The University Of Sheffield.

Electrolyte- Gated Thin Film Transistors for Sensor Applications

By:

Saud Ahmed S. Algarni

A thesis submitted in partial fulfilment of the requirements for the degree of
Doctor of Philosophy in Physics

Faculty of Science
Department of Physics and Astronomy
The University of Sheffield

December, 2016

I dedicate this thesis to my beloved parents,
Ahmed Algarni & Fawzia Algarni

Table of Contents

List of figures

List of Tables

Acknowledgements

First and foremost, I praise and thank Allah the almighty, for the strengths and his blessing in completing my PhD thesis. I would also like to thank my family for their love and support during my postgraduate study.

My sincerest thanks are extended to my supervisor and mentor **Dr. Martin Grell,** for his constant support of my PhD study and related research, for his patience, motivation, and immense knowledge. Without his guidance and persistent help this thesis would not have been possible.

Special appreciation goes to **Dr. Dan Allwood,** my Co-supervisor for his valuable suggestions and encouragement throughout the course of this work.

I thank my group members, for the spectacular discussions, for the continuous work, and for the precious moments that we all have had together in the last years. Dr. Hadi Alqahtani, Dr. Abdullah Alnaim, Dr. Lee Hague, Dr. Antonis Dragoneas, Dr. Adam Hobson, Dr. Alfredo Flores, Dr. Stuart Brittle, Mr. Krisna Adhitya, Mr. Abraham T Kirwa, Mr. Abbad Albaroot.

I thank all my relatives and friends, in and out the university, for their support and kindness. Big thank especially for gorgeous F.Z, who I love so much and my close friend Talal Althagafi for his incredible cooperation and kind contribution to build the Flow cell unit. Also, Many thanks for my best friend Fawaz Alzahrani, my generous roommate Saif Althagafi, and my dearest brother Hasan Albargi.

Additionally, I would like to thank kind people for their collaboration in my PhD thesis: Dr. Antonis Dragoneas from Max Plank institute for his technical support in real time IV converter circuit and programming; Robert Hanson from Chemistry Department, Sheffield university for his advice on the design of their delivery system; Mr. Chris Vickers & Mr. Philip Tylor for their technical support in thermal evaporator problems; Mr. Simon Dixon from mechanical workshop in Physics Department, Sheffield University for making an acrylic box that is used in my delivery system

Last but not least, Special thanks to the University of Taif that granted me full scholarship and as well as the Saudi Cultural Attaché that has supported me.

Abstract

This thesis is concerned with the study and development of water- and other electrolyte- gated thin film transistors (WGTFTs / EGTFTs), including the optimisation of the materials and device architectures, the delivery of aqueous analyte, their electrical characterisation, and use as sensors.

I here report progress in three aspects of WGTFT / EGTFT science:

First, I report ionic liquid (IL) gating of a solution processed semiconducting polymer PBTTT. Due to the high specific capacitance of the IL (estimated as 7 μF/cm^2 in previous research [1] and the high carrier mobility of PBTTT (reported previously up to ~1 cm^2/Vs [2, 3], resulting organic thin film transistors (OTFTs) presented low threshold and delivered high currents (in the order of 1 mA) at low operational voltages, leading to a sheet resistance $R_{\square}$ = 131.6 kΩ/□ at $V_G = V_D$ = -1 V, which is exceptionally low for OTFTs.

Second, I report processing of ZnO thin films by pyrolysis of the precursor Zinc acetate (ZnAc), cast from organic solvents of different quality. We find that a 1:1 mix of Ethanol (EtOH) with Acetone is a significantly better solvent than pure EtOH. ZnO films cast from mixed solvent display a smoother surface while ZnO from EtOH- processed ZnAc shows a grainy surface texture in SEM images. When water- gated transistors were formed from the different ZnO films, transistors from the mixed solvent cast precursor provided more than 4 times larger field effect current than a similar film-cast from the pure EtOH (1100 μA vs 250 μA, all else being equal). The sheet resistance for mixed solvent cast precursor- route ZnO at $V_G = V_D$ = 1 V is 30 kΩ/□, lower than for any organic TFT, and lower than for any electrolyte-gated ZnO TFT reported to date. Hence, I conclude that the performance of precursor- route inorganic semiconductor devices relies upon the selection of the processing solvent, as it is already well documented for organic semiconductors.

Finally, I show that water- gated PBTTT OTFTs are intrinsically sensitive to waterborne amines. For this, I designed and built a bespoke analyte delivery system including a flow cell that delivers a constant stream of electrolyte with variable analyte concentration. PBTTT OTFT currents at $V_G = V_D$ = 1 V were monitored in real time with a TFT characterisation developed by a previous student in our group [4, 5]. Water- gated PBTTT OTFTs react with a decreased drain current when octylamine is added to the water. Normalised current response vs. amine concentration is reproducible between different transistors, and can be approximated by a Langmuir surface adsorption isotherm. This indicates adsorption of water- borne amine

onto PBTTT surface, rather than bulk penetration, as the cause of the observed reduction in saturated drain current. The adsorption constant is found to be $k \approx (150\ \mu M)^{-1}$, corresponding to a Gibbs free enthalpy of adsorption of ΔG^{O} = -31.2 kJ/mol, equivalent to -324 meV/molecule. OTFT response to waterborne amine is reversible and selective at least for amine over alcohol, qualifying such transistors as amine sensors.

Chapter 1
Electronic properties of molecules and crystals used in thin film transistors

1.1 Conductivity of Solid-state Materials

Electrical conductivity is the most widely used property to classify solid-state materials. Conductivity (in units $Scm^{-1)}$, or its inverse resistivity (in Ωcm), is a materials property that spans at last 20 orders of magnitude even when superconductors (with apparently infinite conductivity) are excluded. A pragmatic, engineering- led materials classification introduces demarcations on this sliding scale to categorise materials into 3 families: Insulators, semiconductors, and conductors. Materials with conductivity less than 10^{-8} S/cm are considered to be insulators while materials that have conductivity greater or equal to 10^3 S/cm are taken to be conductors. Materials that fall in between are called semiconductors.

On the microscopic scale, a material's conductivity can be related to the process of charge carrier motion, as explained by quantum mechanics. This is best conceptualised by building up from the quantum description of atoms, which then combine either into molecules, or crystals (or, in the case of organic conductors, sometimes as 'molecular crystals'). Atoms are described with the help of Schrödinger's equation that uses the atomic Hamiltonian operator to find an electron's wave function, and its energy, within an atom. The wave function is a dimensionless complex quantity (i.e. it carries a phase as well as a modulus) that describes the probability of having a particle at a particular time *t* and at location *r* by the square of its modulus.

Schrodinger's equation gives a discrete set of allowed wave functions which define the atomic orbitals. Orbitals are labelled with a set of quantum numbers, namely the principal quantum numbers *n*, the angular momentum quantum number *l*, the magnetic quantum number m_l, and spin quantum number *s*. *l* can take zero or positive integer values where modulus is smaller than *n* based on $(0 \leq l \leq n-1)$, m_l can take positive or negative integers values as $-l \leq m_l \leq l$, and *s* equals +/- ½. The set of quantum numbers defines the orbital's shape, as well as its energy. Pauli's principle demands that no two electrons within the same atom can have the same set of quantum numbers, i.e. each orbital can be occupied only twice (due to the two possibilities for s, +/- ½, which affect orbital energy only very little, hence are taken as belonging to the same orbital). The principle quantum number *n* corresponds to the electron 'shell' stated to be its energy level, albeit in many- electron atoms, the orbital's energy is also

influenced by other quantum numbers (in particular, *l*), so that energies may overlap between different shells. The shell closest to the nucleus is called the *K* shell ($n = 1$), the second is the *L* shell ($n = 2$) (in atomic physics and spectroscopy, letters *K, L, M,…* are used to denote $n = 1, 2, 3…$, while quantum number *l* is specified by lower- case letters *s, p, d, f* for $l = 0, 1, 2, 3$). An atoms' outermost shell is called the 'valence' shell. A valence shell is 'complete' when all orbitals permitted for a given principle quantum number *n* are occupied. The elements that have complete valence shells are chemically unreactive, these are the 'noble gases'. However, if the valence shell of an atom is not completed, it attempts to overlap its partially filled shell with partially filled shells of one or more other atom(s), which may be of the same, or a different, kind, in order to complete their shells. The resulting overlap between atomic orbitals is known as a (covalent) chemical bond, the driving force behind chemical reactions is the desire to reach the lower energy of completed electronic shells.

The compounds resulting from the overlap of atomic shells can roughly be classed into two families: molecules, and crystals. When a small number of atoms combine into a compound, the result is a molecule (e.g. N_2, O_2, NH_3, H_2O, and CH_4). The states of electrons in molecules are characterised by molecular, rather than atomic, orbitals. Often, however, a large (in principle, unlimited) number of one or a few types of atom ('elements') combine into a structure that is periodically repeated in a regular structure in all directions called a 'crystal lattice', or simply 'crystal'. Examples are Cu, Ge, Al_2O_3, ZnO, GaN. The states of electrons in a crystal are characterised by 'bands' which result from the overlap of many atomic orbitals. Note this is a rough classification; there are in fact molecular materials that also repeat the same structure many times, namely 'polymers', also known as 'macromolecules'. However, the structure (called 'repeat unit') typically is repeated in one direction only (the polymer 'backbone'), and polymers do not arrange in periodic 3- dimensional lattices. Instead, they form random coils as the backbone is more or less flexible.

At ambient conditions, many molecules will form gases or liquids, albeit molecules (in particular, relatively large molecules) can also crystallise via weaker intermolecular forces ('dispersion forces') without forming covalent bonds between molecules ('molecular crystals'), or form non- crystalline solids (glasses). Crystals are solids.

Molecules typically have a discrete set of orbitals with clearly separated energy states, all orbitals up to a certain energy level are occupied ('Highest occupied molecular orbital', HOMO), those above that level are empty the lowest of which is the Lowest unoccupied molecular orbital, LUMO. The energy gap between HOMO and LUMO typically is large

(more than 4 eV, i.e. higher than the energy of visible photons). Electrons cannot easily be raised into the LUMO and they are located on one particular molecule. They cannot easily move to another molecule. Molecular materials therefore usually are insulators, albeit there are exceptions, the 'organic semiconductors', see section (1.2).

The electric properties of crystals are controlled by the details of the band structure. In many materials, in particular the 'transition metals' of the periodic table, atomic orbitals are closely spaced energetically and their overlap in the crystal leads to overlapping bands (in the energetic sense). The band overlap leads to a situation where the highest filled energy level in the crystal ('Fermi level') cuts across a band, and leaves it partially filled, with energetically nearby unoccupied states. Electrons in a partly filled band can easily move within the crystals. Metals are therefore electrical conductors. In other solids, bands near the Fermi level do not overlap energetically, resulting in a highest completely filled band ('valence band' VB), and a lowest, completely unoccupied band ('conduction band' CB). When the energetic difference between these bands, the 'band gap' E_{gap}, is large (~ 4 eV or more), then again as in most molecular materials, electrons are not mobile within the crystal, and the material is an insulator. However, when the bandgap is moderate or small, some charge carriers can be raised from VB into CB, e.g. by thermal activation, light ('photoconductors'), or by the deliberate introduction of a small amount of impurity atoms ('doping') that introduce either electrons into the previously empty CB, or vacancies ('holes') into the previously filled VB. Such materials are 'semiconductors'. Note that in their purest form, in dark and cold conditions, the conductivity of a material termed 'semiconductor' (e.g. Si) may be less than the 10^{-8} S/cm used for the pragmatic classification of semiconductors vs. insulators. However, even a small level of doping can hugely increase conductivity, and at high doping levels, a 'semiconductor' may even exceed the nominal borderline between semiconductor and conductor, e.g. for tin-doped indium oxide (ITO).

The gap between HOMO and LUMO in a molecular material is also called a 'band gap', although the molecule strictly speaking accommodates its electrons in molecular orbitals rather than bands. While most molecules are insulators with a large 'band' (HOMO-LUMO) gap, there are exceptions with moderate bandgaps. These are found in organic, i.e. carbon-based, molecules. The unique chemical properties of carbon (C) allow a rich variety of highly complex molecular architectures (including the chemistry of life), but also so- called 'conjugated' chemical bond patterns that lead to rather delocalised molecular orbitals with relatively small HOMO-LUMO gaps. Such materials are called 'organic semiconductors'.

Again, note that very pure ‘organic semiconductors’ will display a conductivity below 10^{-8} S/cm, while some highly doped organic ‘semiconductors’ can be almost as conductive as Platinum (e.g. iodine- or chlorine doped poly(acetylene)).

Many organic semiconductors can be processed from solution, and are responsive to organic analytes. They are therefore particularly interesting in the context of this thesis, and shall be discussed in more detail.

1.2 Organic Semiconductors

While considering the inorganic semiconductors, the covalent model of crystals is effectively used, and conduction of charge is best understood by the band theory, which is based on the movement of electrons in a crystal lattice. For organic semiconductors, which are based on molecular materials, this theory has to be adapted and revised.

First, we have to understand how a relatively small HOMO-LUMO ‘bandgap’ can arise even in a relatively small molecule, rather than an ‘infinitely’ large crystal. This is observed only in a subset of ‘organic’ (carbon- based) molecules, the so- called ‘conjugated’ molecules, a term which therefore often is used as a synonym for ‘organic semiconductors’. This is based on a detailed discussion of the atomic orbitals, and the chemical reactions, of the carbon atom.

Once we understand how a small bandgap can form in a conjugated molecule, we then have to discuss how charge carriers can move between molecules. At first glance, all molecules are characterised by the localization of the charge carriers. It is the same in the case of crystals of organic molecules. Hence the freedom for the movement of carriers appears restricted to a single molecule. We therefore have to introduce the concept of ‘thermally assisted tunnelling’, colloquially called ‘hopping’, of charge carriers between conjugated molecules.

It is primary to understand the formation of bonds in Carbon in order to develop an idea regarding the differences in the organic and the inorganic semiconductors in solid-state materials. The unusual characteristics of carbon can be better defined by the concept of promotion as well as hybridization.

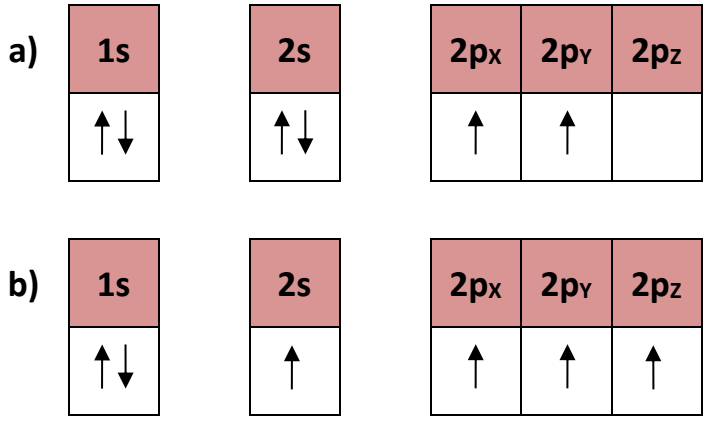

Figure 1-1: The electron configuration and orbital diagram for carbon, a) in ground state and b) excited state after promotion.

As presented in the table, the number of electrons in carbon is 6 and they are schematically arranged into orbitals as in Figure 1-1(a) where as 1and 2 presents the principle quantum numbers *n*, *s* and *p* are the angular momentum quantum number *l* when *l* = 0 and *l* = 1, respectively, X, Y and Z are the magnetic quantum number m_l when m_l = -1, m_l = 0 and m_l = +1 respectively. The arrows mean that electrons exist and up and down directions present spin quantum number *s* for s = + ½ *and* -½.

When a *2s* electron switches its place to an empty orbital called $2p_z$, this is called 'promotion'. Promotion costs a small amount of energy, but this is soon more than recovered.

The remaining *2s* orbitals then can be combined ('hybridised') with one, two, or all three of the *2p* orbitals and hence are referred to as hybrid orbitals. These orbitals can be referred as sp^1, sp^2 and sp^3 respectively. In turn, either no (sp^3), one (sp^2), or two (sp^1) of the original *p* orbitals remain unhybridised. The three- dimensional shape of hybrid orbitals is illustrated in Figure 1-2; note that remaining unhybridised p orbitals are not shown.

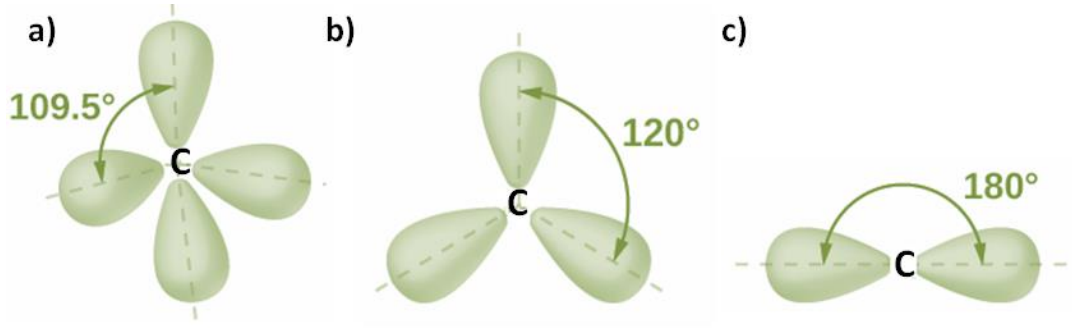

Figure 1-2: Carbon shapes in hybrid orbitals: (a) 4 x sp^3 hybrid orbitals; (b) 3 x sp^2 hybrids, (c) 2 x sp hybrids. Remaining unhybridised p orbitals are not shown in (b) and (c) (there is no remaining p orbital in (a)).

Sp^3 hybrids form equi-spaced orbitals with an angle of 109.5° between the orbitals merge to the centre of tetrahedron, Figure 1-2(a). Note that each sp^3 hybrid orbital is occupied by only one electron, which makes it only half- occupied- it can still accommodate an electron with opposite spin. In this way, the sp^3 hybridised carbon is capable of making 4 bonds by overlapping with half filled orbitals of other, nearby atoms. This may for example be a hydrogen atom, or another hybridised carbon. The overlap between two sp^3 hybrid orbitals of different C atoms forms a strong bond, known as a C- C 'σ' bond. The three sp^2 hybrid orbitals are equi-spaced in a plane, with an angle of 120° between the orbitals whereas remaining *p* orbitals are perpendicular, Figure 1-2(b). When 2 sp^2 hybridised carbon atoms overlap their orbitals, they again form a C-C σ bond. The remaining unhybridised p orbitals of same 2 C atoms will then also overlap, forming a second bond. The second bond is called a π bond, π bonds are somewhat weaker than σ bonds. Note the two bonds in the resulting C=C double bond are not equal, and an example of chemical compounds could be alkenes. The basic reason behind the weakness of the π bond is the larger distance of the *p* orbitals from the parent nuclei. This loose bonding is denoted as delocalization, and serves as the starting point of the electronic delocalisation over an entire molecule, which leads to organic semiconductors. Finally, the *sp* hybrid orbital has two segments at 180° to each other, defining an *x*-axis Figure 1-2(c), and its *p* orbitals become perpendicular on *y*- and *z*- axis. Similarly as explained earlier, the formation of a C-C bond by overlapping two *sp* hybrids now results in one σ- and two π bonds form the overlap of the 2 remaining *p* orbitals. This gives rise to 3 bonds, one is strong while other two weak as they are based on less localised π orbitals. Having three bonds make it a triple bond and is present in compounds, for example alkynes.

When molecules include several carbon atoms, these may form an unbroken sequence of alternating single- and double (or triple) carbon bonds. Such molecules are called 'conjugated'. The π orbitals of subsequent double bonds overlap with each other and lead to delocalisation of their electrons over the entire molecule. Large scale delocalisation can make the energy gap between HOMO and LUMO relatively small, bringing it down to a few eV. Such molecules are organic semiconductors.

While conjugation can occur in extended linear structures (polyacetylene), conjugated molecules often include ring- shaped structures. Note also, while conjugation is based on carbon, conjugated molecules may contain other atoms than carbon and hydrogen, common

'heteroatoms' are oxygen (O), nitrogen (N), and sulfur (S). Two important ring- shaped motifs found in many conjugated molecules are introduced in the next paragraph.

1.2.1 Benzene and Thiophene Ring

A regular hexagon is a planar structure with 6 sides and 6 corners, each with internal angle of 120°. sp^2 hybrid orbitals have an angle of 120° with respect to each other. Hence, by σ-bonding 6 sp^2 carbons we can form a regular hexagon. Each C will form 2 σ bonds, one with each of its neighbours. There remains one sp^2 orbital per C to be 'capped', e.g. by hydrogen (H). The remaining *p* orbitals will again overlap to form π bonds. The resulting structure may look like this:

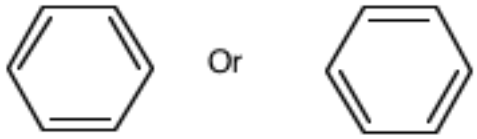

Figure 1-3: Two possible 'borderline' structures of benzene.

It is not quite clear where the π bonds / double bonds should be. In reality, an intermediate state is even more stable, where the π electrons are completely delocalized, so that it is impossible to assign double bonds:

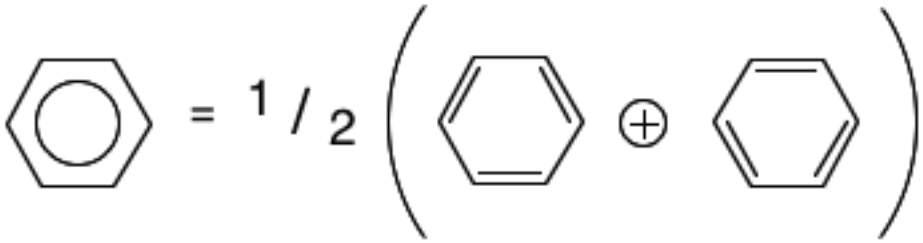

Figure 1-4: The true structure of benzene.

The benzene ring is a key structural motif found in many conjugated molecules. Note, however, that a single benzene ring does not yet provide sufficient delocalisation to bring the bandgap down sufficiently to make a semiconductor. In fact, benzene is colourless, showing that its bandgap is larger than the energy of visible photons. But benzene rings can be part of larger conjugated structures, e.g. they can be 'daisy chained' by linking them together at two of their corners. Linkage can be 'para' (at opposite corners), 'ortho' (at neighbouring corners), or 'meta' (in between). Neighbouring rings linked like that can still rotate around the link. However, rings can also be fused together at two neighbouring corners, forming rigid planar

conjugated systems, called ‘acenes’. The acene made of five benzene rings, pentacene, is an important organic semiconductor.

Other conjugated rings may also contain ‘heteroatoms’, i.e atoms other than carbon, within their structure, and such rings may also contain only five rather than six atoms. Four carbons and one sulfur can form a pentagon like structure, known as thiophene. Again, the sharing of electrons between the atomic orbitals lay the basis of delocalisation due to the π electrons. In a thiophene ring these are induced by electron pairs of a sulphur atom; 4 electrons from carbon together with 2 electrons from sulphur create six π electrons in the ring. Thiophene rings can be linked together at the carbons adjacent to the sulfur, or fused at two corners. Thiophene-based structures have many real life applications as building blocks for organic semiconductors, including semiconducting polymers. The polymers P3HT and PBTTT are just 2 major examples of organic semiconductors that are built on the basis of thiophene rings, Figure 1-5. Note that semiconducting polymers also require the attachment of flexible, non-conjugated sidechains e.g. to the thiophene rings to make them soluble in organic solvents.

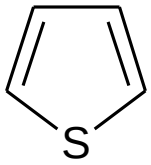

Figure 1-5: Thiophene ring structure

1.2.2 Charge Injection

So far we have only discussed the molecular ground state of conjugated molecules. However, practical applications use excited states: Either, excitons for light emission (not in this work), or charge carriers, either excess electrons in the LUMO, or electron vacancies (holes) in the HOMO. In devices like the thin film transistor, these are generated by charge carrier injection from metal electrodes.

A charge carrier dwelling on a molecular site polarizes its neighbouring region. Consequently it locally distorts the chemical bond patterns and electron clouds to ‘dress’ (screen) the charge. The combination of the charge and the resulting local distortion is called a polaron. In conjugated semiconductors, the fundamental polarization effect is that on the electron clouds and bonds created by the π-electrons [6]. The principle is shown in Figure 1-6, on the example of a charged polythiophene segment. Note how the missing electron (hole) leads to a redistribution of the π-bonds and hence, to different bond lengths and nuclear positions.

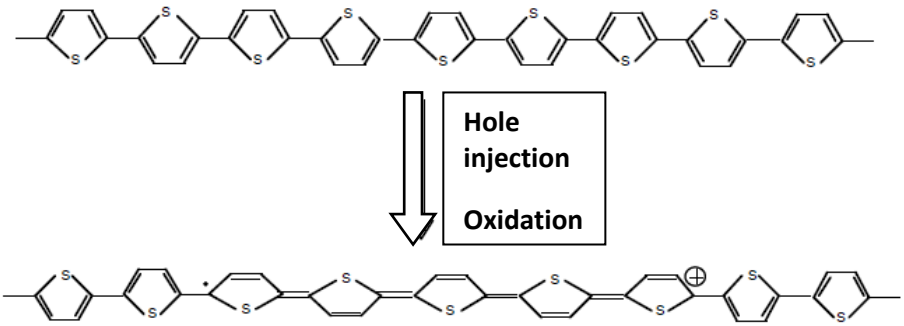

Figure 1-6: polythiophene segment and the derived polaron.

Moving forward, into a deeper level of understanding there are basically two charge injections that can take place at the organic semiconductor. One is the electron polarons and the other is hole polarons. In order to charge inject via the electron polarons an electron is added to the LUMO; on the contrary, to charge inject via hole polarons, an electron is removed from the HOMO – thus, the name hole. The term electron/hole 'polaron' is used to account for the subsequent repositioning of the nuclei in the conjugated molecule together with new orbital levels which together result into the achievement of minimum energy levels. This is typical for organic semiconductors, where charge carriers are localised on a specific molecule rather than delocalised over many unit cells, as in a conventional semiconductor or metal. Electron polarons and hole polarons are also referred to as the radical anions (ones that bear negative charge) and radical cations (ones that bear positive charge); the latter terminology is preferred by chemists.

The energy gained when an electron is added to the LUMO is called electron affinity (E_a), the energy required to remove an electron (inject a hole) from (into the) HOMO is called ionization potential (I_p) respectively. For efficient injection, these have to be compared and matched to the work function of the injecting metal electrodes.

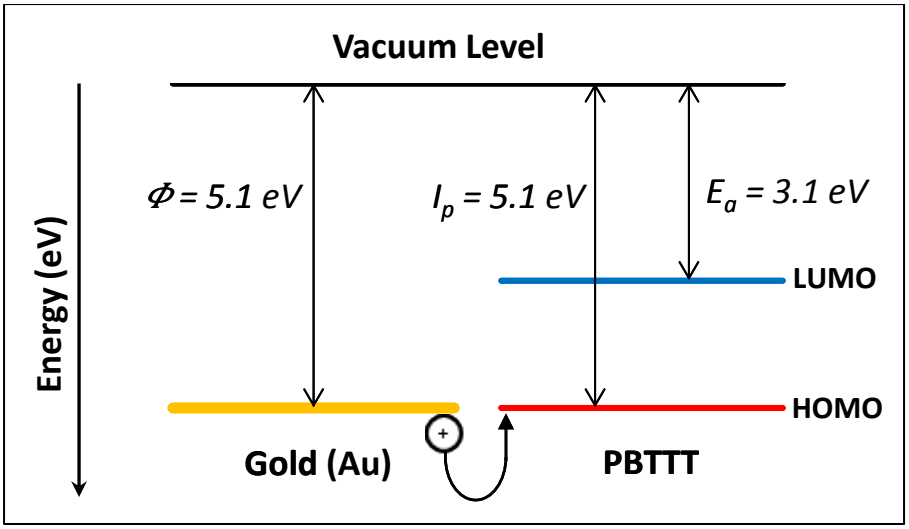

Figure 1-7: A diagram illustrating charge injection into PBTTT, and the energy levels diagram of hole injection barriers from gold electrodes into PBTTT without applying bias. Also this shows how hole injection from Au is better than any lower work function metal for hole injection due to the Au work function is equal to PBTTT ionisation potentials.

According to Marcus Ahles *et al* [7] , there are certain barriers that impede the charge injection into the organic semiconductors; thus these need to be overcome in order to achieve the results of charge injection in an effective and efficient manner. Injection of carriers is controlled by the relative position of the contact metal work function, and the relevant semiconductor transport level. A low work function favours injection of electrons into the LUMO, a high work function favours hole injection into the HOMO, ideally barriers should be avoided altogether by using high work function metals for hole injection / low work function metals for electron injection. For injection, a voltage or potential is applied via a second electrode. Figure 1-7 and Figure 1-8 summarizes the discussion on the charge injection. The applied voltage leads to a field inside the semiconductor that also pulls carriers across the film. Figure 1-8 illustrates this field by showing the HOMO/LUMO levels tilted. However, in the complete absence of doping, the levels remain flat ('flat bands'). In the presence of dopants in the semiconductor, bands will bend near the contacts, forming a Schottky junction. Schottky junctions can assist injection in the presence of barriers, but for organic transistor applications, doping of the semiconductor should be avoided as much as possible.

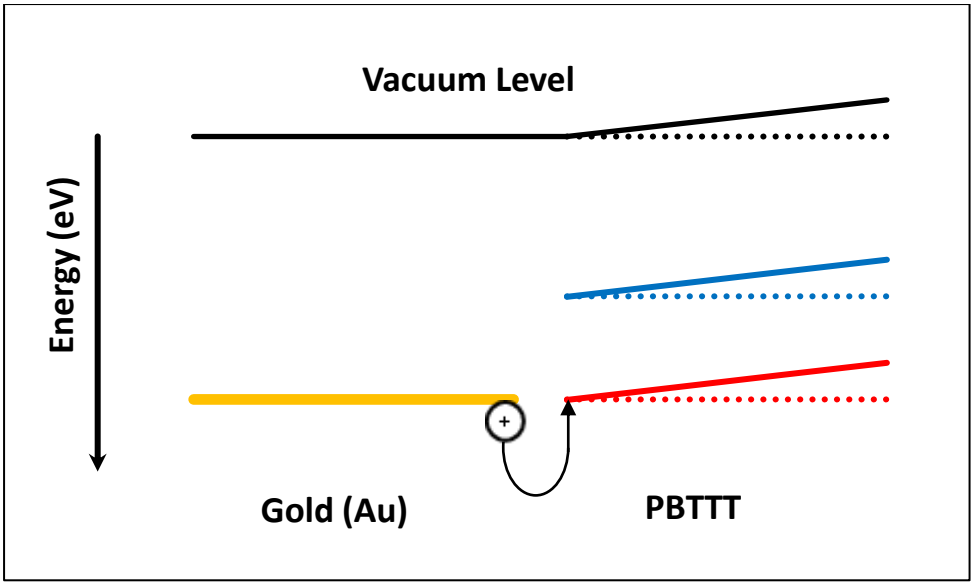

Figure 1-8: A diagram illustrating the energy levels diagram of hole injection barriers from gold electrodes into PBTTT with applying bias.

Moreover, there are two different mechanisms that can help explain the injection of metal into semiconductors as are shown in Figure 1-9. Thermionic emission refers the possibility of the acquiring enough energy to overcome the barrier of injection. On the other hand, Fowler-Nordheim tunnelling helps understand the quantum mechanical tunnelling which helps in by passing the potential barrier of injection. At Fowler-Nordheim conditions the electron tunnels through triangular potential barrier that occurs at the interface between metal and organic semiconductor. An E-field lowers the barrier and makes it appropriately penetrable that is relatively thin and low.

Richardson-Schottky equation (1-1) describes the first mechanism which shows how injection current density (J_{RS}) depends highly on temperature and weakly on E-field [8]:

$$J_{RS} \propto T^2 e^{\left(-\frac{\Phi_B}{kT}\right)} e^{\left(\beta_{RS}\sqrt{E}\right)}, \qquad 1\text{-}1$$

in the above equation Φ_B is denoted as the height of potential barrier and β_{RS} is just a constant ($\beta_{RS} = \frac{e}{kT}\sqrt{\frac{e}{\pi\varepsilon_0 K}}$), whereas ε_0 and $K$are the permittivity of free space and the dielectric constant respectively.

On the other hand, the next equation (1-2) is Fowler-Nordheim equation for the second defined mechanism which is dependent more on E-field compared to temperature; also, this equation

assumes possible changes in the width of the potential barrier rather than the height (as assumed in the first mechanism):

$$J_{FN} \propto \frac{E^2}{\Phi_B} e^{\left(-\frac{\gamma \Phi_B^{\frac{3}{2}}}{E}\right)}, \qquad 1\text{-}2$$

in this equation, γ is constant ($\gamma = -\frac{4}{3}\sqrt{\frac{8\pi^2 m}{h^2 q}}$) whereas h is Plank's constant and m is the electron mass.

However, in the absence of injection barriers, injection will be limited not by barriers, but by the build- up of carriers within the semiconducting film, which via their space charges screen the applied voltage. Such a device will be called 'transport limited' or 'space charge limited'; carrier transport is described in the next paragraph.

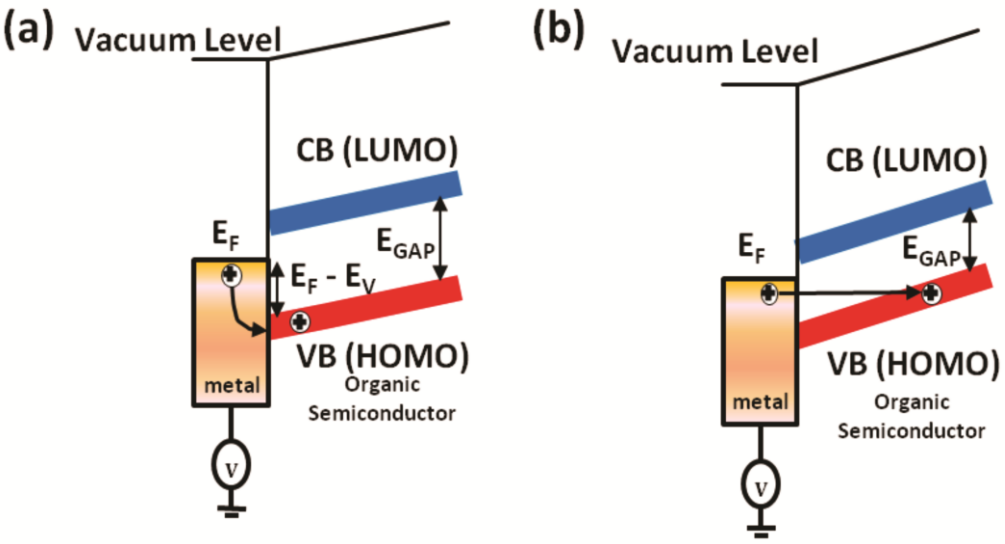

Figure 1-9: charge injection mechanisms from metal into organic semiconductor with applying bias: (a) thermionic emission, (b) Fowler-Nordheim tunnelling.

1.2.3 Transport of Charge Carrier & Mobility

In a working device, after injection from an electrode, carriers then need to move across the semiconductor. The ability of a charge carrier to move under an applied filed is described by

its 'mobility' (μ), typically in units cm^2/Vs, which describes the average velocity of a charge carrier (v) (e.g. in cm/s) when exposed to a unit field E(e.g. 1 V/cm).

$$\langle v \rangle = \mu E. \qquad 1\text{-}3$$

The earlier description of organic charge carriers as 'localised' is at first at odds with the idea of moving carriers.

Therefore, here a comparison of inorganic semiconductors with the, focus of the study, organic semiconductors is initiated; this would be done firstly by understanding and shedding light on what the conceptions of localisation and delocalisation are.

Delocalisation and localisation are opposites of course. The concept of delocalisation revolves around the ability of carriers that are, by default, having the ability to move; also can be referred to as the carriers that already have mobility. Carriers in bands are delocalised, their mobility is high but decreases with increasing temperature. On the contrary to delocalisation is the concept of localisation which revolves around the ability of carriers that are, by default, having no ability to move. However, charge carriers can tunnel from one molecule to a neighbour, this process is helped by vibrations within and between the molecules. This process is called "thermally assisted tunnelling", which is colloquially known as 'hopping'. Hopping mobility is low but increases with increasing temperature.

The value of mobility among organic semiconductors is highly variable; this ranges from10^{-6} – 0.58 x10^2 ($cm^2V^{-1}s^{-1}$) [9]; compare to mobility of charge carriers 10^2–10^3 ($cm^2V^{-1}s^{-1}$) in Silicon [10]. Mobility in organic semiconductors strongly depends on their chemical structure and supramolecular ordering, e.g. molecular crystals have higher mobility than amorphous films [9].

Bässler has carried out extensive computer simulations of hopping type transport to give an equation for field- and temperature dependency of μ [11]. In his model, he assumes that HOMO levels are not all equal in energy, but display a Gaussian distribution around the average HOMO. This energetic distribution is termed diagonal disorder and is characterized by variance σ^2, or the dimensionless $\hat{\sigma} = \sigma/kT$. Hopping rate is also affected by positional or off- diagonal disorder that is quantified by another variance, Σ^2. Bässler arrives at the following equation [11]:

$$\mu(E,T) = \mu_0 exp\left[\left(-\frac{2}{3}\hat{\sigma}\right)\right]^2 \begin{cases} exp\left[C(\hat{\sigma}^2 - \Sigma^2)E^{\frac{1}{2}}\right]; & \Sigma \geq 1.5 \\ exp\left[C(\hat{\sigma}^2 - 2.25)E^{\frac{1}{2}}\right]; & \Sigma < 1.5 \end{cases}, \quad 1\text{-}4$$

wherein C is empirical constant and μ_0 is a fit parameter which accounts for the specific molecule, and cannot be predicted within the theory. More recently, Pasveer *et al*. have updated Bässler's transport model to also account for the observed dependency of mobility on charge carrier density [12]. Pasveer's results cannot be cast into an analytical equation, but that for high carrier concentration, as in organic transistors, mobility can increase by several orders- of- magnitude, in line with experimental results [13]. This is rather fortunate, but still, hopping mobility is always lower than for band- like transport of delocalised carriers. Also, even Pasveer's theory does not allow mobility to be determined simply from a given chemical structure of a molecule. Like Bässler's μ_0 , Pasveer's theory contains parameters that have to be fitted to measured data, and resulting mobilities in films made of the same molecule may still strongly depend on film preparation conditions.

Finally, to discuss transport in a device, we also have to account for so- called 'space charges', which arise from carriers within the device. Space charges partially screen the externally applied voltage / field within the device. Let's first look at the Ohm's law model and equation to create basis for discussion.

$$J_{drift} = \frac{I_{drift}}{A} = \sigma E, \quad 1\text{-}5$$

where J_{drift} is drift current density and σ is semiconductor conductivity. In addition, I_{drift} is the drift current per unit area going through of a cross-sectional area of the semiconductor A when the field E is applied.

Ohm's Law accurately describes current in a metal, where space charges are absent. However, in a semiconductor (both organic and inorganic) due to screening by space charges, the electric field is variable and different in different parts of the film which is situated in the semiconductor device. Charge carriers therefore experience less field than is applied externally, and overall current is reduced. This kind of current is known as the space-charge limited current (SCLC). Following is the equation for this kind of current, known as Child's law:

$$j_{SCLC} = \frac{9}{8}\epsilon_r\epsilon_0\mu\frac{V^2}{L^3}, \quad 1\text{-}6$$

where ϵ_r is the static permittivity of the semiconductor, ϵ_0 is the vacuum permittivity (~8.854 x 10^{-12} F/m), μ is the mobility of charge carriers, V is the externally applied voltage and L is the length of the conduction path.

1.2.4 Traps

Defects are a fact of life in all semiconductors. In crystalline semiconductors, these may be impurities or dislocations, in organic semiconductors e.g. a degraded (e.g. oxidised) molecule. However, since such defects are themselves localised at a specific point, the effect of defects on localised carriers is far stronger than on delocalised carriers. Localised carriers may be immobilised completely when they are captured by a defect. In localized states when the charge carriers are immobilised they are known as trapped carriers, which still contribute to space charge, but no longer to mobility or transport (i.e., current). There are *hole traps* and *electron traps*: The category of *electron traps* refers to the properties of a trap charge carrier which has its electron affinity lower than the LUMO, whereas *hole traps* refers to a trap site which has ionisation potential above the HOMO. 'Trapping' may not be terminal but carriers can be released again after a while which depends on the depth of the trap, which are roughly classed as 'shallow' or 'deep'. Shallow traps are those where carriers can be thermally released, deep traps cannot be thermally released.

Trapping and delayed release effectively reduces carrier mobility. This can be accounted for by introducing an effective mobility,

$$\mu_{eff} = \Theta\mu_0\,, \quad 1\text{-}7$$

therein, Θ is the fraction of mobile (i.e., not trapped) carriers. Equation (1-8) quantifies Θ by the activation energy required to release a carrier from a trap,

$$\mu_{eff} = \mu_0\alpha e^{-\frac{(E_C - E_t)}{kT}}, \quad 1\text{-}8$$

wherein in E_C is the respective transport band edge (HOMO or LUMO, respectively), E_t the trap level, and α is The ratio of trap density of states to the effective density of states at the transport band edge [6].

According to Nicolai *et al* [14] , the cause of electron trap can be oxidization of the atoms and molecules. Since it was already noted that *electron traps* refers to the properties of a trap charge carrier which has its electron affinity lower than the LUMO, hence when this electron affinity overlaps the traps it gets the oxidation process started as also explained by Quantum chemical calculation.

Trapping of localised carriers explains why organic semiconductors often transport only one type of charge carriers (holes, or electrons). A material with many electron traps will effectively have no or very low hole mobility, and vice versa. Thus organic semiconductors can be categorized as hole-transporters or electron-transporters; hole transporters are more common. There is a rare third type of semiconductors which are known as ambipolar; ambipolar materials possess the property of transporting both types of charge carriers [15].

1.3 Thin film transistors (TFTs)

1.3.1 Transistor History

Looking at the history of transistors, the first patents on field effect transistor (FET) was recorded to Lilienfeld in the year 1925; in order to process the signals a tube was used which was not just bulky but also consumed a lot of electricity. John Bardeen, William Shockley and Walter Brattain were rewarded with the Noble Prize in 1956; their contribution was the creation of a bipolar transistor in the year 1947. Kilby and Noyce in 1958-59 built an integrated circuit (IC) which was another step in the transistors improvement; followed by Atalla and Kahng in 1959 [16] who were inventors of the MOSFET. In 1962, Weimer was the first person to introduce thin-film transistors as a form of inorganic thin-film devices [17]. This was a very important development which has shaped different devices and brought a lot of ease through the formation of different electronic applications which were created through the basis of this concept. Talk about active matrix or the famous TFT liquid-crystal displays (LCDs) devices that enable display of individual pixels on the screen; all are products on the basis of the concept by Weimer [17]. In a nutshell, transistors have gone through a lot of improvements for many decades and the versions of transistors that we see today, ones that are used more or less in every electronic device, are the most improved and sound kinds of transistors to date. Computers, laptops and mobile phones, electronics that we use every day have transistors in their list of components. The transistors we use today are not just flexible but also very low cost together with the ability of ease of fabrication.

1.3.2 Thin Film Semiconductor Devices

Organic Photovoltaic Cells (OPVs), Organic Light-Emitting Diodes (OLEDs), Organic Field-Effect Transistors (OFETs) as well as the Organic Chemi-Resistors, all are innovated and versions of thin-film devices; these were however created through the success of utilizing the architecture of thin-films to develop organic semiconductor devices. This concept was amazing due to the fact that the range and application of electronic devices increased to as far as fabricating them on plastics which are not just transparent but also flexible. Within this thesis, the emphasis is on thin film transistors including organic, and solution- processed inorganic devices.

For the practical application in the organic semiconductors, when transistors are configured usefully, the transistors used, mostly, are the thin-film transistors (TFT). Weimer, in the year 1960, proposed this concept and developed it in the polycrystalline inorganic transistors [17]. However, later in the year 1980, the development of first ever organic TFT was reported [18, 19].

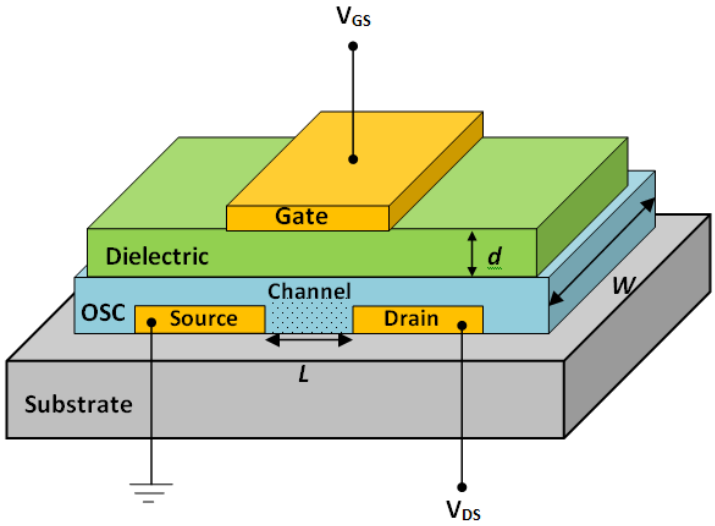

Figure 1-10: The structure of a thin film transistor and illustrating channel dimensions (width (*W)* & channel length (*L)).* The TFT is a three terminal device, terminals are called source (S), drain (D), and gate (G).

Figure 1-10 shows the principle design of an organic thin film transistor *(OTFT)* with electrical connections suitable for basic measurements. The OTFT is similar in principle to the inorganic MOSFET (but unlike the JUGFET). Two contacts known as source (S) and drain (D), separated by a channel, are prepared on a semiconductor film. The semiconductor in an OFET has to be as pure as possible (intrinsic semiconductor). Doping is highly undesirable. That is quite different for other transistor types, but suits the use of organic semiconductors which are

difficult to dope in a controlled way. S and D usually are identical; which one is which is defined by the electrical wiring: the contact connected to ground is called S. At D a voltage can be applied. This voltage is called the drain or drain- source voltage V_{DS}. V_{DS} attempts to drive a current through the semiconducting transistor channel. However, a drain current I_D will only flow if there are mobile charge carriers in the channel. Since the semiconductor is not doped, by itself there will be very few charge carriers in the channel, and I_D will be very low – the OFET is 'off'.

However, carriers can be introduced into the channel by a voltage applied to a third terminal, known as the gate. A gate (or gate- source) voltage V_{GS} of appropriate polarity will pull carriers out of the source into the semiconducting channel. However, gate contact and channel semiconductor are separated by a gate medium, usually a dielectric insulator, but in some cases, a ferroelectric insulator, or an electrolyte. The carriers therefore cannot reach the gate metal. Instead, they will accumulate in the semiconductor near the channel/insulator interface, forming an accumulation layer. The channel semiconductor therefore gets 'doped' with charge carriers by applying V_{GS}, and a substantial I_D can flow: The OFET is 'on'. Practically, the applied gate voltage needs to exceed a certain threshold voltage V_T to switch the OFET on. Other than chemical doping, gate voltage doping is quickly reversible by switching V_{GS} off.

Simplistically, the OFET is an electronic on/off switch. The switch is not operated mechanically though, but by the gate voltage. In contrast, bipolar transistors are actuated by a small current, rather than a voltage.

As organic materials are characterised as either electron- or hole transporters, the gate voltage to attract carriers into the channel has to be chosen appropriately: negative gate voltage (with respect to source) attracts holes into the channel, positive gate voltage attracts electrons.

Threshold voltage (V_T) and charge carrier mobility (μ) are important parameters of an OFET which together with gate and drain voltages, and the geometry factor W/L, control the magnitude of the resulting I_D. A quantitative discussion is to follow.

1.3.3 Field Effect Transistor (FET) Structures

For FET, there are four different device architectures that can be employed; each of these architectures is unique, in terms of nature and performance, and results from a different sequence of depositing the TFT's parts.

For any design to effectively build an accumulation layer it is imperative that above the semiconductor's channel, a gate contact is placed. It is also necessary to have the semiconductor's channel to be segregated from the gate contact by a gate medium. Moreover, in order to allow the charge carriers to move freely from the source contact into the channel, it is necessary to have small energy barriers in place between the semiconductor material and contacts' interfaces as be explained in section (1.2.2).

Still, a number of different architectures are conceivable, see Figure 1-11.

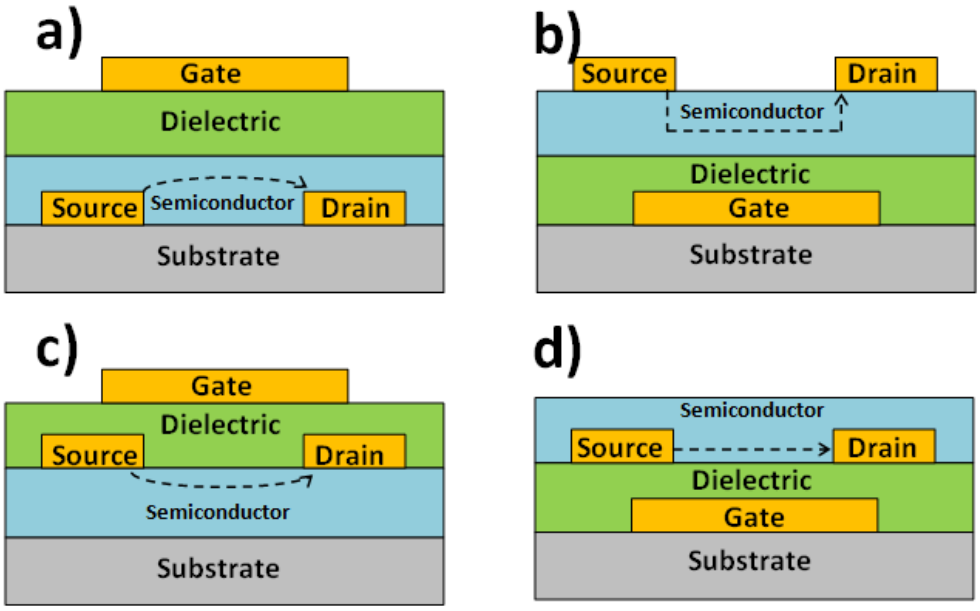

Figure 1-11: Different thin film transistor constructions: a) top gate & bottom contact, b) bottom gate & top contact, c) top gate & top contact and d) bottom gate & bottom contact configurations. Dashed lines shows the charge carriers through the channel.

Note that in structures a and b, the gate voltage / gate field can assist the injection of carriers from the source into the channel, but not in c or d. Architectures a and b therefore will more closely approximate 'ideal' contacts that allow carriers to cross into the semiconductor without any hindrance. Otherwise, modification through proper treatment on the surface of the contacts can help to decrease energy barriers and lead to lower resistance of contacts [20].

In a thin-film transistor, charge carriers are transported at the gate-insulator interface of the semiconductor. A gate insulator thus is a significant and potential determinant of the resulting properties of the transistor [21]. The transistor's performance for example can be jeopardized and reduced largely if the gate-insulator has low levels of permittivity; this would result in the low capacitance (per unit area). On the other hand, high levels of permittivity would result in

impeding the transport of charge carriers due to the fact that they trigger more energetic disorder inside the channel. SiO_2 is a typical gate insulator and it is known to trap electrons. Different studies have suggested different mechanisms and acts to reduce the trapping of electrons by a SiO_2 insulator. According to Chua *et al* for example [15], the trapping can be reduced by applying polyethylene to the surface of the SiO_2 which would result in shielding superficial hydroxyl (-OH) groups hydroxyls are known electron trap sites. However, SiO_2 cannot be processed from solution, and has low dielectric constant. Many other dielectrics have been explored, polymer insulators such as poly(vinyl alcohol) or poly (vinyl phenol) that can be chemically crosslinked after processing have proved particularly useful, as the can be processed from solution, and form very thin insulating layers with consequentially high capacitance [22, 23].

The gate metal is not directly in contact with charge carriers, but via its work function, it does influence the value of threshold voltage. The equation (1-9) shows there are two contributions to V_{th} ,

$$V_{th} = V_{FB} + \frac{qp_0 d_s - Q_i}{C_i}, \qquad 1\text{-}9$$

where V_{FB} is the flat-band voltage, q is the charge on each carrier, p_0 is the trap density in semiconductor bulk and the interface of semiconductor/dielectric), d_s is the thickness of the semiconductor film and C_i is the capacitance per unit area of the gate insulator.

The first contribution to V_{th} in equation (1-9) is the flat band voltage V_{FB} That is given by the properties of the materials used- work functions of gate metal $\emptyset_m$, and either the ionisation potential I_p of p-type of organic semiconductor or the electron affinity E_a of n-type organic semiconductor ,

$$V_{FB} = \emptyset_m - I_p \, . \qquad 1\text{-}10$$

With reasonable choices of materials, V_{FB} is typically less than 1 V. In fact, transistors may even be 'normally on', i.e. on at zero gate, meaning threshold voltage is slightly positive (negative) for hole (electron) transporting semiconductors (practically more often observed for electron transporters). The second contribution to V_{th} is from carrier traps in the semiconducting channel. This contribution is moderated by the gate medium's specific capacitance, C_i. For low capacitance, the second contribution dominates V_{th} and can lead to large (negative/positive) threshold voltages for (hole/electron) transporting TFTs, never to 'normally on' behaviour. But for high C_i, like in 'electric double layer' (EDL) gated devices

that will be discussed later in section (1.3.5), the trap contribution is strongly moderated, and $V_{th} \approx V_{FB} < 1$ V is usually achieved that leads to become significant for low threshold transistors.

1.3.4 Quantitative description of FET Operation

A gate medium is characterised by a specific capacitance C_i (capacitance per unit area) which for a dielectric can be calculated with the following equation or formula:

$$C_i = \frac{\varepsilon_0 k}{d}, \qquad 1\text{-}11$$

where, k is relative permittivity of gate insulator ε_0 is the vacuum permittivity and finally, d is the gate insulator thickness.

The transistors face the build-up of an accumulation layer when a voltage with high level is applied to the gate. Negative charge carriers are introduced into the channel through the gate contact which is positive. Similarly, positive charge carriers are in introduced into the channel through the gate contact which is negative. However, usually, the gate voltage has to exceed a value known as 'threshold voltage' (V_T or V_{th}) before the transistor builds up an accumulation layer. The magnitude of V_{th} depends on a number of factors, including the work functions of source- and gate metals, and the magnitude of C_i, tending to lower threshold for higher C_i.

Consequently, TFT operation is divided into certain regions according to the magnitude of V_{GS} with respect to V_{th}, and V_{DS}. These are namely Subthreshold regime, Linear regime and Saturation regime. Linear and saturation regimes are operationalized when the gate voltage exceeds the threshold voltage.

Drain current I_D, as was explained earlier, can be controlled by two voltages namely: gate voltage and drain voltage, V_{GS} and V_{DS} respectively. So the three scenarios of transistor operations that activate either of the regions, under consideration, are as follows:

Scenario 1: When the applied gate voltage is smaller in magnitude than the threshold voltage, no accumulation layer forms and the drain current is very small. However, drain current is measurable and rises exponentially with increasing gate voltage until threshold is reached. I_D is given by the following equation as the transistor operates in the sub-threshold region [6]:

$$I_D = K\mu C_i \frac{W}{L}\left(1 - e^{\frac{-qV_{DS}}{kT}}\right) e^{\frac{qV_{GS}}{nkT}}, \quad 1\text{-}12$$

where K is a constant for a particular device structure and employed materials, the elementary charge is presented by q, the Boltzmann constant (~1.3806 × 10^{-23} m^2 kg s^{-2} K^{-1}) and the temperature are denoted by k and T respectively. Also, n is the ideality factor ($n = 1$) as a result of $C_s = 0$ on ($n = 1 + \frac{C_s}{C_i}$) where C_s and C_i are the capacitance per unit area of the traps at the semiconductor-insulator interface and the capacitance per unit area of the gate insulator respectively.

Subthreshold characteristics are best analysed on a logarithmic scale, log (I_D) versus V_{GS}. A useful quantity is the inverse sub-threshold slope, also known as sub-threshold swing S [6]:

$$S = \frac{\partial log_{10}(I_D)}{\partial V_{GS}}, \quad 1\text{-}13$$

the sub-threshold swing is proportional to the ideality factor based on:

$$S^{-1} = ln(10)\frac{nkT}{q}, \quad 1\text{-}14$$

the gate voltage change required for an order-of-magnitude change in drain current is described by the quantity of S^{-1} in units of mV/decade.

Moreover, the variants of the above equation would result in the capacitance of the trap density as well as the gate dielectric.

For example, at a temperature of 293K the value from the equation (1-14) would be:

$$S^{-1} = 57n\ {}^{mV}/_{decade} \quad 1\text{-}15$$

For organic transistors, the ideality factor n is given by the ratio of the specific capacitance C_i of the gate insulator to the specific capacitance of carrier traps in the semiconductor, and at the insulator/semiconductor interface, C_t, as $n = 1 + C_t/C_i$ (conceptually, this describes the competition of traps with mobile charge carriers in the accumulation layer). Small subthreshold swing, hence small n, are desirable as they lead to a steeper off → on transition ('switching') and lower threshold. Thus, $n = 1 + C_t/C_i$ explains why large C_i lowers threshold.

Even though, the range of the swing values for OTFTs typically are between 0.5 and 5 V/decade [6], but lower swings have been reported for high capacitance dielectric gate media [24], and for electrolyte- gated transistors.

Scenario 2: It can be defined when the drain voltage is less than the difference of gate voltage and threshold voltage; this scenario would activate the transistor to work and operate in the linear region as be seen in Figure 1-12(a), I_D is described by the following equation:

$$I_D = \mu C_i \frac{W}{L}\left((V_{GS} - V_{th})V_{DS} - \frac{V_{DS}^2}{2}\right), \quad 1\text{-}16$$

where mobility of the charge carrier is denoted by μ, the length and width of the channel are presented by L and W respectively. The capacitance per unit area of the gate insulator is denoted by C_i.

For $V_{DS} << V_{GS}$-V_{th}, the term quadratic in V_{DS} can be neglected, hence this is called the 'linear' regime. In the linear regime, $I_D \sim V_{DS}$, as in an ohmic resistor.

Scenario 3: It can be defined when the drain voltage is more than the difference of gate voltage and threshold voltage; this scenario would activate the transistor to work and operate in the saturation region as be shown in Figure 1-12(c), I_D is described by the following equation:

$$I_D = \mu C_i \frac{W}{2L}(V_{GS} - V_{th})^2. \quad 1\text{-}17$$

This region is actually activated when the carriers are least effective at the drain end of the channel due to the minimized impact of gate voltage at the electrodes of drain; this phenomenon is also referred to as the pinch-off. This regime is known as saturation because the drain current is 'saturated', meaning it no longer increases with increasing V_{DS}. I_D can only be further increased by increasing the gate voltage.

Measurements of TFT electrical properties can be differentiated into two forms of electrical characteristics, namely: transfer or output. Transfer refers to the condition where drain current is measured versus the gate voltage while keeping the drain voltage constant. When these characteristics are measured at a low/high drain voltage, this is known as the linear/saturated transfer characteristic. On the other hand, the characteristics termed as output refer to the condition where drain current is measured versus the drain voltage while keeping the gate voltage constant. More details on the characterisation methodology are given in section (3.2.1).

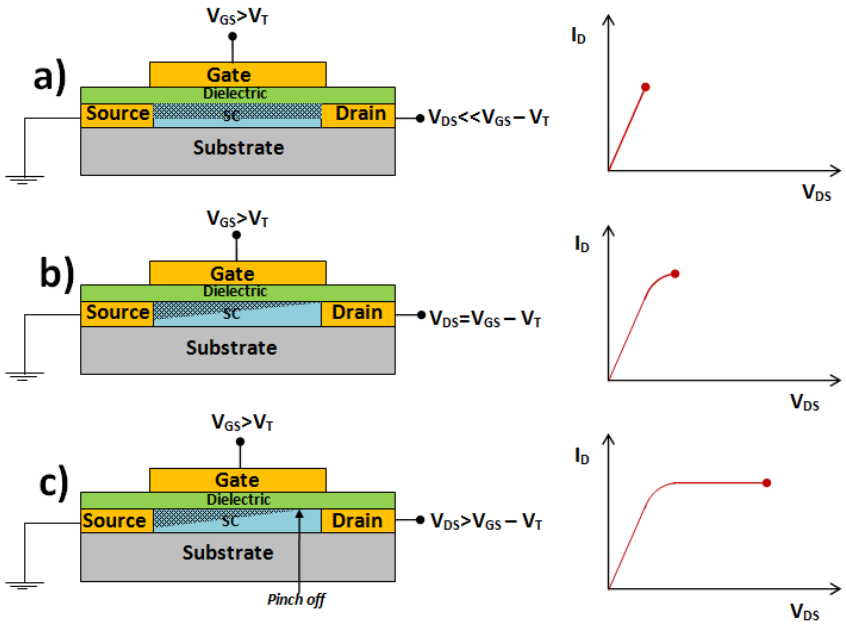

Figure 1-12: Field effect transistor operating regions is shown by an ouput characteristics: (a) linear regime, (b) saturation start at pinch-off and c) saturation regime.

1.3.5 Electrolytes as Gate Media

An electrolyte is a liquid, or a solid, that contains at least one species of mobile ions. A simple example is a solution of a salt in water. Thanks to its high polarity, water can release ions from the crystal lattice of many solid salt and 'hydrates' them within liquid water. However, many other electrolytes are known.

Here follows first, an introduction to the electric properties of electrolytes, which will conclude that they can serve as an alternative to dielectric insulators as gate medium for TFTs. Then, a few examples of electrolytes are discussed that have been used as gate media for TFTs, and are relevant to the work reported later in this thesis. Then, a brief overview over electrolyte- gated TFTs will be presented.

1.3.5.1 Electric Double Layers (EDLs)

When a pair of electrodes is inserted into an electrolyte, a capacitor is formed. When a voltage is applied between the electrodes, mobile ions will migrate towards the respective oppositely biased electrode and build up an 'electric double layer' (EDL) at the interface (somewhat similar to a Schottky contact). An EDL consists of the biased surface of the metal contact, and the layer of opposing ions (of opposite charge) that builds up within the electrolyte at the interface. The EDL shields the bulk of the electrolyte from the applied field, an electrolyte is conductive only as long as the EDL takes to build up. Hence electrolytes are DC insulators,

but AC conductors. The EDL is extremely thin and therefore represents a high specific capacitance, typical values range from 1 μFcm^{-2} to 10 μFcm^{-2}. This high capacitance destines electrolytes as TFT gate media for low threshold.

As the positively charged electrode is called as anode and one that is negatively charged, cathode, the layers have also been coined different names as opposite ions from electrolyte form layers. One is called anionic as it forms at anode while the other is termed as cationic from the word cathode. Anions are *negatively* charged, cations positively. For an in-detail research, more sophisticated and advanced EDL models were devised to understand ion distribution, the field and electrode potential, which have to be discussed briefly. These models show different outcomes but the properties suggested coincide qualitatively, at least on the high capacitance.

Following are some properties of electrolytes and EDLs:

1. The double layer is thinner than 1 nm; whereas the density of the carrier is high, within the layer [25]. This explains the high capacitance.

2. As a capacitor requires two plates, EDLs always come in pairs (one anionic, one cationic). The total EDL capacitance is the result of the serial combination of the two EDL capacitances, following the rule of adding serial capacitances.

3. The field is only strong near the contact with metal; the bulk of the electrolyte remains field- and net charge- free. Similarly if the potential is considered, it remains constant within the bulk of the electrolyte, away from the contact but it changes almost step like near the contact position.

4. The build- up of an EDL can be slow, albeit it strongly depends on the electrolyte. In 'deionised' water, EDL build up can take ~1 second [26]. Water is therefore slightly conductive for AC frequencies down to ~1 Hz. Water carrying some dissolved salts is rather conductive at 50 Hz (the notorious 'hairdryer in the bathtub').

5. Every electrolyte can endure only a limited voltage, this material's property is called the electrolytes' 'electrochemical window'. When a voltage larger than the electrochemical window is applied, the electrolyte decomposes electrochemically ('electrolysis'). By comparison, dielectrics may also suffer destructive breakdown, but this is caused by an excessive electric field (voltage/thickness) rather than an excessive voltage.

For understanding the mechanics and the quantitative models designed over the double layering, we briefly discuss a few theoretical EDL models. Note, these are devised with salt solutions in water in mind, and may not fully translate to other electrolytes.

As the first historical to devise a model, Helmholtz's name and contribution cannot be forgotten. According to his model the layer is built around the contact area of the electrode, counter ions layer, and is over a small distance and is uniform till the distance when the charge over the area is fully balanced [27]. This potential of the electric contact is considered as a decreasing phenomenon as it moves down to the excessive quantity of electrolyte, and decreases linearly. The distance becomes limited to just the water molecules, between the electrode and the ions. This boundary formed is called the outer plane. This model has some deficiencies, as it is unable to comprehend the capacitance and its relation to the lower concentration, where actually the layers are not rigid. Similarly another model such as Gouy-Chapman model, while defining the effect of the thermal motion over the ions attracted, relates the concept by stating that the potential weakens as we go away from the electrode and hence form two layers which can be Helmholtz layer and the other one diffusing, consisting of positivity and negativity of charges [28]. But the model lacks in making a relation with the suggested to the actual experimental results as the capacitance gained from the experiment is quite less than what was to be depending on the capacitance as well as concentration. Here another model can be brought in, which is termed as Stern model [29]. It actually brings the two models together. Stern has assumed that only the ions that are attracted could not balance the layer called as Helmholtz hence a diffusion layer fills the deficiency. The dropping of potential is similarly defined as linearly and an exponential fall in the diffuse layer. It can be stated through equation: electrode capacitance being supported by two layers as it has been stated previously in the Gouy-Chapman model [30].

$$\frac{1}{C_S} = \frac{1}{C_S^{Hz}} + \frac{1}{C_S^{D}}, \qquad 1\text{-}18$$

C_S^{Hz} is the capacitance of the Helmholtz layer has been taken from equation (1-11) as the distance of double layer has been denoted by *d* showing the distance of double layer between the contact of the electrode and the centre of accumulation charged ions. The capacitance C_S^D is of the diffused layer [30] that is Calculated by an intricate equation as be following:

$$C_S^D = \frac{4zeN_A C_\infty \lambda_D}{\Psi_D} \sinh\left(\frac{ze\Psi_D}{2k_B T}\right), \qquad 1\text{-}19$$

where the electrical potential is denoted by Ψ_D. λ_D and z are Debye length and the valency of electrolyte respectively, e is the elemental charge molar concentration of the electrolyte in the bulk C_∞ , Avagadro's number N_A and Boltzmann constant k_B are constants.

Despite the numerous models, not one model looks into the practicality of Double layer dynamics and its important follow up by the ions attraction except for the only one that is Gouy-Chapman model. Here it can be referred that Wang *et al*. did a fabulous job to explain the effect of the concentration of the electrolyte which in turn strengthen the capacitance of the EDL, and he does that by simulations numerically [30]. An example could be finding out the increase in ion concentration from .001 mol/l to .01 mol/l can increase the capacitance C_S^D from 12.7 μFcm^{-2} to somehow 40.3 μFcm^{-2}. It also saves us from misinterpretation after the last fact is considered.

We now look at a few electrolytes that have been used as TFT gate media, and are relevant to this thesis.

DI Water

Even deionised water acts as an electrolyte through 'autoprotolysis'

$$2H_2O \rightleftharpoons H_3O^+ + OH^-$$

i.e. the spontaneous separation of water molecules into hydroxide ions (OH^-) and hydronium ions (H_3O^+) shown in Figure 1-13; the latter are sometimes 'abbreviated' as H^+ (protons). The chemical equilibrium for an autoprotolysis is strongly on the non- dissociated side, at T = 25 ^oC the concentration of H_3O^+ is only 10^{-7} mole/L (hence, pH = 7 for pure water at 25 ^oC). For comparison, the concentration of non- dissociated H_2O is 55.6 mole/L. Consequently, DI water displays a low conductivity.

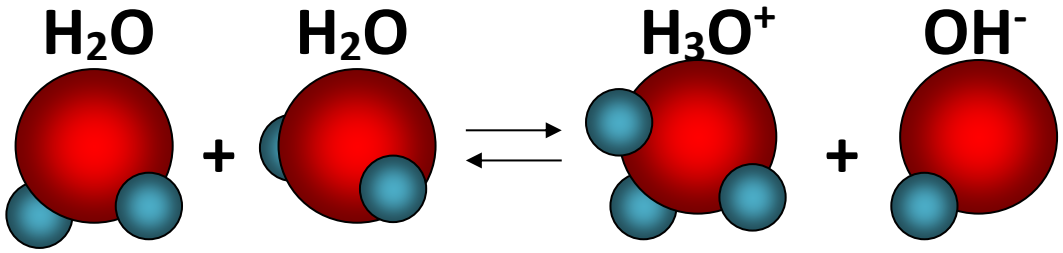

Figure 1-13: Spontaneous separation of water molecules into hydroxide ions (OH^-) and hydronium ions (H_3O^+).

Furthermore, the conductance of DI water increases by its exposure to air because then CO_2 or carbon dioxide dissolves in it resulting in the formation of carbonic acid; the conductance, after this exposure, inclines to about 1 (S cm^{-1}) [31], and the pH drops to about 5.5.

Nevertheless, even DI water can build up an EDL at the interface with electric contacts, and has been used as gate medium for an organic TFT [26]. The capacitance was quoted as 3 μFcm^{-2} and the electrochemical window of water amounts to 1.23 V [32], but the high capacitance brings the threshold voltage down sufficiently so that OTFTs can comfortably operate within this window.

Buffer Solution

An aqueous solution, which resists changes in pH after adding small quantity of acid or base and consists of a weak acid (HA) and its conjugate base (A^-), is called a buffer solution. To avoid pH changes, it is possible to use buffer solution e.g. Phosphate buffered saline (PBS) for biosensor applications due to, it is a biologically realistic aqueous electrolyte as a simulated fluids of organism[33-35].

After using buffer solution (PBS) as gate medium, a high drain current is observed that means, charge carriers amount is larger and forms stronger accumulation layer in the semiconductor–electrolyte interface due to PBS is higher ionic strength than DI water.

Ionic Liquids (IL)

These electrolytes are the composition of positive as well as negative mobile ions which are made of organic salts that have a melting point below room temperature. Ionic liquid has a lot of upsides, some of which are its zero volatility together with robust stability in terms of chemically, thermally and also electrochemically. 0.1 (S cm^{-1}) is the approximate value of conductivity of ionic liquids at room temperature and ambient condition [36]; this is due to the higher values and amounts of concentration that when compared to DI water are very high; for water the concentration is low mainly because of the dissociation that is associated with the water molecules.

Figure 1-14 shows an example IL that has been used to gate transistors [1], *EMI-TFSI* which is an ionic liquid and has the following composition:

1-ethyl-3-methylimidazolium-bis (tri fluoro methyl-sulfonyl) imide

For this composition the electrochemical window is also very high, compared to water for example; 1.23 V of water versus 4.3 V of this composition. Furthermore, it enhances the capacitance by providing it with about ~6.5 μFcm^{-2} at 1 Hz and ~5.17 μFcm^{-2} at 10 Hz [37]. In fact, EDL capacitance remains significantly higher than for aqueous electrolytes up to kHz frequencies. When we combine these two properties, we realize that, in comparison to pure water, the maximum possible gate electric displacement $C_i V_{GS,max}$ is now 10 times bigger. These are applicable and used to achieve relatively low levels of voltage together with fast-switching FET while making sure that the mobility of the organic semiconductor is not compromised.

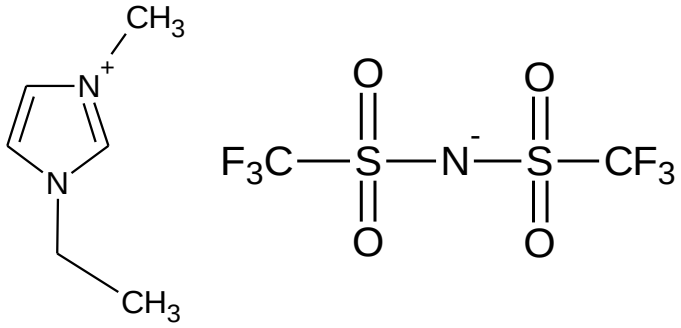

Figure 1-14: The chemical structure of 1-ethyl-3-methylimidazolium-bis(trifluoromethyl-sulfonyl)imide ('EMITSFI').

However, ILs often are good solvents for organic materials, including semiconducting polymers, which compromises their use with most solution- processed organic semiconductors.

Polar Solvents

Al Naim *et al* [38] have shown that some organic solvents can also act as electrolytic gate media. In particular, polar solvents (more precisely, solvents that are fully miscible with water, like ethanol, acetone, methanol, acetonitrile) do act as gate media, while non- polar solvents that are immiscible with water (e.g cyclohexane) do not. They assign that to the inevitable presence of trace amounts of dissolved salts even in 'HPLC grade' solvents. Note that the ability to undergo autoprotolysis is not required for a solvent to act as gate medium, as acetonitrile is 'aprotic', i.e. does not undergo autoprotolysis, but still acts as gate medium. Practical applications of solvents as gate media are rare, albeit an aprotic solvent may be useful for control experiments e.g. for pH sensitive TFTs. Note also that the electrochemical window of acetonitrile is larger than for water. However, the work shows that even extremely small concentrations of ionic species are sufficient to build up an EDL of high capacitance.

1.3.6 Structure and Operation Principle of Electrolyte-Gated Organic FET (EGOFET)

The above discussion suggests that electrolytes may be used as alternative to conventional dielectric insulators as gate media in TFTs. ILs and solid state electrolytes have been introduced as TFT gate media during the 2000's, eg. (IL)[39, 40]. Most significant in the context of this thesis, however, is the observation of Kergoat *et al* [26] that even pure (DI) water can gate a P3HT film and result in a transistor, the high EDL capacitance leads to low threshold (order 0.3 V), within the electrochemical window of water. Moreover, Someya *et al* showed that flowing water still can gate TFTs [41]. These discoveries pave the way to new sensor technologies for waterborne analytes, where the sample is an active part of the transducer. When suitable sensitizers are introduced (and sometimes, without), the presence of an analyte can be transduced into a change of the TFT's electrical characteristics. Much of the work reported in this thesis is concerned with the development of the water- gated TFT platform that enables such sensors.

Figure 1-15 illustrates a schematic OTFT layout typical for the work carried out here, on the example of a p- type semiconducting polymer.

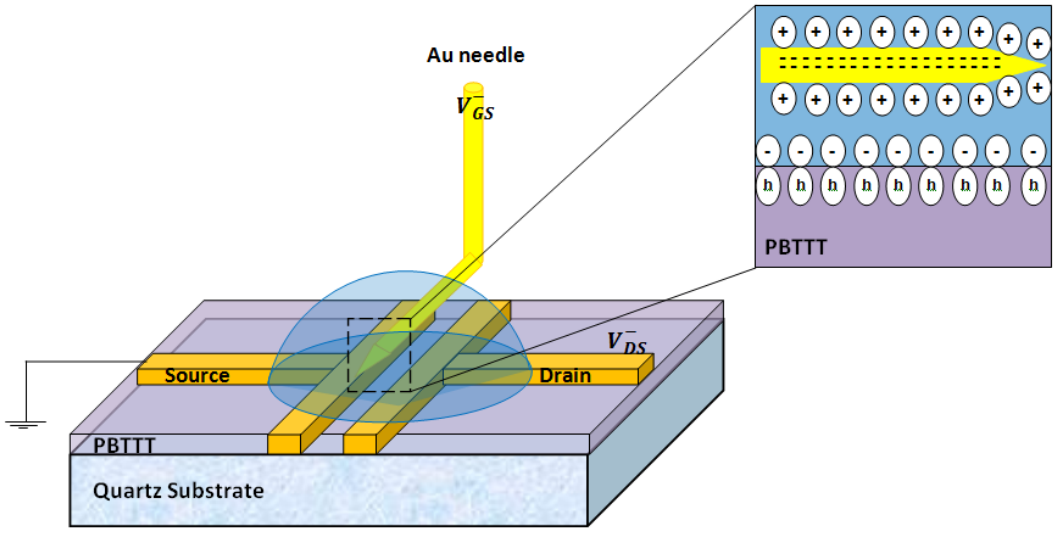

Figure 1-15: A diagram of the water- gated transistor. An inset on the right is an enlargement of the electrical double layer (EDL) interfaces after applying negative voltage, illustrating a cationic EDL at Au gate needle/water interface, a hole accumulation layer is created corresponding to an anionic *EDL* at the water/PBTTT semiconductor interface.

As a qualifying remark, the operation of such transistors is not always purely within the 'field effect' regime, in particular not when salt solutions or buffers are used as gate media, rather

than pure water [26, 41, 42]. Instead, the gate voltage may drive ions across the water/semiconductor interface and lead to electrochemical doping. Devices may therefore acts as 'organic electrochemical transistors (OECTs) in parallel to field effect gating via the EDL, shown in Figure 1-16.

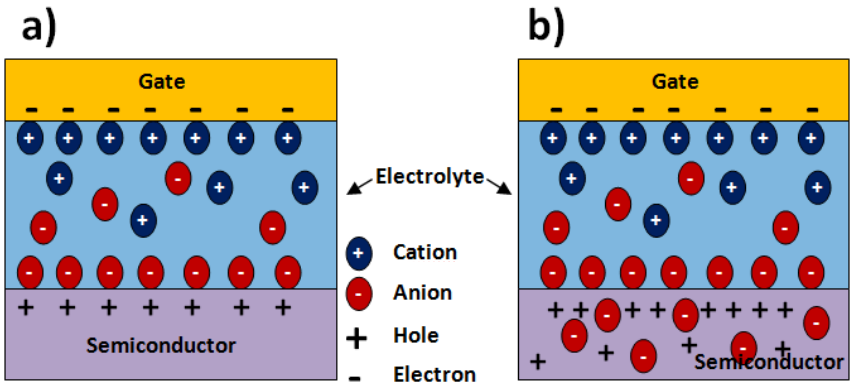

Figure 1-16: A diagram illustrating the electrolyte- gated organic semiconductor film in two cases: a) in Field Effect case, and b) in Electrochemical case [43].

For example, Olle Inganäs *et al* [42] reported on devices that operated as 'WGFET' (water gated field effect transistor' and 'OECT' (Organic electrochemical transistor' in parallel. However, in the context of this work, we have focussed on EDL gating, without electrochemical doping. This can be suppressed when the crossing of ions into the semiconductor is prevented, i.e. by the choice of impenetrable semiconductors.

1.3.7 Semiconductors for water- gated TFTs

A large number of solution- processed semiconductors have been reported, and many of them can in principle be water- gated. Here, we discuss two examples, which are known for their particularly good performance (i.e., relatively high charge carrier mobility), and relative stability, both for long term operation, and against undesired parallel OECT behaviour. Both are commercially available. The first example is a hole- transporting organic semiconducting polymer, PBTTT.

While there are more hole- than electron transporting organic semiconductors, a number of electron transporters have been demonstrated. Remarkably, however, a literature search has found no examples of water- gated n- type (electron- transporting) organic transistors. This is probably due to strong interfacial trapping of electrons in the LUMO by the O-H groups found in water. ILs that lack O-H groups can gate n- type organic semiconductors [39]. To water- gate

a solution- processed n- type TFT, we instead use an inorganic semiconductor, ZnO, that can be derived from a solution- processed precursor.

1.3.7.1 Poly(2,5-bis(3-hexadecylthiophen-2-yl)thieno[3,2-b]thiophene), (PBTTT)

The organic semiconducting polymer regioregular poly(3- hexyl thiophene) (rrP3HT), based on the thiophene unit discussed in section (1.2.1), is one of the best characterised organic semiconductors, and a well- established hole transporter with good properties. In 2006, McCulloch *et al* [44] reported on an improved material, PBTTT, which is also based on thiophene, but includes pairs of thiophene rings fused at two corners, the chemical structure is illustrated in Figure 1-17.

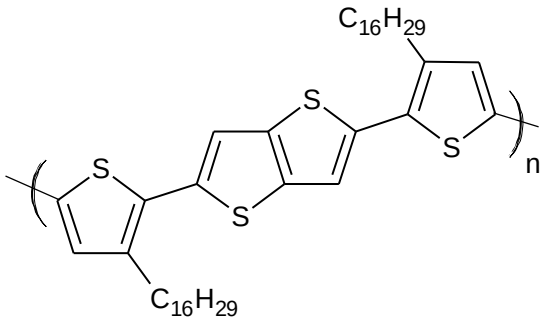

Figure 1-17: Chemical structure of semiconducting polymer poly(2,5-bis(3-hexadecylthiophen-2-yl)thieno[3,2-b]thiophene) (PBTTT).

Due to the fusion of thiophenes that was explained previously, the HOMO level in PBTTT is reduced by 0.1 eV compared to rrP3HT, as fused rings facilitate better π electron delocalisation. This leads to easier charge carrier injection, better stability against degradation, and reduces the likelihood of charge carriers getting trapped. Further, when annealed, PBTTT displays larger crystalline domains than rrP3HT, leading to higher carrier mobility 0.72 $cm^2V^{-1}s^{-1}$.

Due to its rather inflexible structure, PBTTT is only marginally soluble. We require hot chlorinated benzenes to dissolve PBTTT. On the other hand, after casting into a film, same rigid structure makes PBTTT resist penetration by waterborne cations, thus avoiding undesired OECT behaviour.

1.3.7.2 Zinc oxide (ZnO)

ZnO is a wide-bandgap II-VI semiconductor and is mostly recovered and gained from Zincite mineral which is available in the nature however these days ZnO is mostly being created synthetically. ZnO is widely used today in different applications which include, but are not

limited to, field effect transistors (FET), spintronics [45], sensors [46, 47], piezoelectricity [48] and most famously as light emitting diodes (LEDs).

ZnO is found in hexagonal form with a wurtzite crystal structure. This is a structure of Zinc and Oxygen atoms where Zinc atoms are attached to 4 oxygen atoms as shown in Figure 1-18.

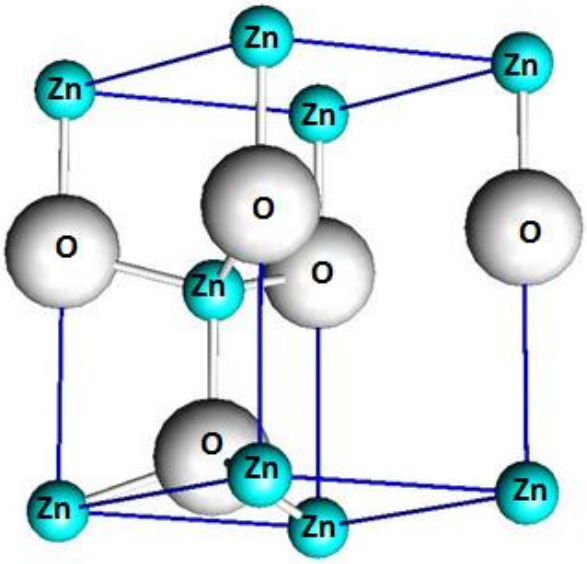

Figure 1-18: ZnO, wurtzite crystal structure

ZnO is an inorganic semiconductor, and unlike organic conductors there is no need to store it in vacuum; it will remain stable at ambient conditions and if stored in vacuum it would get doped by oxygen vacancies in its structure. ZnO is a n-type extrinsic semiconductor due to two different reasons; however, the debate of whether Zinc is dominant or Oxygen is still unsettled [49], although, for an undoped ZnO the doping is caused due to Hydrogen [50]. Due to the practically inevitable doping, and the ease of electron injection vs. the difficulty of injecting holes (see Figure 1-19), ZnO resembles organic semiconductors in the sense that it operates with one type of carriers only, in this case electrons. Nomura *at el* was amongst the first few who revealed a thin-film transistor of ZnO in the year 2003 [51]. Moreover, ZnO TFTs and hydrogenated amorphous silicon (a-Si:H) TFT when compared in terms of mobility, it shows a mobility of $\sim$12 $cm^2V^{-1}s^{-1}$ compared to 1 $cm^2V^{-1}s^{-1}$ respectively, at the same room temperature of course [52]. Finally, Li- doped ZnO reflects more stable performance in terms of electrical properties; the increased operational stability together with decreased threshold and increase mobility [53]. The observed mobility is nevertheless lower than typical found in crystalline semiconductors, which suggests that practical ZnO is largely amorphous, the wurtzite structure shown in Figure 1-18 is an idealisation.

ZnO is insoluble in organic solvents though, and cannot easily be processed from solution. However, this has been overcome by Loutfy *et al.*[54] who reported the processing of Zinc acetate (H_3C-CO-O-Zn-O-CO-CH_3) from an organic solvent, and subsequent thermal conversion into Zinc oxide (ZnO). The resulting ZnO film performed as semiconductor in thin film transistors. Mobility was in the order 5 $cm^2V^{-1}s^{-1}$ which is superior to most organic electron transporters, but still in the regime of hopping- type, rather than band- like conduction, which again suggest a largely amorphous morphology. A drawback of the soluble precursor- route is that the thermal conversion requires 450 ^oC which excludes many substrates, in particular flexible substrates.

In 2012, Al Naim has shown that precursor- route ZnO can be water- gated in TFTs [55]. However, ZnO is chemically 'amphoteric', which means it reacts with / dissolves in both acids, and bases. The long- term stability of ZnO in particular in aqueous gate media that are not at or near neutral pH (~7) is therefore doubtful.

Finally, we illustrate the electronic levels (HOMO/LUMO for PBTTT; valence Band/conduction band for ZnO) and compare to a typical contact metal, gold, Figure 1-19.

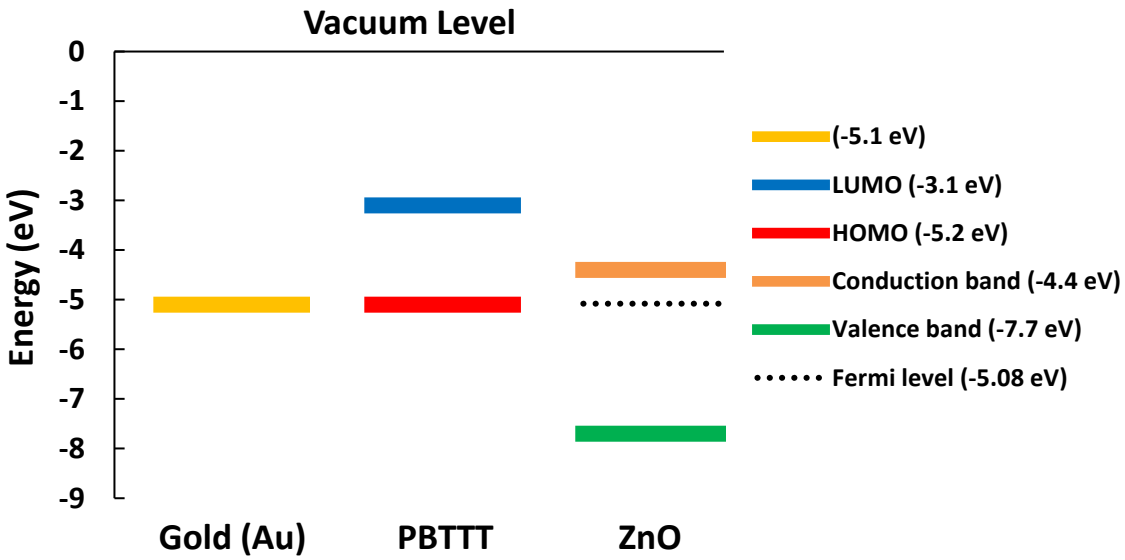

Figure 1-19: PBTT LUMO & HOMO levels, ZnO conduction & valence bands and gold electrode work function.

The work function of gold closely matches the PBTTT HOMO, which allows easy injection of holes. By contrast, despite the relatively high work function of gold, the barrier for hole injection into ZnO VB is very large, and makes hole injection near impossible. However, gold

(as well as any lower work function metal) will easily inject electrons into the ZnO CB. The location of the ZnO Fermi level close to the CB is the result of inevitable n- doping of ZnO.

The thesis is structured into 8 chapters, namely:

Chapter 1 provides an overview over organic and other solution- processed semiconductors and the physical principles of electrolyte- gated TFTs.

Chapter 2 summarises the preparation of TFT samples

Chapter 3 describes the characterisation of semiconductor morphology, and electrical characterisation methods for water gated transistors. This includes bespoke instrumentation that was developed by a previous graduate of the Sheffield group, which I adapted for my purposes.

Chapter 4 describes the development of an analyte delivery system that allows the delivery of a constant stream of water- based analyte with varying concentration for testing and calibration of water- gated TFT sensors, and the design of a bespoke flow cell.

Chapter 5 presents my results on an electrolyte- gated organic TFT that delivers exceptionally large currents.

Chapter 6 describes the development of an improved preparation route for a solution-processed precursor- route inorganic semiconductor

Chapter 7 presents the detection of waterborne amines with a water- gated TFT.

Chapter 8 summarises the thesis, and gives an outlook for potential future work.

Chapter 2
Fabrication of Thin Film Transistor (TFT) Devices

Water- gated TFT architecture

Figure 2-1 shows the architecture of an electrolyte- gated (specifically, water- gated) TFT and its parts. This can conceptually be divided into two parts: Firstly, the 'transistor substrate', which consists of a supporting substrate, source- and drain contacts, and a semiconducting material in the channel; and secondly, the gate medium / gate contact. In the case of water- or ionic liquid (IL) gated TFTs, the transistor substrate can be manufactured independently first, and the gate medium can be applied and contacted later, just before use or testing.

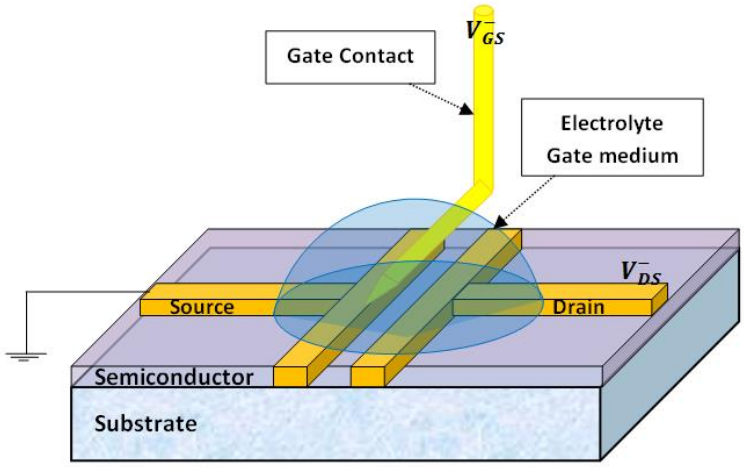

Figure 2-1: A diagram of electrolyte- gated transistor.

This chapter describes the preparation of transistor substrates used for this thesis, including both, solution- processed organic semiconductors, and precursor- route inorganic materials. This will be in the order supporting substrates (2.1), source/drain contacts (2.2), and semiconductor deposition (2.3). Finally, it describes a generic method of applying a liquid gate medium and addressing it electrically with a gate contact (2.4).

Within this thesis, I also developed more sophisticated flow cell apparatus for the delivery of waterborne analyte solutions that allows varying analyte concentration in uninterrupted flow, while continuously gating and testing electrically. This is described in detail in Chapter 4.

2.1 Supporting Substrate

To fabricate TFTs, we require a mechanically firm supporting substrate with a smooth and clean surface, to which contacts and semiconductor show reasonable adhesion. The choice

and preparation of such substrates is elaborated upon now. The surface of supporting substrates used here was always silicon dioxide (SiO_2), albeit of different morphologies: Either, SiO_2 that was formed as thermal oxide (~300 nm) on crystalline Si wafers, or amorphous SiO_2 ('Quartz') that was coated onto conventional soda lime glass. Both were purchased from Ossila (Sheffield, UK).

2.1.1 Crystalline silicon dioxide (Quartz also is silicon dioxide)

Crystalline 300 nm SiO_2 – on (P-Boron doped) Si substrates are already cut into rectangles of 2 cm x 1.5 cm size from distributed as near- circular wafers (10 cm, overall thickness 725 μm) . The SiO_2 surface was highly polished by the manufacturer, making it smooth and reflective.

2.1.2 Amorphous silicon dioxide ('Quartz')

Alternatively, we used substrates which had a 20 nm layer of synthetic quartz deposited on a conventional (soda lime) glass substrate. These substrates are optically transparent, and smooth, and were already cut into rectangles of 2 cm x 1.5 cm size, as be shown in Figure 2-2.

2.1.3 Substrate Preparation

2.1.3.1 Substrate Cutting

Crystalline SiO_2 substrates were already delivered as small rectangles and required no further cutting. However, some of the amorphous substrates need cutting into small square pieces that used as a gate substrate in flow cell, as be described in section (4.1.1). We used a Diamond-tipped glass cutter to score a groove into on the non-SiO_2 side of synthetic quartz substrate.

Moving on, dry nitrogen was used in order to blow away the residuals from scoring.

2.1.3.2 Substrates Cleaning

Cleanliness of substrate surfaces is very important for further deposition steps and therefore they must be cleaned in order to make sure that they don't result in increased off- current or non-working devices by creating poor adhesion. So, before semiconductors are deposited, substrates must be cleaned; this part would elaborate on the different cleaning techniques for substrates.

Cleaning followed a step by step process. Firstly, the substrates were cleaned using acetone with a lab-wipe so that any organic dirt etc. was removed from their surfaces; followed by the use of dry nitrogen to completely remove the residuals from the surface. The steps that followed can be broken down into two major parts, which are as follows:

Alkaline Solution Cleaning

The first major process is initiated with cleaning of the substrates of choice in alkaline solution. A detergent solution of Hellmanex cleaning fluid diluted in highly deionised (DI) water 1:100 (v/v) was used, in a Petri dish to initiate the next step in cleaning. Sonication was then done by giving the substrates a 5 minutes bath. Next, deionised water was used to wash the alkaline from the substrates. Lab-wipe was then used in order to take off the water droplets from the surfaces of the substrates; thereafter, the substrates were left to dry completely.

Isopropyl Alcohol (IPA) Cleaning

The second major process was initiated with the use of isopropyl alcohol (IPA) for the purpose of cleaning. The steps of both processes are relatively similar in procedure. The substrates were place on the Petri dish which was filled with IPA heated to 70 degrees; the substrates were dipped into this hot solvent for 5 minutes; followed by sonication in the ultrasonic bath for 5 more minutes. It was made sure that the temperature of the bath was below 75 degrees so that IPA would not boil. Clean isopropyl alcohol was then used to rinse the substrates followed by the use of lab-wipe and the hot plate to completely dry the cleaned substrates.

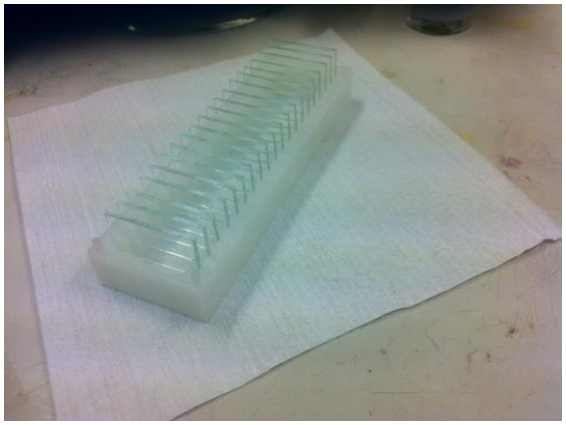

Figure 2-2: Amorphous SiO2 ('Quartz') substrates after cleaning process

Ultraviolet Light Ozone Cleaning (UV O_3 Cleaning)

The final step in the cleaning process is done in order to eliminate the possibility of minute amounts of organic pollutants still being present on the substrates of choice. For this, a 4.5 minutes process was initiated for both, silicon and the quartz substrates. Substrates were placed on a Petri dish which was loaded into the chamber of an UV- ozone cleaner (Bioforce Nanosciences., model: UV.TC.220). This creates ozone (O_3) by irradiating atmospheric oxygen with 'hard' UV from a purpose- made UV light bulb (184.9 nm wavelength). Ozone is a strong oxidising agent for all organic compounds and therefore destroys them, forming volatile compounds.

2.2 Source-Drain Contacts

2.2.1 Thermal Evaporation Deposition

Thin films, which are made of metals, are deposited usually through the process of thermal evaporation under high vacuum. For the evaporation of Gold (Au), a short Au wire is placed on a tungsten (W) boat; for the evaporation of Chromium (Cr), we used Cr- coated W rods. Tungsten (W) is a metal (hence, a conductor) with a very high melting point, which allows the melting of almost all other metals in a W boat / on the surface of a W rod without the boat/rod itself melting.

The tungsten boat or rod is connected to an electrical heater, and the entire setup is placed at the bottom of a high vacuum system (Edwards E306) equipped with suitable high vacuum gauges, Figure 2-3. At the same time, cleaned supporting substrates (cf. 2.1) are mounted face-down at the top of the same evaporator at a distance of ~15 cm, Figure 2-4. The vacuum system included a removable shutter to shield or expose substrates from/to the source. Clean substrates were loaded into the top of the evaporator and covered by Ossila source- drain shadow masks facing downwards, Figure 2-5. Masks were held in place magnetically. The vacuum system was then closed with a glass bell jar, and evacuated. Evacuation was by combining two pumps in a two stage evacuation process, a rotary pump to create a rough vacuum first, and in a second step, same pump is used for the backing of a water- cooled oil diffusion pump, which is further assisted by a cool trap. This system reaches high vacuum with a residual pressure of less than $\sim 10^{-9}$ bar.

Figure 2-3: Edwards E306 thermal evaporator.

Figure 2-4: Au evaporated and deposit Source-Drain electrodes on substrates by using shadow masks.

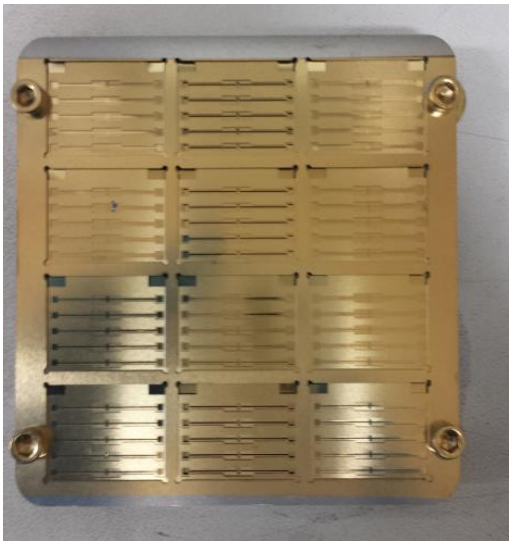

Figure 2-5: A dozen of substrates loaded into Source-Drain shadow evaporation stack.

At such low pressure, the free path length of a vapour atom or molecule is far longer than the 15 cm distance between evaporation boat and supporting substrate. This is supported by theory, equation (2-1)

$$\lambda = \frac{1}{n\pi d^2\sqrt{2}}, \qquad 2\text{-}1$$

where λ and d are the mean free path and the molecular diameter respectively, the number density of the molecules is denoted by n which is extracted from ideal gas law,

$$n = \frac{P}{k_B T}, \qquad 2\text{-}2$$

where the absolute pressure of the gas is presented by P, k_B and T are the Boltzmann constant and the absolute temperature respectively.

At a pressure of 10^{-9} bar, this gives λ = 60 m, which is far more than 15 cm. At 10^{-9} bar or less, any vapour emanating from the evaporation source will therefore reach the supporting substrate before colliding with another gas particle.

To generate vapours of Cr or Au, a high direct current (DC) is passed through the tungsten rod/boat for resistive (Joule) heating.

The rate of thin film deposition is detected by using the quartz crystal microbalance (QCM) as be seen in Figure 2-4.Once the evaporated particles cover the quartz surface, the mass of the quartz will increase leading to a decrease in the resonant frequency which is associated with the electronic oscillator over the time; so based on changes of the frequency and the known materials density, the deposited thickness is calculated. The following equation quantifies the above:

$$\frac{\delta f}{\delta m} = \gamma(f_0 - \delta f)^2, \qquad 2\text{-}3$$

where, δf and δm are frequency and mass changes respectively, resonant frequency is denoted by f_0 and γ is constant for the system.

2.2.2 Materials and Geometry

Our evaporator has two sample heaters, called channel A and B, amidst the small tungsten boat, which is associated with the Channel A, lies the gold wire. Moreover, the chromium-plated tungsten rod is placed at the Channel B, Figure 2-4. 12 of quartz substrates are loaded into a single evaporation stack, hence one evaporation batch delivers 12 supporting substrates, as be shown in Figure 2-5.

2.2.2.1 Gold (Au)

The properties of gold, like being chemically non-reactive and highly resistant towards corrosion, make it very attractive as TFT contact material. Heater current was manually regulated until a steady evaporation rate of 0.03 Angstrom/second was reached, the shutter was then removed and substrates were exposed to Au vapours. Evaporation was timed with a stopwatch to calculate thickness from known deposition rate, and exposure time; to reach120 nm, when the shutter was closed again and the heater was shut down. The work function of gold is 5.0 to 5.3 eV [56, 57]; this is one strong reason to employ gold for the p-type semiconductors under consideration as the ionization potential matches their HOMO most of the time or at least minimises injection barriers, resulting in good hole injection. Au will provide a good carrier injection layer for both, polythiophene- based organic polymers, and Zinc oxide. The deep lying conduction band of ZnO allows electron injection despite the high work function of gold, cf. the level diagram, Figure 1-19 in the previous chapter.

A drawback is that Au shows poor adhesion to silicon dioxide surfaces, which may lead to deposited gold thin films getting delaminated. The counter to the drawback, however, is the

use of other metals for thin adhesion promoting layers (like Titanium or Chromium) before depositing Au.

2.2.2.2 Chromium (Adhesion Layer)

As explained in the previous part, adhesion properties, which are very weak in gold, may lead to taking gold off the deposited gold source/drain electrodes which were placed on the cleaned substrates. As mentioned earlier, is the use of other metals for adhesion promoting layers (like Titanium or Chromium) which are deposited before the deposition of gold takes place. Cr adheres well to Silicon dioxide, and Au adheres well to Cr, so the adhesion layer mediates adhesion between Au and Silicon dioxide. The adhesion layer is deposited from Cr- plated W rods from evaporator channel B, otherwise similar as described before (but first in time, before Au). However, Cr adhesion layer is kept very thin, 5 to 7 nm.

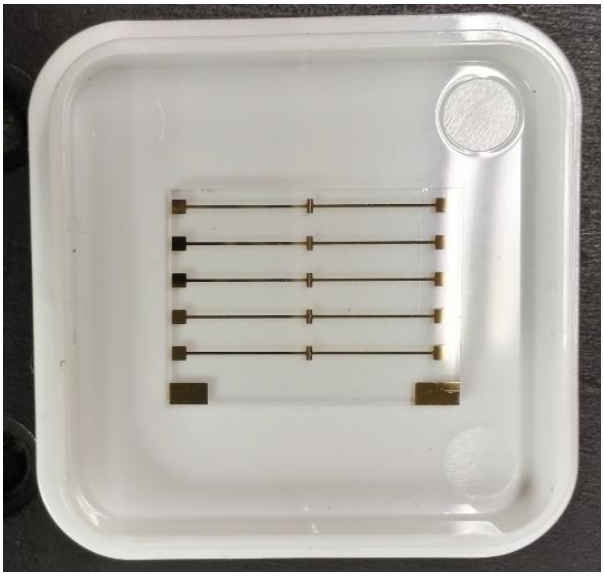

Figure 2-6: Five pairs of Source/Drain electrods of gold and Chromium (Adhesion Layer) deposition on amorphous SiO_2 ('Quartz') substrates.

2.2.2.3 Transistor substrate geometry

As a result of the two- stage contact evaporation procedure, we have Cr/Au contacts deposited onto the supporting substrate that are in the shape of the shadows of the defining mask. This shape is shown to scale in Figure 2-6 and Figure 2-7:

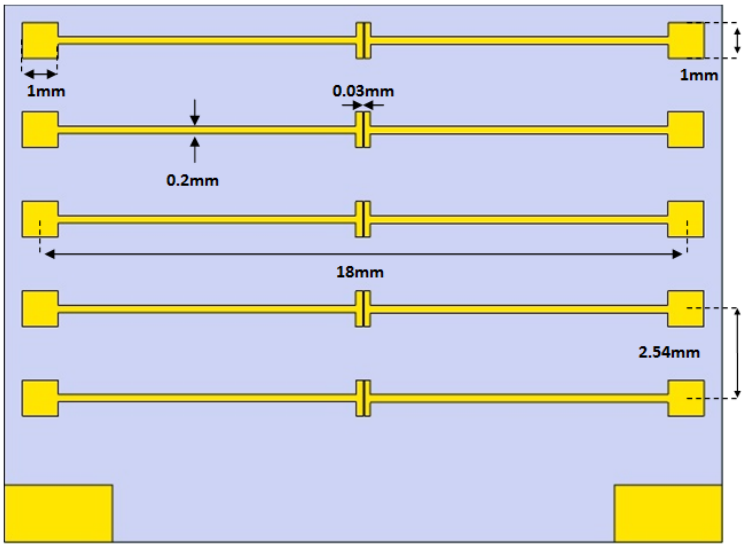

Figure 2-7: Transistor substrate geometry [58].

The shadow mask defines five separate transistor substrates on every supporting substrate with metal source / drain contacts defining a transistor channel of width W = 1 mm / length L = 30 μm, geometry factor W/L = 33. Source and drain can be addressed from a distant 1.0 mm^2 contact pad that is linked to source/drain via a thin metal line ('wire') of length 16.57 mm running from contact pad to source / drain.

TFT substrates are now ready for the deposition of the semiconductor, leading to five independent transistor substrates on each supporting substrate.

2.3 Thin Film Deposition

2.3.1 Spin Coating

Spin Coating is a process that allows casting thin films of a material from a solution. Spin coating is a convenient method that allows the coating of large areas with films of uniform thickness without the need for evaporators. The desire to find or synthesise functional materials (in particular, polymers, that can not be evaporated) that are soluble is driven by the ease of processing afforded by spin coating, and other solution- based methods (e.g. spray coating or printing).

On the laboratory scale, typically, a few microlitres of solution are placed on the chosen substrate that is placed on a turntable (also referred to as chuck) of small size. Substrates are held in place by vacuum suction from below to minimize or eliminate possible movements of the substrates. The chuck is machined from *Polytetrafluoroethylene* PTFE (also referred to as

Teflon) for its resistance to solvents, and ease of cleaning. The operator is protected by a transparent cover lid on top of the cavity as the turntable is set into rotating motion. Moisture and ambient oxygen however can cause problems for the deposited thin films; in order to eliminate that dry nitrogen is used within the spinning chamber while the spin coating is in process. Spin coating can be by static or dynamic deposition. Static deposition refers to deposition of the solution through the small hole in the lid before the onset of spinning whereas dynamic deposition refers to deposition of the solution through the small hole in the lid onto a spinning substrate.

The process of spin coating revolves around the concept of centrifugal force which is utilized for the solution spread as well as coating of the thin layer on the substrates. The solvent evaporates under the 'wind' of fast rotation and leaves behind a film of the solute.

When spinning polymer solutions, using a slowly evaporating (less volatile) solvent helps in leaving necessary time for polymers to order and crystallize, which will lead to higher carrier mobility as be described in section (1.2.3).

Solvent and other spin parameters also impact the thickness of the resulting films thickness can be known roughly using the following equation/formula [16]:

$$t \propto \frac{c\eta(c)}{\sqrt{\omega}}, \qquad 2\text{-}4$$

where the resultant thickness is denoted by t, c and $\eta(c)$ are the solution concentration and a viscosity which depends on the concentration respectively and the 'spin speed' is presented by ω. Strictly speaking, ω is an angular velocity, usually reported in 'revolutions per minute' (rpm). Typical 'spin speeds' are 1000 to 4000 rpm.

Substrates, solvent and other factors including adhesion affect the constant in the above equation.

2.3.2 Thin Film Semiconductors

Within the framework of this thesis, we used spin coating to deposit semiconducting films belonging to two different 'families' onto the previously prepared supporting substrates: Firstly, an organic semiconducting polymer (PBTTT), and secondly, a 'precursor route' inorganic semiconductor, Zinc oxide (ZnO). In the latter case, spin coating does not deposit the semiconductor directly, as it is not easily soluble. Instead, a solution of an organic

precursor to ZnO, Zinc acetate (ZnAc) is deposited, which is subsequently thermally converted to ZnO. Both materials and the precursor process were introduced in section (1.3.7.1) for PBTTT and section (1.3.7.2) for ZnO.

2.3.2.1 Deposition of Polymers (PBTTT-C16)

McCulloch *et al* was among the initiators of the concept and usage of poly(2,5-bis(3-alkylthiophene-2-yl)thieno[3,2-b]thiophenes), which is also referred to as PBTTT; this was done in the year 2006 [44]. Figure 1-17 which was included in Chapter 1, reflects the schematics of PBTTT. Firstly, the employed fused thiophene unit helps in increasing the ionization potential which results in strong environmental stability since the oxidation of the molecule is inhibited. Secondly, McCulloch *et al* were of the opinion that highly-ordered crystalline domains can be formed by the incorporation of rotational invariance of fused rings; this resulted into the increased mobility of the charge carriers.

In this study, PBTTT-C16 sourced from *Ossila* in the powdered state and its ionization potential, as per the data sheet, is 5.1 eV [58]. While its rigid backbone structure makes PBTTT an excellent organic semiconductor, it also makes it difficult to dissolve. PBTTT required heated 1, 2 dichlorobenzene (DCB) and vigorous stirring with a magnetic stirrer to dissolve, we used a concentration of 7 mg PBTTT per mL DCB. PBTTT films were spun immediately from hot solvent to avoid precipitation. Elaboration on the deposition of polymers would further be made in Chapter 5 and Chapter 7.

2.3.2.2 Deposition of Zinc Oxide (ZnO)

As mentioned previously, ZnO films were prepared via thermal conversion of the precursor, Zinc acetate (ZnAc). ZnAc dihydrate was sourced from Aldrich and dissolved in a suitable (i.e., polar) solvent. Originally we used 22 mg/mL ZnAc in Ethanol. Note that polymeric nature of PBTTT leads to more viscous solutions at low weigh, and hence to higher film thickness according to equation 2-4. For ZnAc we need to compensate by higher weigh- in. Ethanol is not a particularly good solvent for ZnAc though, in Chapter 6 we will report on alternative processing solvents that lead to better TFTs.

After spin casting a film of ZnAc onto a supporting substrate, this was then placed on a hotplate at 450 ^{o}C for 12 minutes under ambient air. This affected the thermal conversion of ZnAc into ZnO.

2.4 Gating transistor substrates

After finalising the above described procedure, we have five independent transistor substrates on every support substrate. Each transistor substrate consists of source- and a drain electrodes separated by a semiconducting-channel.

To complete the transistors, we still require the application of a gate medium, which is electrically addressed by a gate electrode. Within this thesis, the gate medium was always an electrolyte, e.g. water, or an ionic liquid [26, 59].

Sometimes, transistors were completed simply by applying a droplet of liquid gate medium onto a transistor substrate using a pipette, and contacting with a 'gate needle'. This was a tungsten, or gold- plated, needle bent into L- shape, which was immersed into the gate droplet with the foot of the L overlapping the channel of the transistor substrate, i.e. running along the width of the channel.

Alternatively, to test transistors as sensors for waterborne analytes, a bespoke flow cell and pump system was designed and built within this thesis, which allows for the delivery of a continuous stream of gate medium with varying concentrations of analyte. Gating is via an evaporated gold strip on a separate substrate, Figure 2-8. The construction of this system is one important success of my work and it is therefore described in detail in Chapter 4. The flow cell system has helped to establish PBTTT- based TFTs as sensor devices for waterborne amines; these results are reported in Chapter 7 of this thesis.

Figure 2-8: A dozen of substrates loaded into Gate shadow mask (Left) and Top –gate with gold and Chromium (Adhesion Layer) deposition which planned to compatible to flow cell sandwich design (Right)

Chapter 3
Characterisation of thin film transistor materials and devices

The following chapter describes experimental characterization methods used in this work, divided into two parts: section (3.1) introduces the methods used to characterise the morphology and electronic properties of semiconducting films used in this work. Section (3.2) describes the electrical characterization of thin film transistor devices (TFTs), including real-time characterization when TFTs are used as sensors, to work in parallel with the analyte delivery system to be introduced in Chapter 4.

3.1 Characterising thin film morphology and electronic properties

After depositing thin semiconducting films onto TFT substrates, as described in Chapter 2, but before characterizing TFTs for their electrical characteristics (3.2), we inspected deposited films for their morphology and basic properties. This is partly 'quality control' to exclude trivial preparation errors, e.g. poor coverage of the TFT channel with semiconductor, but also to clarify morphological consequences of different preparation methods that correlate to electrical performance, as revealed by the methods described in section (3.2). Such correlation was later made e.g. in Chapter 6.

The methods used here include optical microscopy (3.1.1), profilometry (3.1.2), scanning electron microscopy (SEM) (3.1.3), and X-ray photoelectron spectroscopy (3.1.4).

3.1.1 Optical Microscopy

After fabricating devices and before depositing films, these were routinely inspected with a conventional optical microscope. We used a conventional Nikon optical microscope with the ability to zoom up to 100x magnification. The microscope could work in transmission or reflection mode (lighting from below / above). The purpose of this initial characterization was detecting any problems with the device fabrication like shorts between source and drain electrodes; also it helped in evaluating the alignment of the shadow mask in the previous evaporation.

3.1.2 Surface Profilometry

In order to quantify the deposited films' thickness, we used a Veeco Dektak³ ST Surface profilometer as an auxiliary tool. The instrument works by lowering a Stylus onto a sample surface that scans the surface that is under consideration and investigation into one direction.

A computer- controlled feedback loop samples and processes the electrical signals that are generated from the stylus's motion and records a one- dimensional height profile with a height resolution of 1 nm. The surface profilometer can be likened to a one- dimensional AFM. To measure the thickness of a soft film on a hard susbtrate, the film is first deliberately scratched with a scalpel; the stylus then scans across the resulting groove. The depth of the groove equals the film thickness. Also, the quartz microbalance measuring thickness during contact evaporation (see previous section (2.2.1)) was calibrated by profilometer measurement of resulting contact thickness after completed evaporation.

3.1.3 Scanning Electron Microscopy (SEM)

In order to test the sample's surface that is under consideration a focused electron beam scan is done through employing electron microscopy; SEM is one of the widely used types of electron microscopy. In SEM, an incident beam excites Secondary electrons, which are sampled by a detector, Reconstruction of the surface's image can be done through the readout electronics (specifically in the SEM equipments) through employing a digital signal processing software. A high vacuum environment is imperative for SEM characterization.

As the incident electron builds up surface charges, the SEM technique relies in a certain level of conductivity of probed samples to disperse such charges by electrically grounding them; otherwise resulting images would be distorted. It is therefore limited to conductive samples, including semiconductors. We here applied it to ZnO only, using an SEM facility based at a research partner, King Faisal University in Al-Ahsa, Saudi Arabia. Primary beam energy was 15 keV, delivering magnifications from (50,000 to 85,000) and resolution of less than 10 nm. SEM surface characterization established the morphological features that provide the link between processing conditions and resulting performance of ZnO semiconducting films reported in Chapter 6.

3.1.4 X-ray Photoelectron Spectroscopy (XPS)

X-ray Photoelectron Spectroscopy effectively extends the photoelectric effect to deep- lying atomic orbitals. The aim and objective of X-ray Photoelectron Spectroscopy is to identify and determine elements' chemical state on the surface of a thin film [60] by examining the small shifts in their energy levels resulting when the atom engages in different chemical bonds. It is therefore also known as 'ESCA' (electron spectroscopy for chemical analysis).

For XPS, an X- ray beam is projected onto a surface, and induces the release of photoelectrons from low- lying electronic shells ('core electrons'). The kinetic energy E_k of such photoelectrons is detected. X-ray photoelectron energy is given theoretically by equation (3-1):

$$E_k = hv - E_b - \varphi, \qquad 3\text{-}1$$

wherein hv is the energy of incident X-rays, φ is the spectrometer (not the sample) work function, and E_b is the binding energy of the core electronic level. This allows precise determination of E_b, which shifts slightly in response to the 'parent' atoms' chemical state. By comparing measured E_b to known E_b taken on standard compounds of the same atom, surface chemistry can be determined. Typical E_b are e.g. ~530 eV for oxygen 1s electrons, and (1020 // 1045) eV for Zinc $2p_{1/2}$ // $2p_{3/2}$ electrons, typical chemical shifts are less than 2 eV, which demands for good resolution.

In addition to the release of photoelectrons, the incident X-ray beam may also cause X-ray fluorescence, or the emission of Auger electrons, from the irradiated surface. All three processes are illustrated schematically in Figure 3-1 However the latter two are not used in XPS.

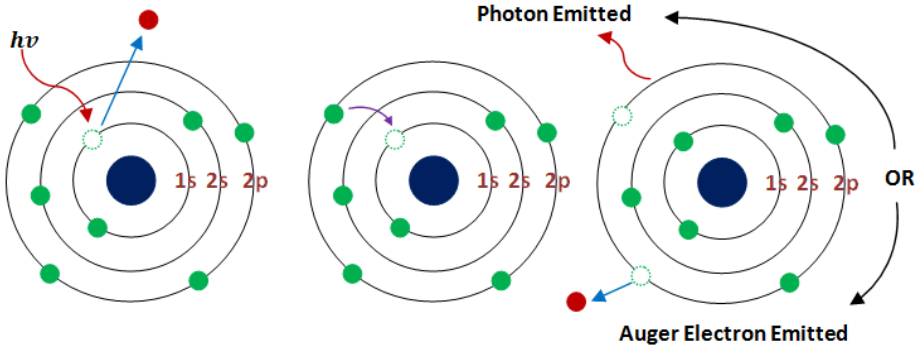

Figure 3-1: Photoelectrons releasing from low- lying electronic shells ('core electrons')

We here again used the XPS facility at our research partners at King Faisal University, Al-Ahsa, Saudi Arabia.

3.2 Electrical Characterisation of thin film transistors

To assess the quality of a thin film transistor, and to monitor its performance as a sensor device, it needs to be characterized for its electrical performance; in the latter case, this characterization has to be repeated continuously in real time to follow the TFT's response to analyte exposure.

There are two standard characteristics which were induced with the fabricated devices to identify the resulting drain current as a function of drain- and gate voltage, namely: output and transfer characteristics, cf. section (1.3.4). Conventional TFT characterization methods to determine output- and transfer characteristics are described in section (3.2.1). For The necessary measurement and evaluation while monitoring and identifying the presence of an analyte in real-time, previous graduates from our group have developed bespoke equipment that is elaborated in (3.2.2). While the preparation and device architecture of electrolyte- gated TFTs is different from 'dry' gated TFTs, the principles of measurement are the same. We did however adapt measurement protocols, as electrolyte- gated TFTs typically work at low (< 1 V) voltages.

3.2.1 Source Measure Units

To characterise TFT within this study, we used a pair of Keithley 2400 source measure units. These can in principle be used in two ways: Either, as programmable voltage source, delivering and measuring the resulting current, or as programmable current source, applying and measuring the voltage required to drive the set current. Within this study, we only use the first (voltage source / current meter) mode. The units were linked by coaxial cables to two Suss microtec PH100 probe heads that could position two needles (Gold or Tungsten). These were used to contact the TFT drain contact, linking it to the 'drain' Keithley, or the electrolyte droplet via an L- shaped contact needle' linking it to the 'gate' Keithley. A third probehead / contact needle was used to link TFT source contact to electrical ground. They set up is illustrated in Figure 3-2.

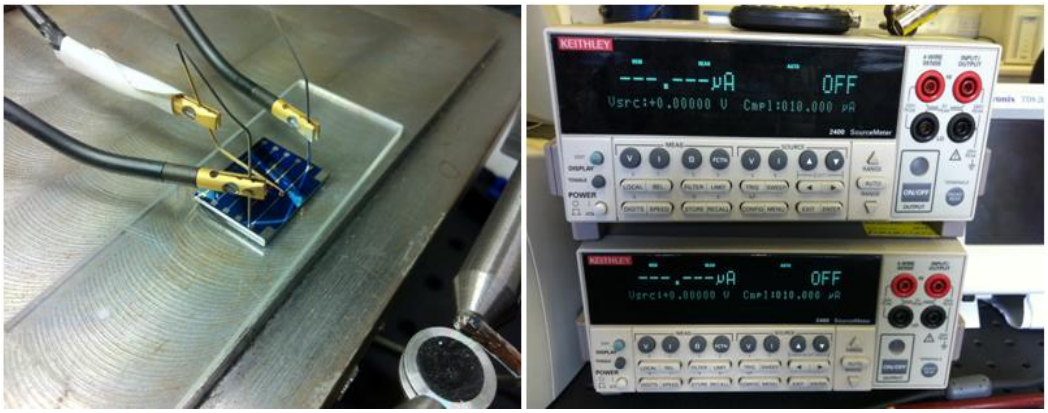

Figure 3-2: Source, drain and gate probes (Left) are connected to Keithley 2400 source measure units (Right) Water gated-TFT.

Keithleys were linked to a PC via GPIB-PCI cables and an experimental protocol of application of drain and gate voltages / measurement of resulting TFT drain currents was driven by a bespoke LabView software.

Separate modes are used by the software, to differentiate among the characterisations of output as well as transfer characteristics. Accordingly, parameters could be selected in the software, including which voltage to sweep (drain or gate voltage), the number of voltage sweeps, the range of the voltages, the voltage step size, delay time between the steps etc. Results are presented on screen in real time and can be exported as data files for later analysis, if we like to find the threshold and the mobility.

3.2.1.1 Output Characteristics

In order to measure output characteristics, drain voltage V_D is swept in a number of small steps beginning from zero up to a maximum modulus of V_D, with the appropriate polarity (positive for electron transport, negative for hole transport), and sometimes back to zero in reversed steps, while gate voltage V_G remains fixed. Resulting drain current I_D is recorded for each step. The procedure is then repeated at a different gate voltage, eventually resulting in a family of $I_D(V_D)$ characteristics parametric in V_G, which is known as the TFT's output characteristics. A thing that should be kept in mind is to not use voltages that exceed the electrolyte electrochemical window.

Output characteristics can be analysed quantitatively, but they are particularly useful to diagnose compliance with, or deviation from, theoretical behaviour, as presented in section (1.3.4). An example here could be sublinear behaviour in the supposedly linear part of the output characteristics, which indicates contact problems due to the injection that is not ideal.

The problem known as doping in the TFT's could also be diagnosed when the value of the drain current I_D still increases gradually in the saturation region for high drain voltages V_D. A gate leakage current is revealed when the output curve does not intersect the (0 V_D, 0 I_D) particularly for high gate voltage. Impurities which could be in the TFT bulk or at the interface of the insulator and the semiconductor can also be known in the problems such as hysteresis.

An example of a near- ideal output characteristic for a water- gated TFT recorded with our set up is shown in Figure 3-3.

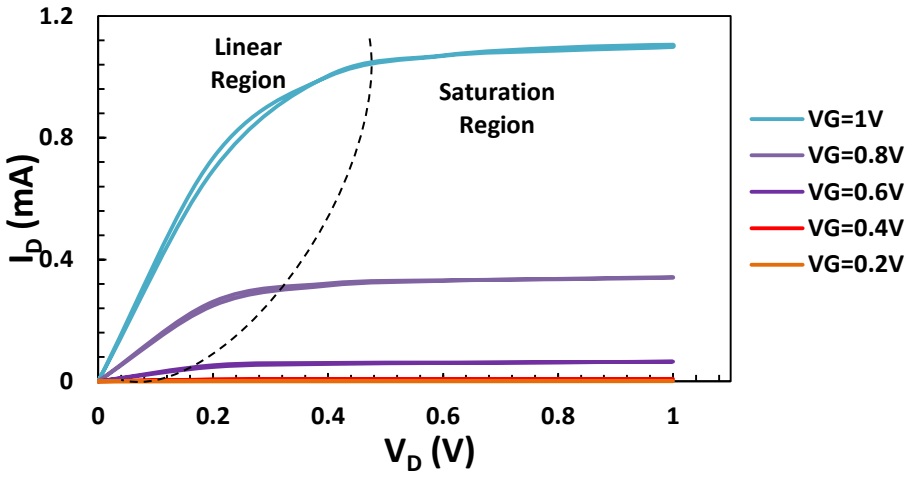

Figure 3-3: Near - ideal output characteristic for a water- gated TFT recorded with our set up

3.2.1.2 Transfer Characteristics

Coming to transfer characteristics, the gate voltage V_G sweeps with drain voltage V_D fixed. The linear transfer characteristics is extracted when small value of drain voltage ($V_{G,max} >> V_D$) is applied. The saturated transfer characteristic is measured by applying large values of drain voltage ($V_{G,max} < V_D$). Transfer characteristics are presented as graphs of I_D vs. V_G; for the saturated transfer characteristics I_D is often presented twice, once on a logarithmic scale, and once on a square root scale. This is in response to the equations for saturated drain current and subthreshold behaviour, presented in section (1.3.4). As be shown in Figure 3-4, the saturated transfer characteristics on both scales.

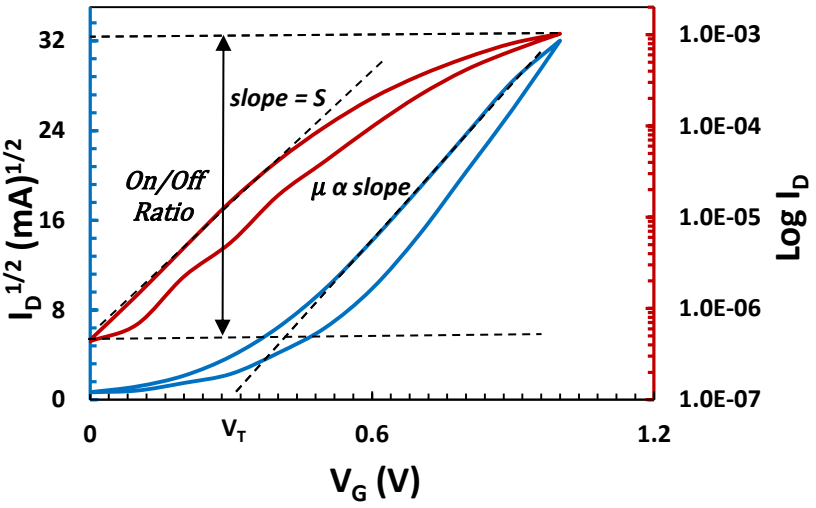

Figure 3-4: The saturated transfer characteristics on a logarithmic scale (red), and on a square root scale (blue)

Transfer characteristics are evaluated quantitatively [61] to find the key performance parameters of the TFT's as shown in Figure 3-4; this includes carrier mobility, the threshold voltage V_T, (inverse) subthreshold slope S (S^{-1}) and on/off ratio. For carrier mobility and threshold, we fit a straight line to the saturated drain current in square root ($I_{D,sat}^{1/2}$) presentation at high gate voltages. The intercept of this line with zero $I_{D,sat}^{1/2}$ is the TFT's threshold voltage, V_T. The carrier mobility can also be known by entering the measured slope of the fitted straight line into equation (1-17), mobility is proportional to this slope. The inverse subthreshold slope is found from fitting a straight line to the $log(I_D)$ vs. V_G characteristic at voltages below threshold. Straight line slope gives by how many factors- of- ten ('decades') drain current increases per unit gate voltage increase in the subthreshold regime. Its inverse, in units Volts/decade (or mV/decade) is known as inverse subthreshold slope or subthreshold swing, S^{-1}. S^{-1} is linked to traps by TFT theory, cf. section (1.3.4). The transistor's 'on/off ratio' is also read from the $log(I_D)$ scale as the ratio of the highest to lowest recorded drain current.

Most quantitative TFT data quoted in this thesis were evaluated as described above, using the following equations:

For on/off ratio, equation (3-2)

$$\frac{I_{on}}{I_{off}} = \frac{I_{D,V_D=max,V_G=max}}{I_{D,V_D=max,V_G=0}}. \qquad 3\text{-}2$$

From transistor theory (section (1.3.4), equation 1-17), the following equation can be derived:

$$Slope = \left(\mu C_i \frac{W}{2L}\right)^{\frac{1}{2}}, \qquad 3\text{-}3$$

wherein 'slope' stands for the slope of the line fitted to $I_{D,sat}^{1/2}$ vs. V_G saturated transfer characteristic. When we make mobility the subject of the equation, we get equation (3-4)

$$\mu = \frac{2L}{C_i W} Slope^2, \qquad 3\text{-}4$$

Which allows calculation of carrier mobility μ from a graphically extracted slope, if TFT geometry *W/L* and the specific capacitance C_i are known.

3.2.1.3 Hysteresis

The phenomena and mechanism that is responsible for the short-term and temporary shifts in the OFET's characteristics, like transfer or output, is so-called hysteresis. The time laps between the measurement points together with the voltage application time and the sweep direction of the voltage are the characteristics on which the shift in the OFET is dependent [62]. Hysteresis can be measured when two voltage sweeps are applied then their curves are plotted in a loop; where one of them has to have an increasing voltage while the other has to have a decreasing voltage sweep direction. Hysteresis is not explained by the TFT theory presented in section (1.3.4), but it is clearly visible in Figure 3-4. Figure 3-5 illustrates hysteresis in a saturated transfer characteristic plotted on a linear drain current scale.

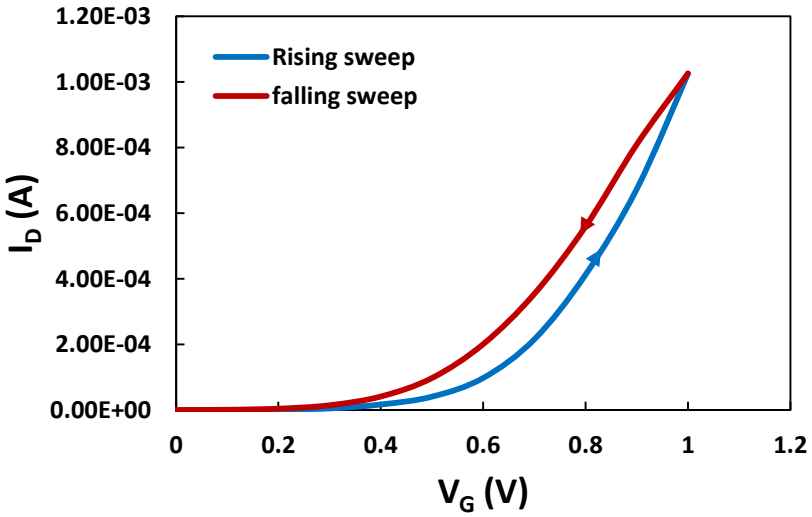

Figure 3-5: An illustrating 'anticlockwise' hysteresis in a saturated transfer characteristic plotted on a linear drain current scale

Hysteresis mechanism is related to the traps which are found in interface of the semiconductor and the insulator and mainly presented in the bulk of semiconductor [63]. To detect the presence

of hysteresis it is imperative to take help from the IEEE standard on the organic transistors which do the job through the two types of voltage applications namely the rising and the falling which refer to voltage application from off to on and voltage application from on to off respectively [64]. In this work, both the rising and falling voltage were applied on all devices under consideration and the measurement of parameters of OFETs was done in the study through the data point obtained from the falling voltage sweep (the sweep directed towards zero V_D).

3.2.2 Real time TFT characterisation

While the method described in (3.2.1) allows for a comprehensive characterization of TFTs, it does rely in detailed analysis of measured characteristics after measurements were recorded. However, in the context of TFT sensor devices, these should respond to changing analyte concentration in real time. This calls for a continuous TFT characterization method that shows TFT parameters in real time.

Such methods have been developed by prior graduates of the Sheffield TFT group. Lee Hague *et al* [4] initiated the use of *I-V* converter systems with sinusoidal voltage drive from the source contact, which affords measuring of the saturated transfer characteristics in real-time Antonis Dragoneas *et al* [5] built and developed many modifications in this *I-V* converter system, interfaced it to a PC with LabVIEW software, and developed a user- friendly interface to set measurement parameters, drive source voltage, and record and analyse resulting saturated transfer characteristics. The following sections would elaborate on the parameters calculation, operations and electrical circuit of *I-V* converter system.

3.2.2.1 Electrical Circuit and Operation

At the heart of the *I-V* converter based characterization system is the electric circuit shown in Figure 3-6.

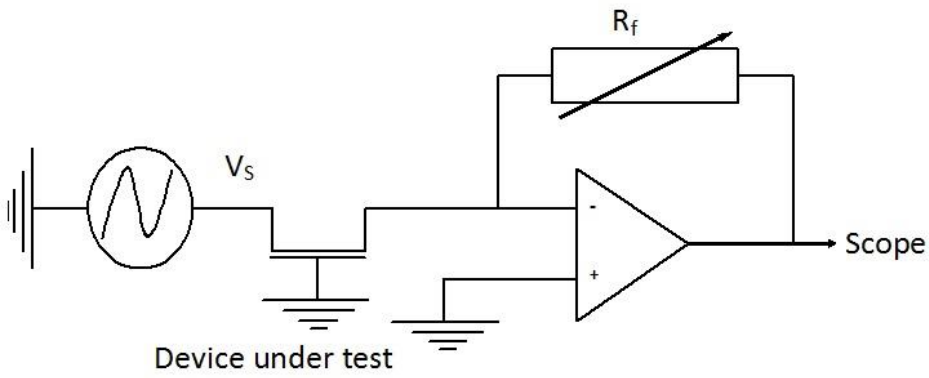

Figure 3-6: I-V converter measurement system scheme for saturation transfer characteristics

Other than in conventional characterization, here the TFT source contact is driven by a sinusoidal voltage from a programmable signal generator, $V_S(t)$. Gate of the TFT is connected to electrical ground and drain is linked to the input of a current-voltage converter, *i.e.* the inverting input of a high input impedance operational amplifier (*op-amp*) with a variable feedback resistor, R_f, between output and inverting input, while op-amp non- inverting input is grounded. This configuration establishes a virtual ground at the inverting input, hence both TFT drain and gate are effectively grounded. Note that applying positive V_S with drain and gate grounded is electrically equivalent to a grounded source with negative voltages equal to $-V_S$ applied to both drain, and ground. As V_D and V_G are always effectively equal, sinusoidal V_S therefore sweeps out the TFT's saturated transfer characteristic parametric in time. The resulting drain current, I_D, is sunk into the inverting input. Virtual ground at the inverting input is maintained with the help of the op-amps output voltage V_{out}, which is given by the *I-V* converter equation (3-5 (a))

$$V_{out} = -R_f I_{D,sat} \, , \qquad \text{3-5 (a)}$$

V_{out} is therefore proportional to I_D, and recording I_D vs. time under sinusoidal V_S drive shows a saturated transfer characteristic parametric in time. The inversion (minus sign) is a characteristic of *I-V* converters. Dragoneas *et al.* later implemented a modified version of circuit Figure 3-6 which amplified V_{out} 10- fold [5], equation (3.5 (b)).

$$V_{out} = -10 R_f I_{D,sat} \, . \qquad \text{3-5 (b)}$$

Figure 3-7 shows a two- channel oscilloscope shot of a water- gated TFT as characterized with the circuit Figure 3-6; source drive voltage V_S is here called "V_{in}". Note the V_{in} channel was inverted to account for the effective inversion of TFT operation that results from source drive.

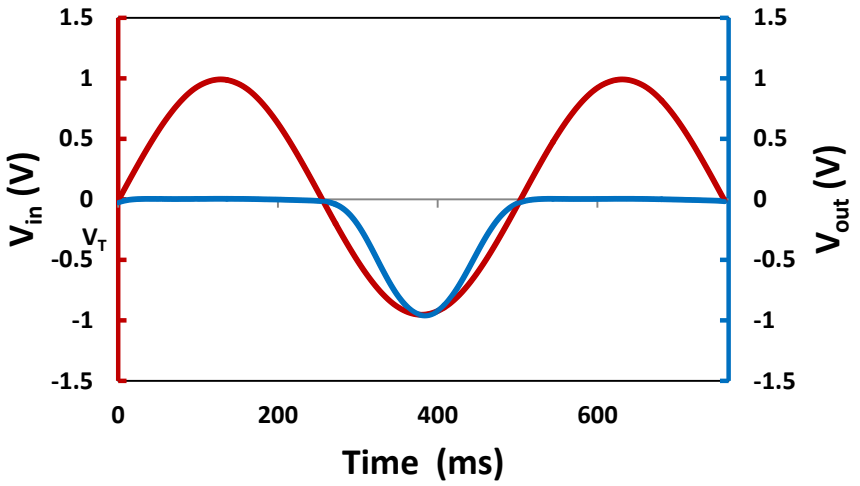

Figure 3-7: Saturated transfer characteristics (Blue) parameteric in time and V_S applied to the source (Red)

TFT drain current can be calculated with the help of equation (3-5), the result is shown in Figure 3-8.

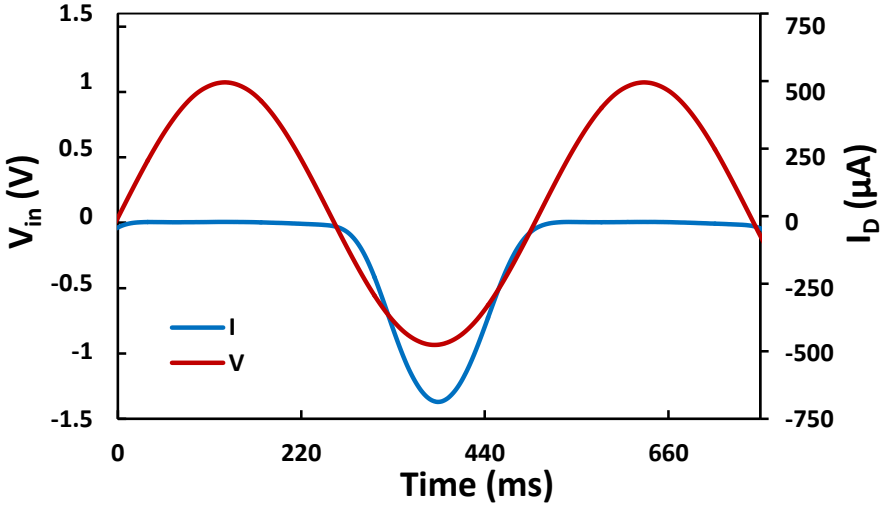

Figure 3-8: Saturated drain current (Blue) parameteric in time and V_S applied to the source (Red).

Note the low characterization frequency (2 Hz) to remain in quasi- static conditions, and the maximum V_S of 1V to stay within the electrochemical window. In practical characterization, the feedback resistor R_f (i.e., the 'transimpedance gain' of the *I-V* converter) is adjusted to make V_{out} similar in magnitude to V_S; depending on what TFT is used that may require different orders- of- magnitude for R_f. We therefore employed a dial- in 'resistance box' for R_f.

Figure 3-8 represents a saturated transfer characteristic parametric in time. We observe low current in reverse bias, and at voltages below threshold, and an approximately $\sin^2$ shape above threshold, reflecting the quadratic dependency of saturated I_D on ($V_G - V_T$). In principle, the time parameter can be eliminated to reveal saturated transfer in the conventional presentation, $I_D(V_G)$, but we prefer to analyse parametric characteristics directly. Due to the grounding of the gate electrode, *I-V* converter based characterization is robust against interference from gate leakage currents, as these would be sunk directly into (real) ground.

3.2.2.2 *I-V* converter Application to Electrolyte-gated TFTs

Shifting in phase can be witnessed when the current/voltage converter scheme is applied onto the electrolyte-gated TFTs, i.e. the V_{out} / I_D current peak slightly lags behind the V_{in}/V_S peak, sometimes even at 2 Hz. This was not observed when same method was applied to a 'dry' (dielectric insulator) gated TFT at 70 Hz [4]. We assign this lag to the slow build- up of the electric double layer, which was observed previously in capacitance vs. frequency studies, e.g. by Berggren *et al* [26]. Thus, in order to avoid this issue, a low frequency was applied to the system which was about 0.5 - 1 Hz. The gate medium's electrolytic decomposition was avoided by keeping the maximum of drive voltage to 1.0V; which was equally compatible to all electrolytes under consideration.

3.2.2.3 Calculation of Saturated Drain Current

Oscilloscope data as shown in Figure 3-7 are used in order to calculate the maximum (by modulus) saturated drain current; this however is based upon the equation (3-5 (b)) presented earlier:

$$I_{D,sat} = \frac{V_{out,max}}{10R_f} . \qquad 3\text{-}6$$

Alternatively, $I_{D\ sat,max}$ can be read directly from charts such as Figure 3-8, where the entire V_{out} trace has already been converted into drain current.

3.2.2.4 Calculation of on/off Ratio

To calculate the on/off ratio of TFTs the maximum and minimum currents were read from the drain current trace in oscilloscope screen shots such as shown in Figure 3-7. For better accuracy, these were rather taken from the results spreadsheet that can be exported from a digital oscilloscope.

For n-type, the maximum output voltage is divided by minimum output voltage where one is positive and the other is negative respectively. The minimum and maximum points are switched from numerator to denominator for p-type; as can be seen in the following equations:

For *n*-type $$\frac{I_{on}}{I_{off}} = \left|\frac{V_{out,max}}{V_{out,min}}\right|, \quad 3\text{-}7$$

For *p*-type $$\frac{I_{on}}{I_{off}} = \left|\frac{V_{out,min}}{V_{out,max}}\right|. \quad 3\text{-}8$$

3.2.2.5 Calculation of Threshold voltage and mobility

In order to extract mobility and the threshold voltage from *I-V* converter measurements, there are two unique ways which will be discussed below.

3.2.2.5.1 Eliminating the time parameter

The previous discussion showed the data from the *I-V* converter parametric in time, Figure 3-8. Moving forward, we can eliminate the parameter time, and use that same data points to plot a saturated transfer characteristic in the conventional form, as can be seen in Figure 3-9.

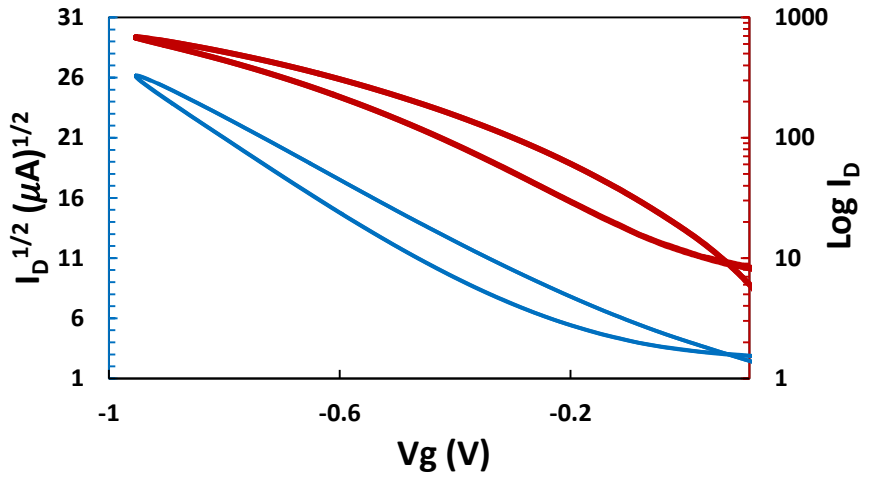

Figure 3-9: Saturated transfer characteristics on a logarithmic scale (red), and on a square root scale (blue) after eliminating the time parameter.

Note, V_{out} has first been converted into drain current using equation (3-6), and then root or logarithm has been taken to present the saturated transfer characteristic in the same form as discussed earlier for source/meter based measurements, Figure 3-4. Figure 3-9 can now be evaluated mobility and threshold voltage; as explained earlier in section (3.2.1.2). There is a

small difference between the characteristics of standard transfer and the converted saturated transfer data. Considering the converted saturated transfer data we see that V_{DS} is equal to V_{GS}, rather than larger (in modulus). The saturation condition is fulfilled as long as only 'normally off' FETs are under consideration of the study. This means TFTs with negative threshold in the p-type semiconductors and positive threshold in the n-type semiconductors. This is observed in most cases though and quantitative agreement with source/measure unit characterization is good [4].

3.2.2.5.2 Direct evaluation of parametric characteristics

This method uses the characteristics parametric in time directly to determine mobility and the threshold voltage from the data recovered from the *I-V* converter; eliminating time is not needed. Figure 3-10 shows fitting a line to $V_{out}(t)$ in the rising flank, threshold voltage V_T is then taken as the source voltage ('V_{in}') at the point of intercept of this line with the time axis. This V_T can then be used to calculate the mobility through the below equation (3-9):

$$\mu = \frac{1}{10 R_f C_i} \times \frac{2L}{W} \times \frac{|V_{out,max}|}{(|V_0| - |V_T|)^2} . \qquad 3\text{-}9$$

Equation (3-9) results from combining previous equations. $V_{out,max}$ refers to the-peak of output voltage, whereas V_0 refers to the input (source) voltage's amplitude from the sinusoidal drive. Both of them can be similar by making necessary adjustments through feedback resistance.

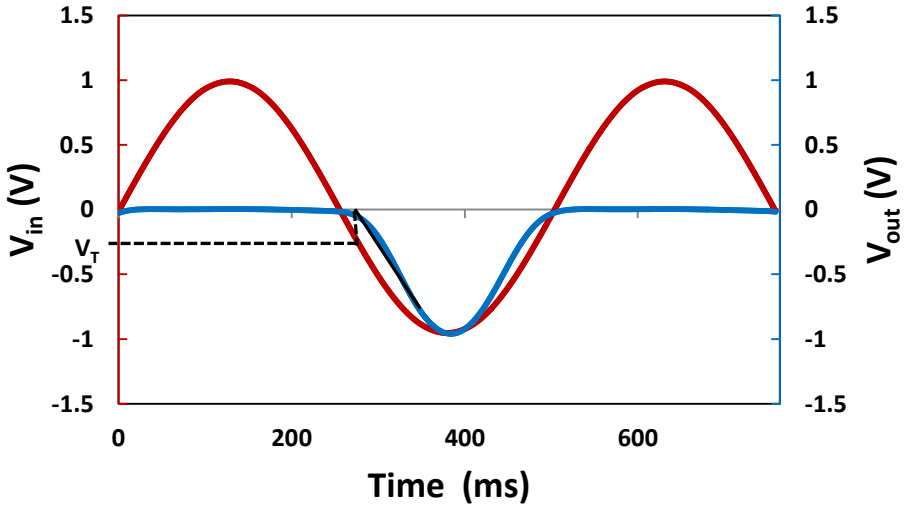

Figure 3-10: Extracting threshold voltage V_T from Saturated transfer characteristics (Blue) parameteric in time and V_S applied to the source (Red)

3.2.2.6 Real time TFT measurements

Section (3.2.2.5) explains the calculation of mobility, threshold, and on/off ratio from parametric saturated transfer characteristics recorded with the circuit shown in Figure 3-6, and results generally agree well with those extracted from source/drain unit measurements. However, this still requires the manual evaluation of measured data after their measurement.

To allow real- time characterization and parameter evaluation, a former member of Sheffield transistor group, Dr Dragoneas, has developed hardware and Labview code suitable for the job [5]. Dr Dragoneas used a 'Picoscope' digital oscilloscope and signal generator to drive a bespoke *I-V* converter circuit board, developed from the simple circuit Figure 3-6, and to communicate the results in digitized form with the help of Microsoft Windows software called: dynamic-link library. The Picoscope is linked to Labview software on a PC via USB and offers a user- friendly interface, where the user can enter TFT details, e.g. the Gate capacitance and width and length of TFT channel and semiconductor's type (n-type versus p-type). Also, the user can select signals' frequency, signals' shape, signals' amplitude and the feedback resistance. Once the aforementioned parameters are identified the software then applies source voltage drive to the TFT, collects resulting drain current data, displays an oscilloscope screen shot similar to Figure 3-7, and extracts TFT parameters such as: threshold, mobility, ratio between on/off ratio together with the on and off currents. This is achieved by an automated version of the methods explained in sections (3.2.2.5.1) and (3.2.2.5.2) respectively.

Figure 3-11 shows an example of the user interface during TFT characterization, the '*I-V* converter assistant'

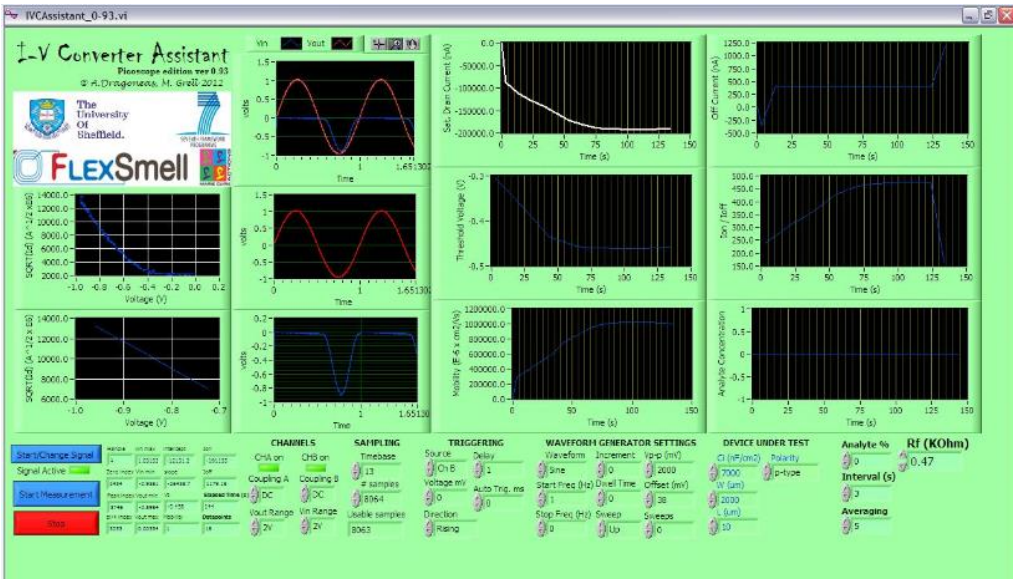

Figure 3-11: User interface during TFT characterization (*I-V* converter assistant)

The *I-V* converter assistant is reported in detail in [5], where it is thoroughly tested on a dry-gated transistor and shown to give reliable independent determination of mobility and threshold in real time. The assistant was adapted here for the characterization of electrolyte-gated transistors, using the appropriate settings (low frequency, low peak source voltage).

The automated extraction of mobility and threshold separately from *I-V* converter data by the assistant is not as reliable for water- gated TFTs as it was for dry- gated devices. This is outweighed though by the convenient collection of real- time maximum drain current data with the 'assistant', which proved sufficient for conclusive amine sensing experiments, to be discussed in Chapter 7.

Chapter 4
Analyte Delivery System

The Sheffield TFT group published several papers on electrolyte gated transistors [38, 55, 65-67] using the 'droplet method' where a drop of electrolyte is placed on the active area of thin film transistor (TFT) as be seen in Figure 1-15 and Figure 4-1. However, to calibrate sensor transistors, it is often desirable to deliver a continuous flow of electrolyte with variable analyte concentration, while characterising the electrical characteristics in real time. In Chapter 3, there is a description of a real time TFT electrical characterisation unit built by a previous group member. Within this thesis, I have developed a pumped flow cell analyte delivery system that combines with the real- time electrical characterisation unit. The design and construction of this system is described in the present chapter.

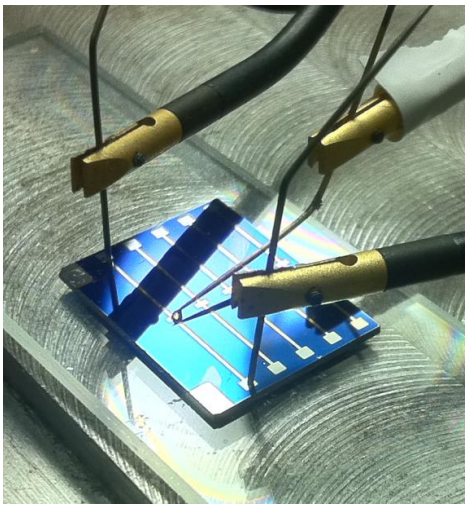

Figure 4-1: Electrolyte gated transistor by using droplet method on the active area of organic thin film transistor.

4.1 Components and Structures

4.1.1 Flow Cell

Flow cell TFTs were formed as a 'sandwich' of two parts, the thin film substrate carrying source/drain contacts and the semiconductor, and the gate substrate carrying a T- shaped gate electrode. The flow cell was formed by sandwiching the two substrates face- to- face, in between Kapton spacer is attached which forms a channel for the flow of water. The thin film substrate is a glass substrate of 15 mm x 20 mm and carries 5 source/drain contact pairs deposited by shadow mask evaporation, as described earlier in section (2.2). Source and drain with a width of 1mm are separated by a channel length of 30 μm, corresponding to a width to

length ratio of 33.33. The gate substrate is made from similar glass slides of 15 mm x 15 mm dimensions with a T- shaped gate strip (Au on Cr adhesion layer), also deposited by shadow mask evaporation. The gate strip was 1.5 mm wide and overlapped the channel area between the Source/Drain contacts on the thin film substrate. The two substrates were sandwiched face-to- face in a slightly staggered configuration. To establish a flow channel (not to be confused with the electrical channel), the two substrates were separated by 240 μm Kapton spacers, establishing a cell volume of 15.6 μL. The two parts were held in place by an acrylic box manufactured in the Sheffield mechanical workshop. The five Source/Drain contact pairs on the thin film substrate were connected to the real time electrical characterisation system (section 3.2.2) by test-pins (plain head & light spring probes, 'pogo sticks') integrated into the acrylic box, making contact with the thin film substrate contact pads. The gate was contacted (i.e., grounded) via a similar probe to the cross bar of the 'T'. Analyte solution was pumped in at one end, and drained into a waste reservoir at the other, as described in the next paragraph. The entire flow cell assembly is illustrated in Figure 4-2 and Figure 4-3.

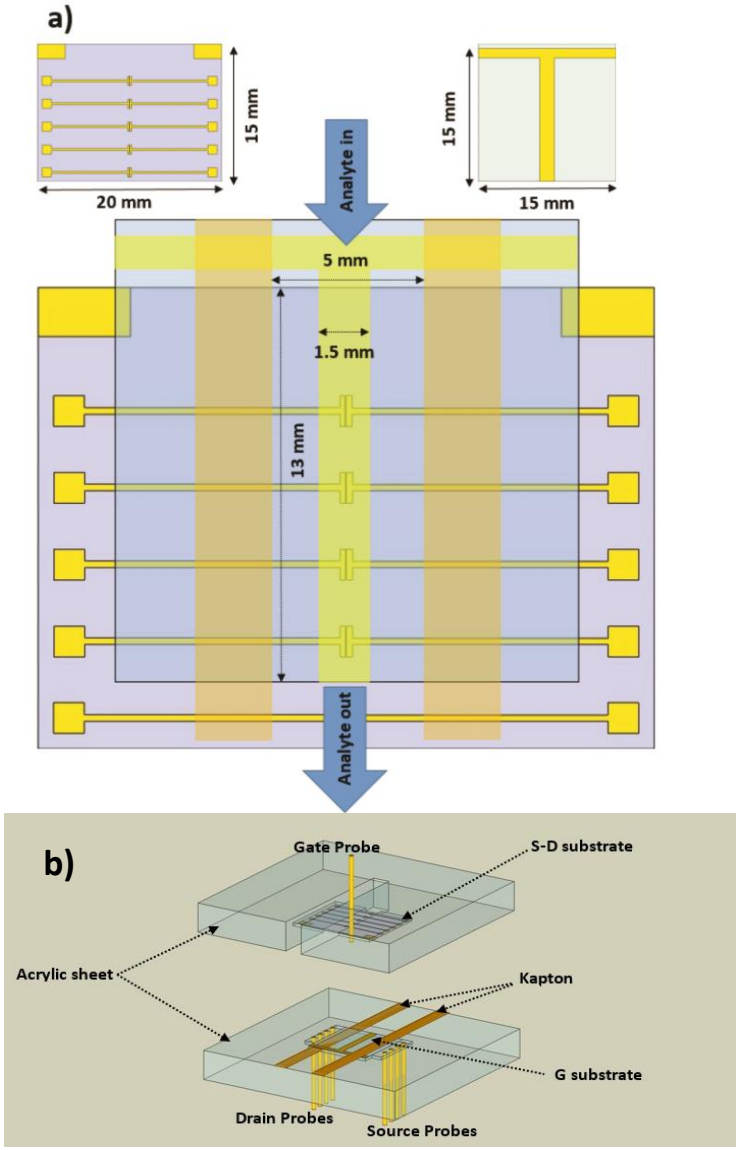

Figure 4-2: (a) Flow cell sandwich consists of five pairs of Au source/drain contacts and Au T-shaped gate contact on square substrate are face to face and formed the channel by using Kapton spacer. (b) Flow cell sandwich assembly constituted by acrylic box and connected to S, D and G by using probes.

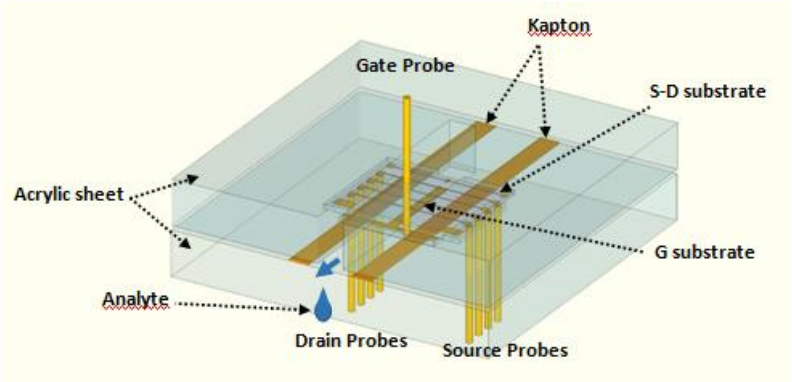

Figure 4-3: The schematic of electrolyte draining through the flow cell.

4.1.2 Analyte Delivery

For analyte delivery, we used two Terumo plastic syringes with inside diameter 29.7 mm and volume of 60 ml. One of the two syringes was filled with pure (analyte - free) electrolyte, e.g. deionised water, or a pH buffer solution. The other was filled with a relatively concentrated solution of analyte in same electrolyte; e.g. in the case of octylamine as analyte (Chapter 7) with a saturated solution. The syringes were mounted in a pair of NE-300 Just Infusion™ syringe pumps from New Era Pump Systems. Syringe pumps were powered from DC batteries to avoid electrical interference from power units connected to AC mains. Pumps were mechanically driving the syringe piston forward at a velocity in the range between ~7 μm/min and ~262 mm/min that could be dialled in from their control panel, thus delivering an adjustable flow in the range 0.5 μL/min to 26.14 mL/min [68]. Both syringes were connected to PEEK GPC tubing (inner diameter exactly 0.51 mm). The two flows were mixed by a Y coupler/mixer that was equipped with valves to avoid back flow. By adjusting the flow rates of the two syringes separately, we could therefore mix any analyte concentration from zero (content of syringe 1) to maximum (content of syringe 2). Finally, the mixture, by the use of a syringe needle (which had diameter exactly 0.23 mm), was fed to the flow channel of the employed sandwich cell. The delivery system is illustrated in Figure 4-4.

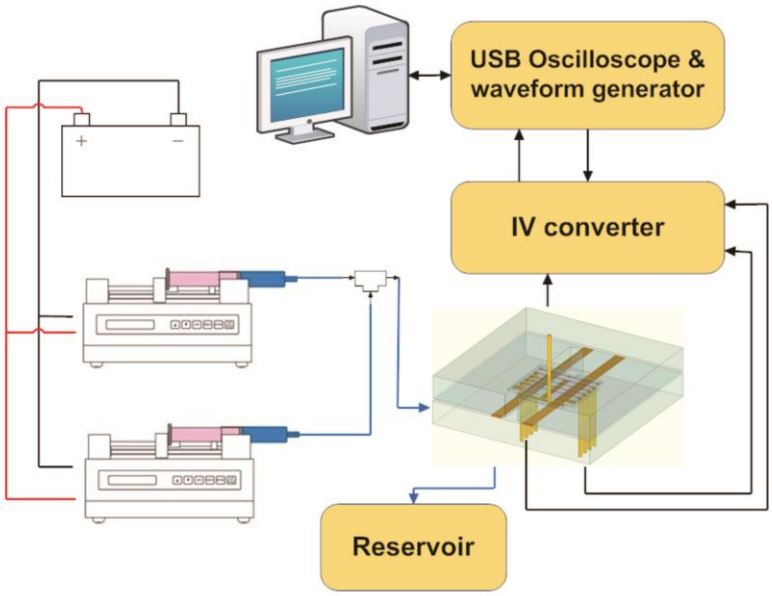

Figure 4-4: Sketch of delivery system for real time sensing.

4.2 Operation and Delivery Response Time Calculation

Figure 4-5 shows a photograph of the complete system in operation.

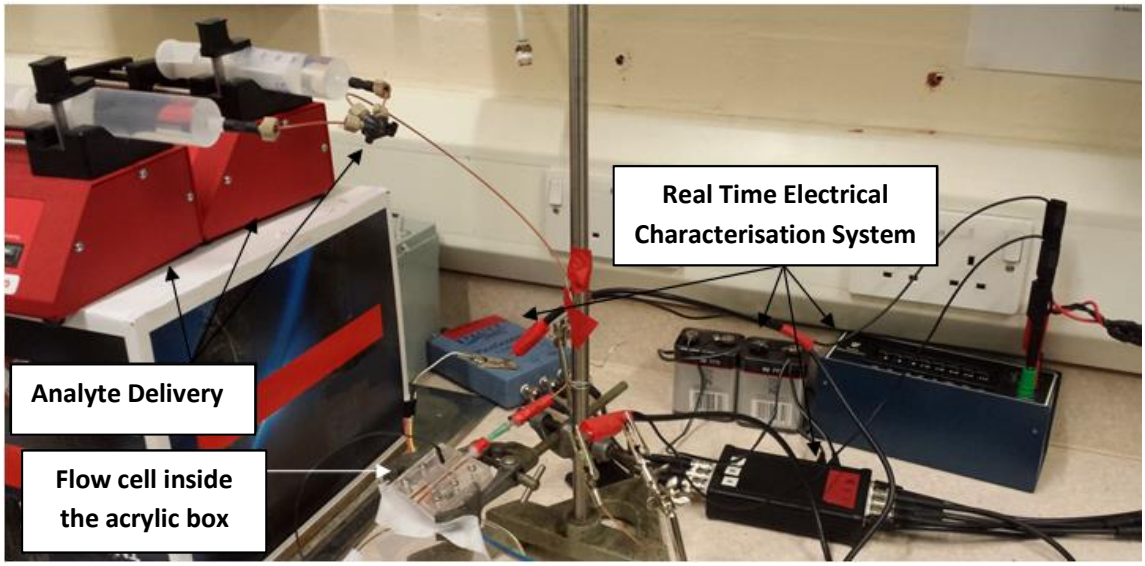

Figure 4-5: Three main units, analyte delivery, flow cell and real time electrical unit in the delivery system.

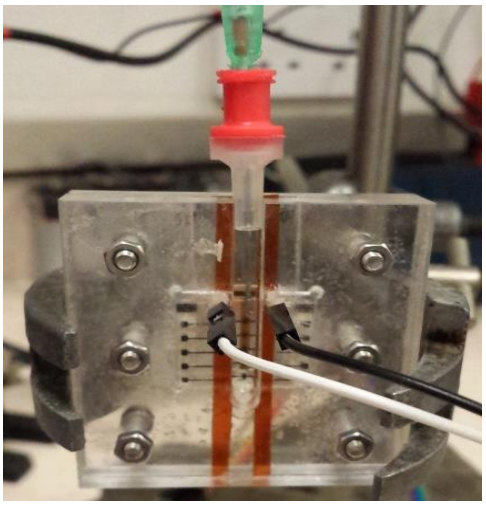

Figure 4-6: Sandwich flow cell assembly which is held together by an acrylic box and S, D and G connected to the real time electrical unit.

The total dead volume of the system was 57 μL derived from, the following equation:

$$V_{total} = V_{flow\ cell} + V_{tubing}. \quad 4\text{-}1$$

In the above, the flow cell dead volume is given by

$$V_{flow\ cell} = whl_{channel}, \quad 4\text{-}2$$

with the length $l_{channel}$, width w and height h of the flow cell channel, and the dead volume of the GPC tubing is given by

$$V_{tubing} = \pi r^2 l_{tubing}, \quad 4\text{-}3$$

where the length and the radius of inner diameter of the GPC tubing are l_{tubing} and r respectively.

In order to keep constant flow rate through flow cell channel, the sum of both the pumps' rates Q was maintained constantly e.g. 250 μL/min regardless of the variable ratio between them even though both pumps' rates ratio is varied to achieve a variable analyte concentration in the extracted mixture. Therefore, the time to turn over the analyte delivery system's total dead volume is ~14 s which is calculated by using the following equation:

$$t = \frac{V_{total}}{Q}. \quad 4\text{-}4$$

We therefore have to expect ~14 s delay in the response of a sensor TFT under test after setting pump flow rates to different values.

4.3 Concentration Calculation

For calibration of sensor transistors, we dissolve a target analyte as solute in the TFT electrolyte, which has to act as solvent for this solute. The amount of solute that is dissolved in a solvent defines the concentration of a solution. We will here speak of 'solutions' regardless whether the solute in its pure form is a solid, or itself a liquid, prior to mixing with solvent. In some cases (e.g. octylamine in water), solubility is limited by a maximum amount of solute that a solvent can accommodate, this is known as 'saturation'. The concentration at which saturation occurs depends on solvent, solute, and temperature.

The unit of concentration we will use in this thesis is 'molarity',M, given as moles of solute per litre of solution. In order to determine the concentration, we must first calculate the number of moles of solute form its mass in grams using the below given equation:

$$number\ of\ moles\ (\mathrm{m}) = \frac{mass\ (\mathrm{gm})}{Molecular\ weight\ (\mathrm{gm/m})}. \quad 4\text{-}5$$

Derived from the above equation (4-5) the following equation can be used to determine molarity,

$$Molarity\ (\mathrm{M}) = \frac{number\ of\ moles\ (\mathrm{m})}{Volume\ of\ solution\ (\mathrm{L})}\ .\qquad 4\text{-}6$$

When one of two syringes is filled with analyte solution e.g. of saturated molarity (M_{sat}) that is pumped at rate Q_{sat}, and the other is filled with plain solvent (i.e., electrolyte) being pumped at rate Q_{solv}, and the two flows are mixed, the resulting diluted molarity of mixed analyte solution (M_{dilute}) is given by equation (4-7):

$$M_{sat}\ Q_{sat} = M_{dilute}\ Q_{solv}\ .\qquad 4\text{-}7$$

We here used an experimental protocol were the total flow rate $Q = Q_{sat} + Q_{solv}$ was kept constant at 250 µL/min. To change M_{dilute}, we changed both Q_{solv} and Q_{sat} simultaneously in opposite directions to keep overall Q constant; the reason for this will be shown in section (4.4). This adds the relation between Q_{solv} = 250 µL/min - Q_{sat} to equation (4-7).

With this added relation we can calculate the flow rate settings required to establish a particular analyte molarity. The following Table 4-1 and Table 4-2 give two examples for this calculation for two analytes that show different saturation in DI water, namely 1-octylamine (Table 4-1, M_{sat} = 1.55 mM), and 1-octanol (Table 4-2, M_{sat} = 3.53 mM). Resulting analyte concentration (*C*) in the mixed solutions is given in 3 units: parts- per- million (ppm), mM (milliMoles/Litre), and percentage of M_{sat}. The molarity, as introduced above, is in the middle of the three concentration columns

C(ppm)	C (mM)	% C_{sat}	Q_{sat} (Octylamine) (μL/min)	Q_{solv} (DI water) (μL/min)
0.5	0.0275	1.79	4	246
1	0.0554	3.57	9	241
2	0.1107	7.14	18	232
5	0.2750	17.86	45	205
10	0.550	35.71	89	161
15	0.8304	53.57	134	116
20	1.1	71.43	177	73
25	1.38	89.29	223	27
28	1.55	100	250	0

Table 4-1: Octylamine concentration from ~28 μM to saturated concentration ~1.55mM.

% C_{sat}	C (mM)	C(ppm)	Q_{sat} (1-Octanol) (μL/min)	Q_{solv} (DI water) (μL/min)
10	0.353	6	25	225
20	0.706	13	50	250
30	1.06	19	75	175
40	1.41	26	100	150
50	1.77	38	125	125
60	2.12	15	150	100
70	2.47	45	175	75
80	2.82	51	200	50
90	3.18	71	225	25
100	3.53	64	250	0

Table 4-2: 1-Octanol concentration from ~353 μM to saturated concentration ~3.53 mM.

We used Table 4-1 and Table 4-2 for testing amine sensitivity of water- gated TFTs in Chapter 7.

4.4 Different Flow rate study

As a test of the delivery system described here, we filled both syringes with deionised water, installed a TFT substrate using organic semiconductor PBTTT (see section (4.1.1)) in the described sandwich flow cell, and used the real- time characterisation system to record the TFT's peak saturated drain current (at source drive voltage peak 1 V) called "on- current" (I_{on}) over time. As a parameter, we changed the volumetric flow rate (Q) between 0 and 2000 µL/min. Results are shown in Figure 4-7.

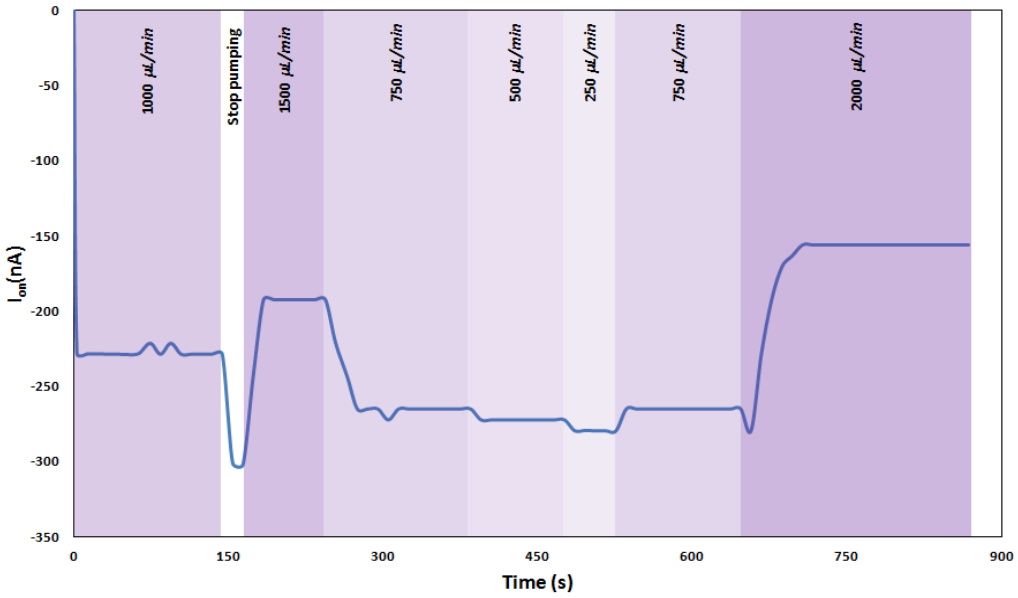

Figure 4-7: Illustrating drain current I_D of water gated PBTTT TFT has been affected by inversely relation with the volumetric flow rate *Q*.

Results clearly show water- gated TFT action, however, I_{on} does depend on Q, even when no analyte is present, decreasing at higher flow rate.

We speculate that a high flow rate might disturb the electric double layer (EDL) at the interface between DI water and PBTTT, and as a consequence reduce the EDL capacitance and therefore drain current, based on equation (1-11).

Regardless of the precise reason, Figure 4-7 shows that a change in flow rate will lead to a change in drain current, which will interfere with any drain current changes that may result from a change in analyte concentration when calibrating a TFT sensor. It is therefore paramount that overall flow rate is kept constant in a sensor test run, to avoid such interference. This is realised by always changing pump rates of both syringes at the same time, in opposite directions, as described above.

Chapter 5
Ionic liquid- gated organic thin film transistors

5.1 Introduction

The utilization of soluble semiconducting polymers is mainly attractive due to their processing options. To better avail the processing advantages, all components in the device and not only the semiconductor should then be solution processed. A constraint is noted however that OTFTs generally have lower charge carrying mobility than other conventional transistors. This matter hampers applications where electrolyte gated-OTFTs supplies drain current I_D. The objective of this study has been to maximize the drain current delivery of solution processed OTFTs. Equation (1-17) provides a guideline towards obtaining high drain current OTFTs at moderate operating drain and gate voltages. To maximize the drain current for a given gate voltage, high capacitance gate media with low threshold and high mobility semiconductors are required. Some of the variables in equation (1-17) however are related to each other, for example higher C_i reduces V_{th}.

The following equation explaining how the specific capacitance of the gate medium C_i affects on threshold voltage V_{th} inversely [69],

$$V_{th} = \frac{Q_0}{C_i} + V_{FB} \ , \qquad 5\text{-}1$$

wherein V_{th} is threshold voltage, Q_0 is bulk charge, and V_{FB} is 'flat band voltage'. Flat band voltage is given by the work functions of source and gate metals, and semiconductor HOMO/LUMO, and is typically in the order of 1V. Q_0 are charges due to (unintentional) dopants in the semiconductor bulk. Equation (5-1) clearly shows how V_{th}comes down as C_i goes up.

This suggests the use of high capacitance gate media, however, such media are typically polar and may lead to substantially reduced carrier mobility at the insulator/semiconductor interface [70]. It is also noted that different gate media have differing or limited stability to applied voltage levels (dielectric breakdown for insulating gate media, electrochemical window for electrolytes). Therefore there is a maximum gate voltage $V_{G\,(max)}$ that cannot be exceeded for a given transistor architecture without destroying the device, thus also limiting saturated drain current $I_{d,sat}$ via equation (1-17). In addition to these performance- limiting and partly competing factors, the geometric ratio *W/L* is a somewhat arbitrary choice. Therefore, two quantities independent of W/L are defined as figures- of- merit to measure the ability of an

OTFT to deliver current, namely the maximum sheet current $I_{\square}$, and the lowest sheet resistance $R_{\square}$. The equations (5-2) and (5-3) define these relationships:

$$I_{\square} = \frac{L}{W} I_{D,sat}\left(V_G = V_G(max)\right), \quad 5\text{-}2$$

$$R_{\square} = \frac{V_G(max)}{I_{\square}}. \quad 5\text{-}3$$

In recent years, OTFTs using electrolytes rather than insulators as gate media have been shown, including solid electrolytes [2, 40] water [26, 71] and ionic liquids (ILs) [1, 39, 72]. When voltage is applied to a gate medium, an extremely thin electric double layer (EDL) forms at the electrolyte / semiconductor interface, with specific capacitance being high (> 1000 nF/cm^2) as is explained in section (1.3.5.1). EDL gating can therefore lead to low V_{th} and high $I_{\square}$ / low $R_{\square}$. Ionic liquids (ILs) as gate media display a number of advantages over aqueous electrolytes: ILs are not volatile [73] and IL/polymer formulations processed via ink jet printing can gel into a quasi-solid film [74]. However, ILs often are good solvents [73] and therefore are not generally suited for use with soluble OSCs. Previous studies and reports have therefore utilized IL-gated OTFTs with vacuum evaporated OSCs [1, 39, 72].

In this chapter I report an OTFT utilizing a solution-processed polymer OSC in combination with an IL gate medium. PBTTT (or poly(2,5-bis(3-hexadecylthiophen-2-yl)thieno[3,2-b]thiophene)) was used as the OSC polymer (Figure 1-17) which is known for high carrier mobility ~ 3.5 cm^{2}V^{-1}s^{-1} [2, 3]. Also, PBTTT is noted for its low and selective solubility due to its predominantly inflexible nature; note its more rigid backbone architecture compared to the chemically related, but more flexible poly(3- hexyl thiophene), P3HT. To dissolve and process PBTTT, we require hot chlorinated benzenes [3]. I show that PBTTT has low solubility to the ionic liquid (1-ethyl-3-methylimidazolium-bis(trifluoromethyl-sulfonyl)imide ('EMITSFI') Figure 1-14 which has been used as a gate medium for evaporated OSCs in previous studies [1, 39, 72]. The resulting EMITSFI- gated OTFTs show good figures-of-merit, specifically $I_{\square}$ and $R_{\square}$.

5.2 Preparation and characterisation of high- current ionic liquid gated organic transistors

IL- gated PBTTT OTFTs were prepared using either, prefabricated gold source/drain (S/D) contact substrates of W = 2 mm/ L = 10 µm (W/L = 200) as described in a previous publication of our group [71], or inkjet printed silver (Ag) contacts of W = 3 mm/ L = 40 µm (W/L = 75). These were printed from a 20 wt% suspension of silver nanoparticles (size ranged 20 – 50 nm)

in ethanol and ethylene glycol (from Sun Chemical, Slough, GB). Ink viscosity and surface tension were 12 mPas and 27 – 31 mN/m at room temperature, respectively. A JetLab 4xl printing system (Microfab, Inc., Plano, TX), was used which was equipped with a 60 μm diameter drop-on-demand piezoelectric printhead (MJ-AT-01-60, Microfab, Inc.). The printing frequency is 100 Hz with a voltage at 60 V and a pulse width to 10 μs. This is in line with the previously reported procedure as in [75, 76].

Printing was performed at room temperature onto glass substrates pre-cleaned with acetone and isopropanol. The printed contact substrates were allowed to dry at room temperature for 10 minutes. They were then placed on a hotplate at 200 ^{o}C for 60 min to remove the carrier solvent and organic components and sinter the silver nanoparticles. (Figure 5-2(b)) inset provides the image of the printed S/D substrates). The resistance between the pad for external contacting, and the 'source' contact to the OTFT channel, was noted at as ~40 Ω. 7 mg/ml PBTTT sourced from Ossila Ltd was dissolved by stirring into hot 1,2dichlorobenzene (DCB) (110 ^{o}C) for 45 minutes. It was then further spun at 5000 rpm for a period of 40 seconds onto contact substrates from hot (100 ^{o}C) DCB. After casting, the films were dried under dynamic vacuum at 110 ^{o}C for 1hr.

For electrolyte gating we applied EMITSFI IL droplets [1, 26, 72] which was sourced from Aldrich. For comparison, we also used DI water applied through a microlitre syringe over the channel area, and insertion of an Au gate needle (American Probe and Technologies) bent into L-shape.

For electrical characterisation, a setup consisting of two Keithley 4200 source/measure units [77] (for output characteristics) was used as be explained in section (3.2.1). A similar setup of a bespoke current/voltage *I-V* converter as described previously in section (3.2.2) can likewise be utilized for recording saturated transfer characteristics parametric in time.

All readings were recorded under ambient atmosphere and the method was introduced in more detail in this thesis section (3.2) as it is used repeatedly.

5.3 Ionic liquid gated organic transistor performance

Figure 5-1 indicates a) the output, b) saturated transfer characteristics and c) extracted saturated transfer characteristics after eliminating the time parameter, for an IL- gated PBTTT OTFT using Au contact substrates. The transfer characteristic is illustrated the parametric in time rather than explicitly as described in section (3.2.2.5.1). The reasons for the acquisition

and the evaluation of parametric transfer characteristics were discussed in the previous studies [4, 55, 71, 78]. The PBTTT OTFT output characteristics display near- ideal shape, with little hysteresis and linear I_D (V_D) behaviour for low V_D, confirming good hole injection at the Au/PBTTT source contact ('Ohmic contacts'). At large negative V_D, I_D saturates, as expected from equation (1-17).

At $V_G = V_D$ = -1 V, a drain current of $|I_D|$ = 1.52 mA was noted which as equations (5-2) and (5-3) provide the $I_{\square}$ to be at 7.6 µA/□ and $R_{\square}$ = 131.6 kΩ/□. This is a remarkably high sheet current / low sheet resistance even in comparison to previous high performance OTFTs, a systematic comparison is in Table 5-1. Like P3HT, PBTTT can also be gated with deionized water an example is included in Figure 5-1(b). This shows resultant drain currents being lower than for IL gating, which reflects the higher specific capacitance of an IL, compared to water. However, performance of PBTTT under water- gating still is considerably better than for water-gated P3HT [4, 26], which is a tribute to the molecular engineering of PBTTT for high carrier mobility.

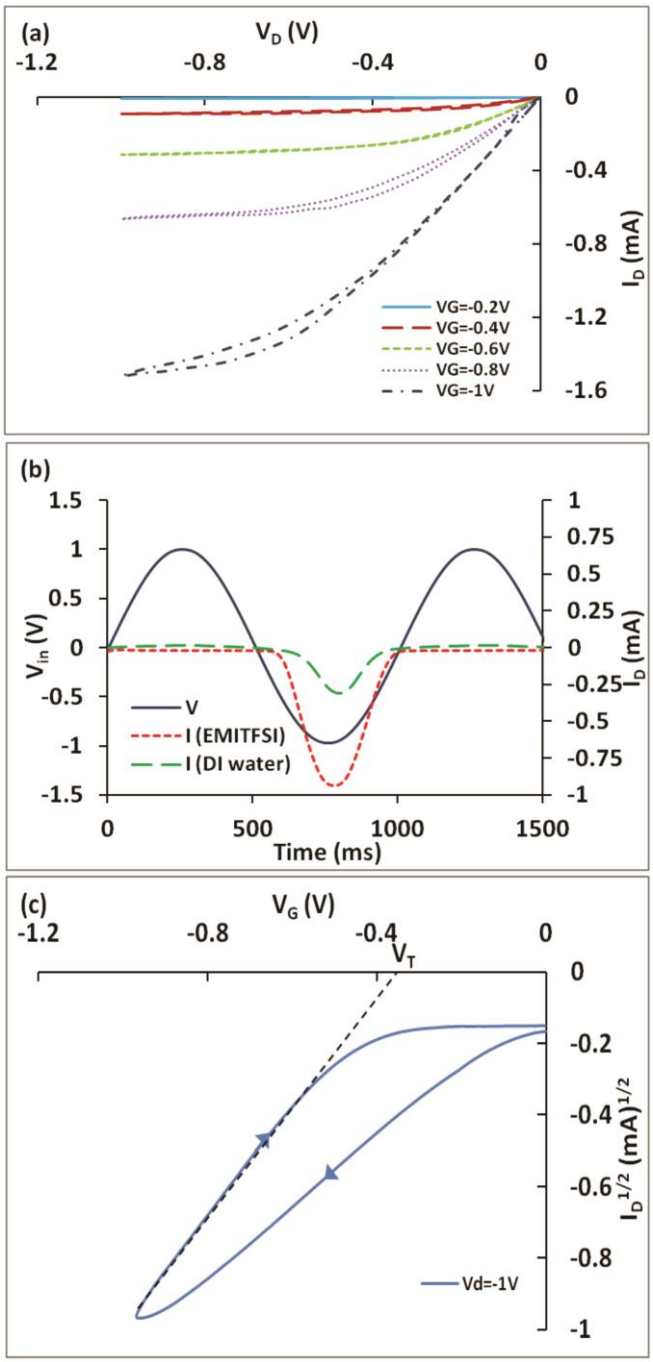

Figure 5-1: (a) Output characteristics for IL- gated PBTTT OTFT with Au source/drain contacts. (b) Saturated transfer characteristics (red short dash), parametric in time, for same device. Also shown is the saturated transfer characteristic for same device when gated with water (green long dash). The drive voltage, applied to the source, is shown in solid blue [4]. (c) V_{th}= -0.36 V has been extracted from saturated transfer characteristics after eliminating the time parameter.

In a control experiment with IL on a blank contact substrate without OSC, we recorded only 0.45 μA maximum current. This provides a safe conclusion that the observed characteristics

exclude parasitic currents in the IL. From the saturated transfer characteristics in Figure 5-1(b), charge carrier mobility in the saturated regime μ_{sat}, and threshold voltage V_{th}, can be evaluated. This is done by eliminating time and then plotting in the form $I_D^{1/2}$ vs. V_G as shown in Figure 5-1(c) and described in section (3.2.2.5.1). The straight line fit provides the threshold from the intercept with the V_G – axis, and μ_{sat} from the slope, cf. equation (1-17). The V_{th} = -0.36 V is noted for IL gating. For the $\sqrt{I_D}$ vs. V_G plot, we find a slope of 0.0476 $\pm$ 0.0001 $A^{1/2}/V$, which according to equation (1-17) corresponds to $\sqrt{\mu C_i \frac{W}{2L}}$. With $\frac{W}{2L} = 100$, this gives $\mu C_i = (2.27 \pm 0.01)$ x 10^{-5} A/V^2. Evaluation of μ_{sat} relies in an estimate for C_i , we here take $C_i = 7000 \pm 700$ nF/cm^2, C_i is given by Ono *et al.* [1] for the IL EMITFSI at low frequency levels of 1 Hz. This leads to μ_{sat} is 3.24 $\pm$ 0.3 cm^2/Vs, which is considered to be a remarkable carrier mobility factor for a polymer OSC. PBTTT is known for its exceptional mobility, e.g. Hamadani *et al.* report that dielectric- gated PBTTT OTFTs show a mobility of ~1 cm^2/Vs [3]. Also a very high charge carrier density in the accumulation layer can be obtained through a gating with a high capacitance IL, which may lead to a rise in mobility [12].

When saturated transfers on IL- gated PBTTT are measured with drive voltages exceeding 1.2 V, a decline in on/off ratio (on/off ~2200 under 1 V drive) is noted. This shows a rapid decay in overall device performance. I state that this may be related to water being electrolyzed. The highly hygroscopic IL will rapidly absorb water from atmospheric humidity, and while the 'electrochemical window' of the EMITSFI IL used was 4.3 V [73], the 'window' for water is only 1.23 V. Therefore for the purposes of the study, a maximum voltage of 1 V is being limited in the subsequent experiments and observations. I state that by limiting the gate voltage to 1 V a serious drawback is not noted. Limiting drive voltages to 1 V is supported by a study of Xie and Frisbie who report that the mobility at gate voltages > 1 V declines again in IL-gated devices at room temperature [72]. They attribute this factor to a binding between holes in the OSC and anions in the IL.

For a better practical form of 'printed electronics' it is required that all components of OTFT be solution processed, including the S/D contacts. Therefore, we also prepared IL- gated PBTTT OTFTs with printed Ag contacts (description is provided in section (5.2) while Figure 5-2 portrays the characteristics).

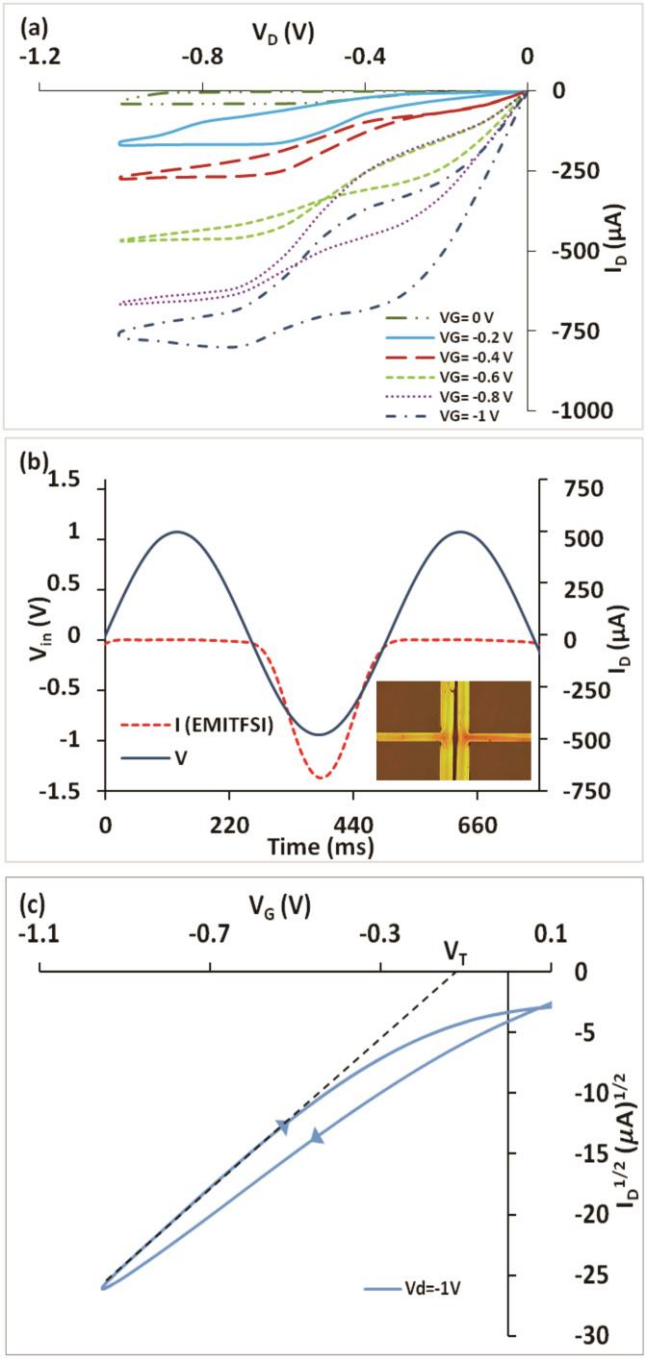

Figure 5-2: (a) Output characteristics for IL- gated PBTTT OTFT with printed Ag source/drain contacts. (b) Saturated transfer characteristics (red short dash), parametric in time for same device, Drive voltage in solid blue. Inset: Optical micrograph of printed / fused Ag contacts with L =40 m. (c) V_{th}= -0.15 V has been extracted from Saturated transfer characteristics after eliminating the time parameter.

The output characteristics in Figure 5-2(a) display considerable hysteresis. For low gate voltages, non-linear output is noted for I_D (V_D) at low drain voltage. I_D continues to be

sublinear initially and curves upwards only at higher V_D. This shape, especially the sub-linear part, is the mark of a considerable hole injection barrier at the printed Ag / PBTTT contact. This is attributed to the lower work function of Ag compared to Au. The high conductivity of the IL- gated channel highlights the poor contacts, which contributes to greatly non-ideal output characteristics. The positive side is that at high gate voltages, the injection problem at the contact is resolved; we attribute this to the fact that the high gate voltage strongly assists tunnelling injection. Therefore, high drain currents are delivered at $V_G = V_D = -1$ V for IL-gated PBTTT with printed Ag contacts.

In fact, higher sheet currents and low sheet resistance is noted for the above OTFTs with printed Ag contacts when compared with OTFTs with Au S/D contacts, despite the injection barrier at the Ag contact ($I_{\square} = 9.7$ μA/□ (Ag) vs. $I_{\square} = 7.6$ μA/□ (Au); ($R_{\square} = 102$ kΩ/□ vs. $R_{\square} = 131.6$ kΩ/□). It is known that the apparent carrier mobility and it the sheet current increase for longer channel length L. This is because longer channels weaken the relative contribution of contact resistance, and ink jet printed Ag contacts are separated by a longer channel than prefabricated Au contacts [79]. Some doubt is therefore cast on the sheet current / sheet resistance metric in general due to the dependence of apparent mobility on L. However, we note that this is generally used for characterising conductive surfaces, e.g. synthetic metal films.

5.4 Summary and conclusions

We have reported the first IL gating of a solution processed semiconducting polymer, PBTTT. The performance of resulting OTFTs is very good in the sense of high sheet current / low sheet resistance. This is underscored by comparison to a few high-performance OTFTs from recent other studies in the literature, which is shown in Table 5-1.

Reference	Semiconductor	Deposition	h^+ / e^-	Gate medium	$I_{\square}$ [μA/□]	$R_{\square}$ [MΩ/□]
Hasegawa *et al* [80]	C_8-BTBT	Ink jet (2 shot)	h^+	Dielectric	69	0.87
Klauk *et al* [81]	DNTT	Evaporation	h^+	Dielectric	0.54	5.56
Bao *et al* [23]	Pentacene	Evaporation	h^+	Dielectric	0.3	6.7
Horowitz *et al* [26]	P3HT	Spin casting	h^+	Water	0.0054	111
Grell *et al* [71]	ACN- conditioned BBL nanobelts	Drop casting	e^-	Water	0.35	2.28
Berggren *et al* [82]	P3HT	Spin casting	h^+	Solid electrolyte	0.0175	57
Frisbie *et al* [72] Takeya *et al* [1]	Rubrene	Evaporation	h^+	Ionic liquid	0.66	0.3
Takeya *et al* [39]	C_{60}	Evaporation	e^-	Ionic Liquid	0.027	37
Heeney *et al* [3]	PBTTT	Spin casting	h^+	Dielectric	25	2.4
Torsi *et al* [2]	PBTTT	Spin casting	h^+	Solid electrolyte	0.459	2.18
This work	PBTTT (Au contacts)	Spin casting	h^+	Ionic Liquid	7.6	0.132
This work	PBTTT (inkjet Ag contacts)	Spin casting	h^+	Ionic Liquid	9.7	0.102
This work	PBTTT (Au contacts)	Spin casting	h^+	Water	1.6	0.64

Table 5-1: Figures- of- merit $I_{\square}$ and $R_{\square}$ (equations (5-2) and (5-3)) from recent publications, in comparison to data from this work. The table includes a range of semiconductors (solution processed and evaporated), and gate media (dielectrics, solid electrolytes, liquid electrolytes). $I_{\square}$ and $R_{\square}$ were extracted from transistor characteristics shown in the respective publications.

In summary, the figures- of- merit for entirely solution- processed OTFTs reported in this thesis compare favourably within Table 5-1. This is the result of the concurrent high capacitance, high carrier mobility, and low threshold, of the PBTTT/EMITSFI EDL transistor. Further, IL gating of PBTTT opens up avenues to explore the interesting and unique field of physics of OSCs at extremely high charge carrier concentrations [72] on the example of a semiconducting polymer. Previously studies of these sorts were limited to low molecular weight OSCs. As a concluding remark, we note that presently, the operational lifetime of the devices discussed here were limited to less than or maximum of 1 hr , probably due to eventual slow dissolution of PBTTT in IL. We invite that further improvement in the device can be

made to reduce the limited durability, e.g. by the use of a gelled IL [74] or synthesis of a PBTTT derivative that can be cross-linked after deposition.

Chapter 6

New precursor- route ZnO films for increasing performance of aqueous electrolyte- gated inorganic thin film transistors

6.1 Introduction

As is explained in section (1.3.6) about the features of electrolyte-gated OFET (EGOFET) such as very low threshold and high capacitance EDL (electric double layer), There is interest in developing the thin film transistors (TFTs) into a unique kind of biosensor, in which the active part of the transducer is an aqueous sample under test. TFT devices gated by a biologically realistic aqueous electrolyte, phosphate-buffered saline (PBS) solution, were sensitised (e.g. by enzymes) either at the semiconductor/water interface [33, 34] or at the gate electrode [35]. Sensitised layer at the gate electrode is easier and more versatile as no chemical modification of the organic semiconductor is required, otherwise there would have been a loss of performance. Highly concentrated electrolyte gate media like PBS, when compared to DI water, favourably display higher capacitance somewhat up to higher frequencies. Organic semiconductors, however, often suffer stability problems under concentrated electrolytes. They may become subjected to penetrating ions, i.e. electrochemical transistor behaviour competes with field effect gating as be shown in Figure 1-16(b) [83].

This makes the output of the transducer difficult to interpret and can mostly be avoided when the inorganic semiconducting film is utilized as an alternate. Ong *et al.* [54] had shown that the II-VI semiconductor Zinc oxide (ZnO) can be prepared by casting a soluble precursor, Zinc acetate (ZnAc, $Zn(O_2CCH_3)_2$), as be seen in Figure 6-1 with subsequent thermal conversion into ZnO under atmosphere.

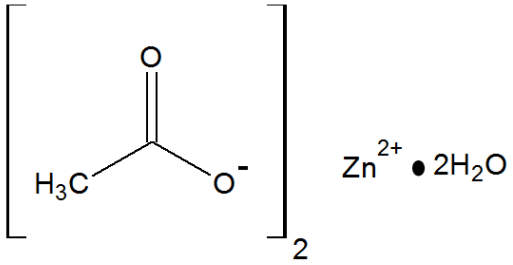

Figure 6-1: Chemical structure of Zinc Acetate Dihydrate

Ong *et al*. reported (dielectric- gated) n- type field effect transistors using such films, with electron mobility $\mu \sim 5$ cm^2/Vs and good on/off ratio. However, high operational voltages are

needed using the conventional 'dry' dielectric gate medium with low capacitance. Another study done by Al Naim *et al*. indicates aqueous media can be utilized for gating precursor route ZnO [55] and also several papers reported that electrolyte- gated precursor- route ZnO transistors may show similar mobility to dry- gated devices at much reduced threshold [53, 84, 85]. This is attributed mainly to high EDL capacitance. To date, however, mobility performance in precursor- route ZnO is still lower than ZnO deposited by methods such as magnetron sputtering or pulsed laser deposition [86-89].

This chapter reports on the preparation of precursor- route ZnO with improved performance in electrolyte-gated TFTs. This performance was compared to previously reported precursor-route ZnO films. We attribute the improvement in performance to the utilization of a mixed solvent for casting the precursor (ZnAc).

6.2 Preparation of aqueous electrolyte gated ZnO TFTs from a mixed casting solvent

Precursor solutions were made by dissolving 0.1M ZnAc in ethanol (EtOH), isopropanol, acetone, or 1:1 EtOH/acetone. These were stirred consecutively at temperature 80 ^{O}C for ~2 hours and it is observed that ZnAc dissolves more readily in the mixed solvent. Preparation of the TFT contact substrates was done as is described in sections (2.1) and (2.2). For converting the ZnAc solution into ZnO, the solution was cast onto contact substrates at 2000rpm for 50s and thermally converted under atmosphere on a hotplate at 450 ^{o}C for 12 minutes. The ZnAc coating and conversion was done three times. The resultant ZnO films were characterised by XPS and SEM.

Calibration of the XPS is done by the graphitic carbon C 1s peak [90] by absorbing graphitic carbon on the surface during exposure of the sample to ambient atmosphere. This is a commonly used method for XPS calibration [91]. ZnO surfaces were imaged by SEM at 15 kV.

For transistor manufacture, a droplet of the aqueous electrolyte 0.01 M phosphate buffered saline (pH = 7.4) (PBS, Aldrich catalogue No P4417) was applied as a gate medium. This was then electrically addressed by an L- shaped Au gate needle that was, using a probe head, lowered to very close proximity (200 μm adjusted by a glass cover slip used as spacer). The 'foot' of the L was positioned with the width *W* of the transistor channel which overlapped the channel completely. Source and drain (S/D) were contacted by Tungsten (W) needles. These had readily pierced through the ZnO film formed on the evaporated Au contacts.

The TFT output and transfer characteristics were then quantified with two Keithley source/measure units configured for TFT characterization, a detail in section (3.2.1).

6.3 Morphological and Electrical Characterisation of ZnO thin film transistors from a mixed casting solvent

Previous reports [55, 84] had utilized ethanol (EtOH) as the casting solvent on water- gated ZnO transistors from ZnAc precursor. However, we find that ZnAc at a typical precursor solution concentration of 0.1 M in EtOH does not dissolve readily. We required heating and stirring for several hours to achieve complete dissolution. On storage at ambient temperature, ZnAc then precipitates again in less than an hour. For re-dissolving the process of heating was repeated along with stirring for 30 minutes before processing. Solubility of ZnAc in pure acetone and 2-propanol was found to be similarly poor. Ong *et al.* [54] has utilized methoxyethanol to dissolve ZnAc but did not clearly report on solvent quality.

We find that, a 1:1 mix of EtOH and acetone was a better solvent for ZnAc then either EtOH, 2-propanol, or acetone, alone heating and stirring. ZnAc in mixed solvent was dissolved quicker (∼2 hours) compared to (∼5 hours) for sole solvent as mentioned before. Also, the advantage noted is that only a small amount of precipitate was formed even after several days of storage. These precipitates quickly re- dissolved on gentle heating.

I here compare ZnO films prepared from ZnAc dissolved in mixed EtOH:Acetone (1:1) solvent, and similar films from pure EtOH.

6.3.1 XPS results

The first process is to characterize both resulting ZnO film surfaces by X-ray photoelectron spectroscopy (XPS). Figure 6-2 shows the detected peaks for Zn 2p orbitals for precursor-route ZnO films cast from EtOH (top) and mixed solvent (bottom). Figure 6-3 shows O 1s XPS spectra for precursor- route ZnO films cast from EtOH (top) and mixed solvent (bottom). For Zn 2p orbitals, the usual split into Zn $2p_{1/2}$ Zn $2p_{3/2}$ orbitals [92-96] was observed, more details in section (3.1.4). The (non- Gaussian) O 1s peaks in Figure 6-3 have been resolved into a superposition of two overlapping Gaussians. The lower energy Gaussian has been attributed to O_2^- ions bound into the regular wurtzite structure of ZnO (Zn-O-Zn), the higher energy Gaussian to oxygen in metal-OH (M-OH) surface groups as be described in section (1.3.7.2) [92]. All XPS peak positions, and their widths (FWHM), are summarised in Table 6-1.

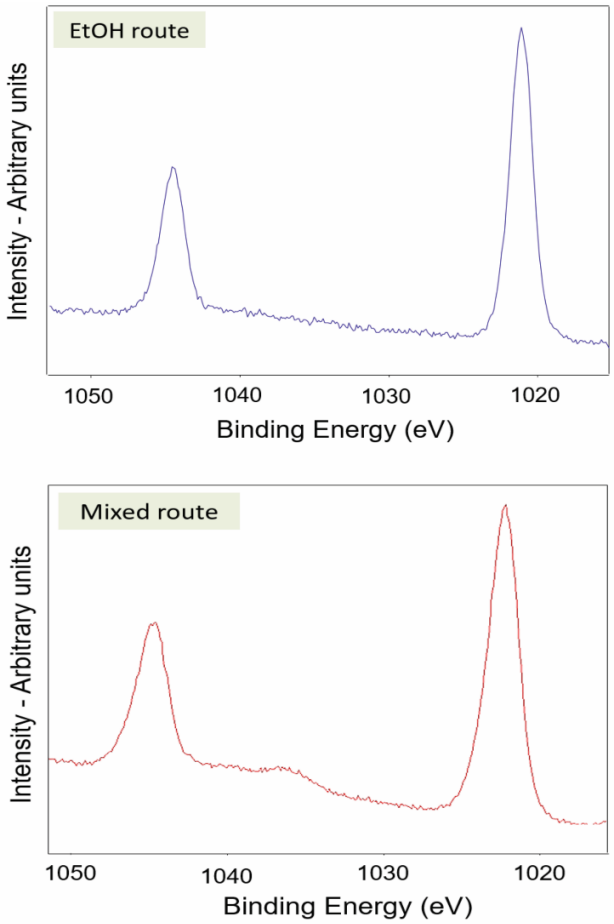

Figure 6-2: Zn 2p orbitals XPS spectra for ZnO films Top: spin casting ZnAc dissolved in pure EtOH, bottom: spin casting ZnAc dissolved in mixed solvent, EtOH:Acetone 1:1.

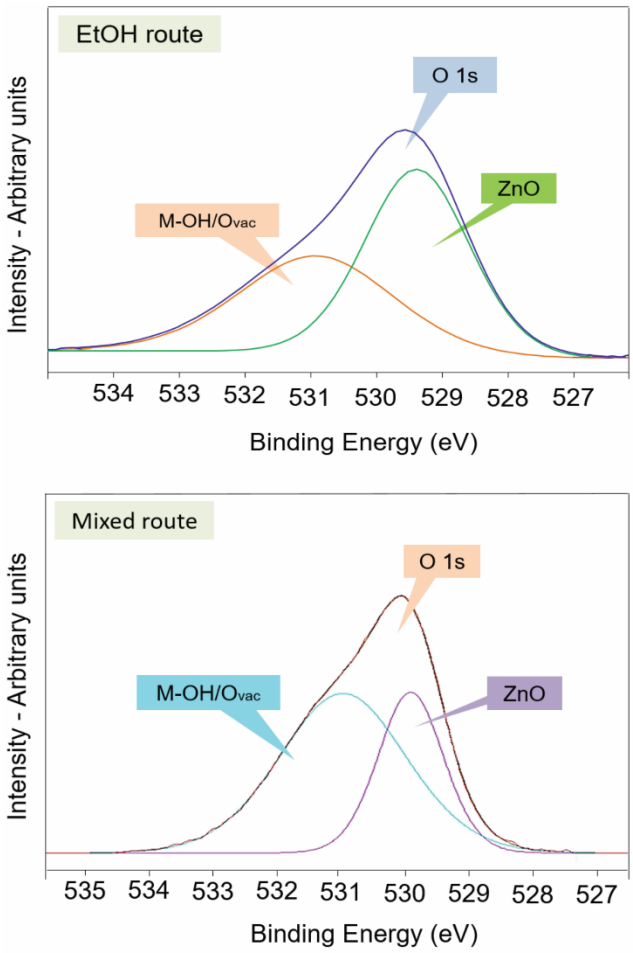

Figure 6-3: O 1s XPS spectra for ZnO, Top: spin casting ZnAc dissolved in pure EtOH, bottom: spin casting ZnAc dissolved in mixed solvent, EtOH:Acetone 1:1.

	EtOH route		**Mixed route**	
	Position (eV)	**FWHM (eV)**	**Position (eV)**	**FWHM (eV)**
Zn $p_{1/2}$	1021 ± 0.17	1.75 ± 0.03	1023 ± 0.23	2.5 ± 0.042
Zn $p_{3/2}$	1045 ± 0.12	2.0 ± 0.019	1047 ± 0.2	2.5 ± 0.025
O 1s	529.6 ± 0.44	2.8 ± 0.051	530 ± 0.39	2.2 ± 0.047
Zn-O	529.4 ± 0.31	1.9 ± 0.02	529.9 ± 0.5	1.07 ± 0.02
M-OH	531.2 ± 0.22	2.8 ± 0.04	531 ± 0.42	2.2 ± 0.018

Table 6-1: Offers observed XPS peak positions summary, with their FWHM, for ZnO films which is extracted from ZnAc precursor for both routes.

All observed XPS peaks were found to be in the same range as in previous XPS studies on ZnO [84, 92-96]. Overall, XPS analysis shows the chemical identity of the films as wurtzite ZnO along with Zn-OH surface groups. This process confirms the conversion of the precursor for

both casting solvents successfully. However, no differences at the atomic binding level were noted between the different casting solvents.

6.3.2 SEM results

The SEM surface imaging shows differences at the morphological level on the ~10 nm size scale between ZnO films cast from precursor in different solvents. In Figure 6-4, images of ZnO surfaces are portrayed. The top image is result from the conversion of EtOH cast precursor. The bottom indicates mixed solvent cast precursor.

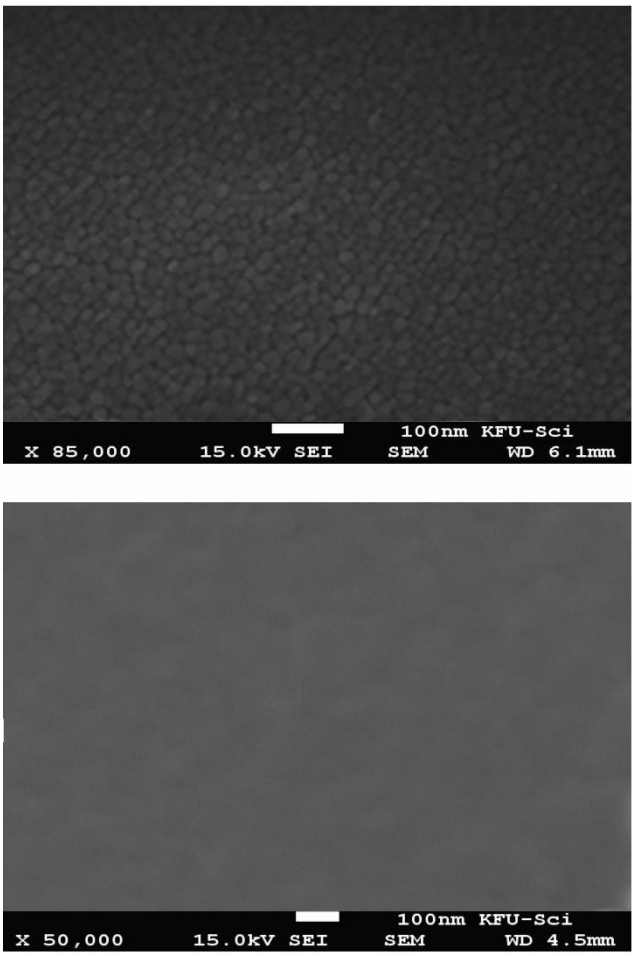

Figure 6-4: SEM images of ZnO films after thermal conversion of ZnAc precursor. Top: spin casting ZnAc dissolved in pure EtOH, bottom: spin casting ZnAc dissolved in mixed solvent, EtOH:Acetone 1:1.

Films show recognisable small grains in the order 7 to 15 nm from EtOH- cast precursor. In contrast, the image of mixed solvent cast precursor films shows little contrast. The grains are barely recognisable, and larger (17-20 nm). The absence of the clear and visible morphological features indicates a very homogenous film in case of the mixed solvent cast ZnO surface.

I conclude that the precursor ZnAc forms a true solution in a better quality mixed solvent. In a poor solvent, e.g. pure EtOH, precursor molecules will cluster into small aggregates and do not fully dissolve. When casting from the poor solution, it is observed that aggregates will transfer to the substrate. On thermal conversion this primes the formation of ZnO grains with defined boundaries. When the precursor is cast with a better solvent the grains are larger, and less clearly separated.

Grain boundaries usually limit charge carrier mobility. The homogeneous, featureless morphology of the mixed solvent cast ZnO highlights that the performance of this as a semiconductor is hopefully better when used as a thin film transistor (TFT).

6.3.3 Output & transfer characteristics results

Both types of the ZnO films were tested in TFTs gated by phosphate- buffered saline (PBS) as an aqueous gate medium. PBS is considered to be a realistic medium for biosensor applications and is often used to simulate bodily fluids [33-35]. Since the surface of ZnO is hydrophilic, PBS forms a flat 'puddle' with small contact angle. Figure 6-5 and Figure 6-6 indicate the resultant transistor output- and transfer characteristics.

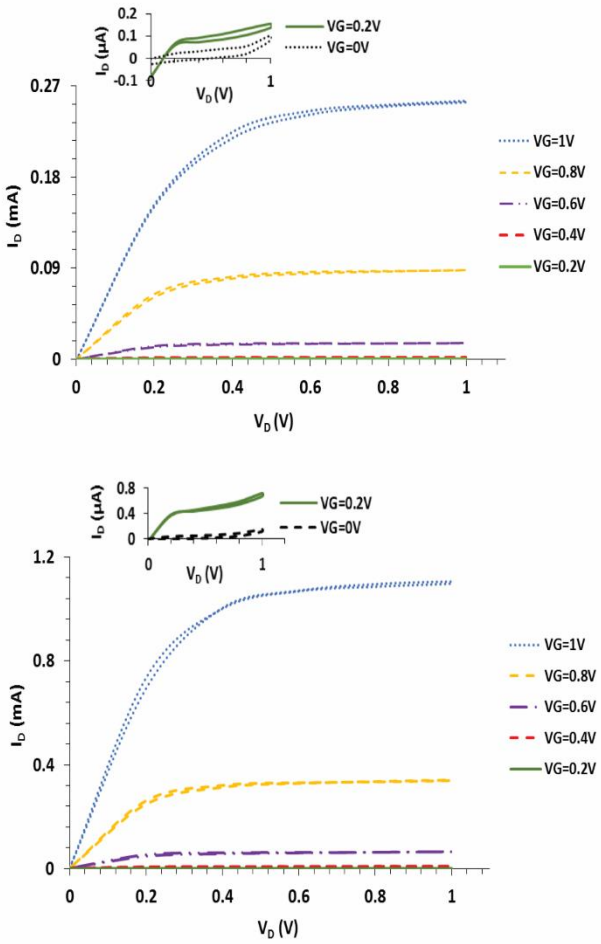

Figure 6-5: Output characteristics of PBS electrolyte gated ZnO TFTs resulting from Zn acetate precursor route. Top: spin casting ZnAc dissolved in pure EtOH. Bottom: spin casting ZnAc dissolved in mixed solvent, EtOH:Acetone 1:1. Insets show magnified output characteristics at low V_G.

Output characteristics show that TFTs turn on for positive gate voltages, as expected for electron- transporting transistors. Electron-, rather than hole, type transistor action is well established for ZnO [52, 55, 84, 86] but is in contrast to organic TFTs gated with aqueous electrolytes which to date all were hole transporters. Again little hysteresis, a truly linear 'linear' regime and drain current saturation at high drain voltages are noted that to output characteristics being near ideal. The inset of Figure 6-5 shows magnified low gate voltage output characteristics. This clearly highlights TFTs are 'off' at V_G = 0 V, and 'on' at V_G = +0.2 V (above threshold). The range of the threshold voltage is therefore between 0 and 0.2 V, and is similar to previous reports on PBS-gated ZnO [84]. Due to the high specific capacitance of electrolyte gate media, low threshold is noted for all electrolyte- gated TFTs. In parallel, gate leakage currents were also monitored; compared to drain current the gate leakage was always small (< 5 μA at V_D =

V_G =1 V for EtOH route, 0.2 µA for mixed solvent route). Output characteristics for mixed solvent route gives higher I_D (about 4 times higher max current) that could be as a result of higher mobility.

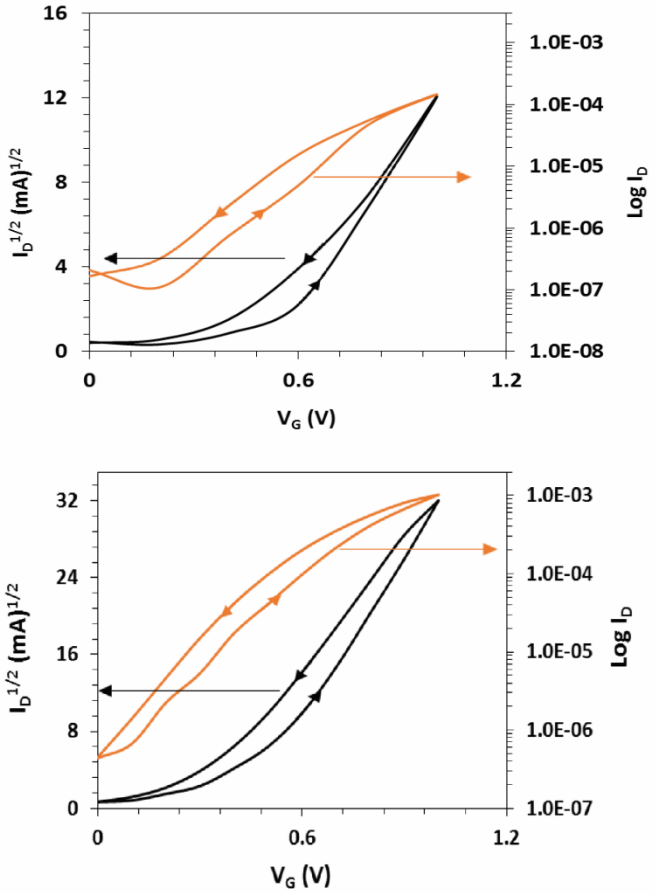

Figure 6-6: Saturated transfer characteristics of PBS electrolyte gated ZnO TFTs resulting from Zn acetate precursor route. Top: spin casting ZnAc dissolved in pure EtOH. Bottom: spin casting ZnAc dissolved in mixed solvent, EtOH:Acetone 1:1. Two different representations of transfer characteristics are illustrating (on $I_D^{1/2}$ (black) and logI_D (orange) scale).

Figure 6-6, indicates saturated transfer characteristics for same transistors. Both show some hysteresis, which is also sometimes observed for ZnO TFTs under ionic liquid (IL) gate media [85]. Figure 6-6, top in particular also shows a rather curved $I_{D,sat}^{1/2}$vs. V_G plots. This is approaching linearity (as predicted by generic TFT theory) only at high gate voltages (above 0.8 V). At high gate voltages/carrier densities in the channel, non- linearity of the saturated transfer characteristic in $I_D^{1/2}$ representation may indicate increasing electrolyte capacitance or increasing carrier mobility. The low gate voltage output characteristics is considered to be a better estimation of the threshold voltage. However, field effect transistor action is clearly

shown by transfer characteristics, i.e. off → on switching of drain current with gate voltage. The on/off ratios [I_D (V_G = 1 V) / I_D (V_G = 0 V)] is 710 for EtOH route, while is 2340 for mixed solvent route. This is within the range 10^2… 10^4 reported previously for ZnO TFTs [84, 85] under various electrolyte gate media.

Although the qualitative characteristics are similar between the different casting solvents, there is a remarkable quantitative difference. This is shown as follows:

For the ZnO TFT cast from ZnAc in EtOH, saturated drain current at V_G = V_D = 1 V is 0.26 mA, corresponding to a sheet resistance $R_{\square}$ (1 V) = W/L [V_D = 1 Volt / $I_{D,sat}$ = 0.26 mA] = 128 kΩ/□. For the ZnO TFT cast from ZnAc in mixed solvent the saturated drain current is significantly higher, at 1.1 mA. This corresponds to a sheet resistance of only $R_{\square}$ (1 V) = 30 kΩ/□. The calculation of carrier mobility is difficult when compared to standard transistor equations in the case of electrolyte- gating. This is considered to be due to uncertainty on the precise figure of specific capacitance C_i [26, 55]. Instead a figure- of-merit μC_i can be extracted directly from measured characteristics without making assumptions on C_i [24]. When the saturated transfer characteristics is evaluated at high gate voltage (V_G = 0.8 V … 1 V), the μC_i = 33 μAV^{-2} is observed for EtOH- cast films, and 117 μAV^{-2} for films cast from mixed solvent, which is almost 5 times higher.

If the assumption of a specific capacitance [26] of C_i = 3 μF/cm^2 is made, the electron mobility of 11 cm^{2}V^{-1}s^{-1} for EtOH- cast ZnAc-precursor ZnO, and 39 cm^{2}V^{-1}s^{-1} for mixed- solvent cast ZnAc-precursor ZnO is noted. True mobilities from electrolyte gated transistor should be treated with caution. However, the approximately five- fold improvement remains true, whatever the magnitude of C_i.

Table 6-2 puts the current study into context with literature results on directly comparable devices (more specifically electrolyte- gated TFTs using solution- processed ZnO as semiconductor).

Reference	Preparation	Gate medium	$R_{\square}$ [kΩ/□]	μC_i [μAV^{-2}]
Park *et al.*[53]	Li- doped ZnO cast from ammonia solution	Ionic liquid	110 @ 1V	8.3
Singh *et al.*[84]	ZnAc precursor cast from EtOH	PBS	5000 @ 0.5V	1.4
Singh *et al*.[84]	ZnAc precursor cast from EtOH	DI water	77000 @ 0.5V	0.23
Al Naim *et al*.[97]	ZnAc precursor cast from EtOH	DI water	180 @ 0.8V	26
Thiemann *et al*.[85]	ZnAc precursor sprayed from MetOH	Ionic liquid	50 @ 1V	48
This work	ZnAc precursor cast from EtOH	PBS	128 @1V	33
This work	ZnAc precursor cast from EtOH : Acetone	PBS	30 @1V	117

Table 6-2: Electrolyte- gated TFTs performance characteristics with solution- processed ZnO.

Data in Table 6-2 clearly marks the improved performance of ZnO films derived from mixed solvent route processed ZnAc precursor in electrolyte- gated TFTs when compared to any other solution- processed ZnO films. For mixed solvent cast precursor the sheet resistance is lower with the figure-of-merit being higher even when comparison is made with previous studies where higher capacitance ionic liquid (rather than aqueous gate medium)[85] was used, or when ZnO cast from ammonia solution (rather than precursor- route ZnO) [53] was used.

A further comparison, indicates that mixed solvent route ZnO results are also better when compared to electrolyte-gated organic TFTs, even those using state- of- the art hole transporting polymer, Poly(2,5 bis(3-hexadecylthiophen-2-yl)thieno[3,2-b]thiophene) (PBTTT). This is indicated by the fact that for best performing electrolyte gated PBTTT TFTs [65] the sheet resistance is observed at $R_{\square}$ (1 V)= 640 kΩ/□ for water gating and 102 kΩ/□ for ionic liquid gating. These sheet resistances are still higher than the sheet resistance observed in the current study for mixed solvent cast precursor ZnO.

The TFT performance reported for mixed solvent cast precursor- route ZnO is matched only by conventional 'dry' processed ZnO TFTs. Fortunato *et al.* [86] and Zhang *et al.* [87] deposited ZnO by rf magnetron sputtering and reported carrier mobility of 70 $cm^2V^{-1}s^{-1}$ when gated by silicon oxynitride (SiOxNy) dielectric [86], and 60 $cm^2V^{-1}s^{-1}$ using Ta_2O_5 gate insulator [87]. However in both experiments, mobilities were measured at rather high voltages (Fortunato *et al.*: 10 V; Zhang *et al.*: 5V). Brox-Nilsen *et al.* [88] report 50 $cm^2V^{-1}s^{-1}$ again on Ta_2O_5 at slightly lower voltage (4 V). The highest mobility to date of 110 $cm^2V^{-1}s^{-1}$ for ZnO TFTs has been

observed by the study conducted by Bayraktaroglu *et al.* [89] who grew ZnO by pulsed laser deposition onto a substrate held at 350 °C. The sheet resistance in the device of Bayraktaroglu *et al*. was $R_{\square}$ (15 V)=25 kΩ/□. However, the previous studies as mentioned did not benefit from the ease of processing offered by soluble precursor routes, none of the previous studies (Fortunato *et al*, Zhang *et al*., Brox Nilsen *et al.*, and Bayraktaroglu *et al.*) conducted experiments with gating done with an aqueous electrolyte, which can be considered essential for biosensor applications.

6.4 Conclusions

It has been, through studies and literature, well established that performance of organic semiconductor devices depend on the choice of processing solvent [98]. I here make a similar observations on ZnO semiconductor devices prepared via a solution- processed precursor. We found Zinc acetate (ZnAc), a precursor to the II-VI semiconductor zinc oxide (ZnO), dissolves significantly better in a 1:1 mix of ethanol and acetone than in pure ethanol, acetone, or isopropanol. SEM characterised smooth and homogeneous thin layer of ZnO resulting from 1:1 mix of ethanol and acetone precursor solution cast, which we think reflects the better solvent properties / absence of aggregates in the precursor, although SEM does not look at the solution so can not strictly tell us properties of the precursor solution. I find that the transistor from precursor cast from mixed solvent performs better than the one cast from pure EtOH and that the transistor sheet current and other performance characteristics are superior to previously reported precursor- route ZnO TFTs, when gated by the aqueous electrolyte PBS. Finally, The above PBS gated ZnO TFT is a near match to the performance of ZnO transistors deposited by conventional ‘dry’, precursor- free methods such as magnetron sputtering or laser ablation, and gated by dry dielectrics.

Chapter 7
A water- gated organic thin film transistor as sensor for waterborne amines.

7.1 Introduction

Proteins are found in many foods like meat, fish and dairy products and are considered a key ingredient. However, When proteins are broken down e.g. by bacteria, food is considered spoiled. As a result of protein breakdown, amines are released [99]. Therefore, amine sensors are considered as a tool to ascertain the degree of freshness of food.

Previous studies have shown that organic conductors have propensity to respond to airborne amine (amine 'odours'). A study of Sotzing *et al.* [100] showed that a chemiresistor built from a sulfonic acid- doped poly(aniline) (PAni) synthetic metal / carbon black composite was significantly sensitive and selective to amine odours. With odour exposure, the resistance increased significantly because of de-doping of the acid-doped PAni. The amine in this case acted as a Lewis base. Hague *et al.* [4] showed dielectric- gated organic transistor based sensor for amine odours where a previously un-doped n-type organic semiconductor was doped by amine odours, with resultant impact on the characteristics of the transistor [101-106].

Here I present a study that extends the scope of sensitivity of organic semiconductors to amines to the sensing of waterborne amines. The basic premise of the sensor again builds on the discovery of Berggren *et al.* [26] who showed that organic thin film transistors (OTFTs) can be gated using water as an electrolytic gate medium. Other works done by various researchers are also on record which indicate the detection of water-borne analytes by monitoring the characteristics of water- gated OTFTs, including quantitative response vs. analyte concentration characteristics [34, 35, 107, 108]. In the above mentioned studies, the sensors usually relied on the sensitizing of the OTFT with an analyte- specific receptor. Here, we utilize the natural sensitivity of thiophene- based organic semiconductors to amines to devise a water-gated OTFT that acts as amine- sensitive and selective sensor.

7.2 Device preparation, analyte delivery, and electrical characterization

7.2.1 Flow Cell Transistors

The preparation and deposition of Au/Cr source/drain substrates was explained in Chapter 2. In addition, the structure and geometric dimensions of the 'sandwich' flow cell TFTs, which is used here, was described in section (4.1.1). The source/drain contacts substrate coated with

p-type semiconducting polymer Poly(2,5-bis(3hexadecylthiophen-2-yl)thieno[3,2-b]thiophene) (PBTTT) sourced from Ossila Ltd. This was then spincast from 7 mg/mL hot solution (~100 °C) in 1,2-Dichlorobenzene (5000 rpm for 40 seconds). Finally, it was dried under dynamic vacuum at 110 °C for 45 min. PBTTT performs well in water- gated OTFTs[65].

7.2.2 Analyte delivery

As be explained before in section (4.1.2), two syringe pumps were used in parallel with different adjustable speeds and both syringes were filled with the following:

1. DI water.
2. A saturated solution of octylamine in DI water as an example amine, or with a saturated aqueous solution of the analogous alcohol 1-octanol for control experiments. Octylamine and 1-octanol sourced from Aldrich, aqueous solution saturates at 1.54 mM at 25 °C for octylamine, and 3.53 mM for 1-octanol [109].

The sum of the pump rates (both pumps) at 250 µL/minute is held constant for the study, section (4.4); ratio of the pump rates is changed so that the analyte concentration in the resulting mixture is the variable as be seen in Table 4-1 and Table 4-2. The total dead volume flow of the sensing system (flow cell and tubing) was turned over in ~14 seconds, as explained in section (4.2). Figure 4-4 shows a sketch of the analyte delivery system.

7.2.3 Electrical characterisation

For electrical characterisation, a setup of a bespoke current/voltage *I/V* converter as described previously in section (3.2.2) can likewise be utilized for recording saturated transfer characteristics parametric in time. This system was used with sinusoidal voltage drive of magnitude 1 V at 1 Hz frequency applied to OFET (PBTTT TFT) driven. Data were recorded every second of peak drain current for both "on" current $I_{on}(t)$ (at $V_S(t)$ = +1 V) and "off" current $I_{off}(t)$ (at $V_S(t)$ = -1 V).

7.3 PBTTT thin film transistor for sensing water-borne amine (Amine sensor)

Figure 7-1 shows the 'on- current' of transistor when continuously pumping with plain DI water over a period of approximately 2 hrs. Low noise data were recorded with the OTFT peak drain current initially drifting from a large negative value of 480 nA towards lower values nearing (290±5) nA that no longer drifts after 1 hr. This drift may be assigned to 'washing' of water soluble dopants out of PBTTT. The organic semiconductor contains a small amount of unintentional dopants. These dopants carry only a small current (the transistor's off- current),

however, the presence of dopants significantly improves carrier injection at the contacts by forming Schottky junctions [110]. Therefore, loss of dopants may lead to reduced injection.

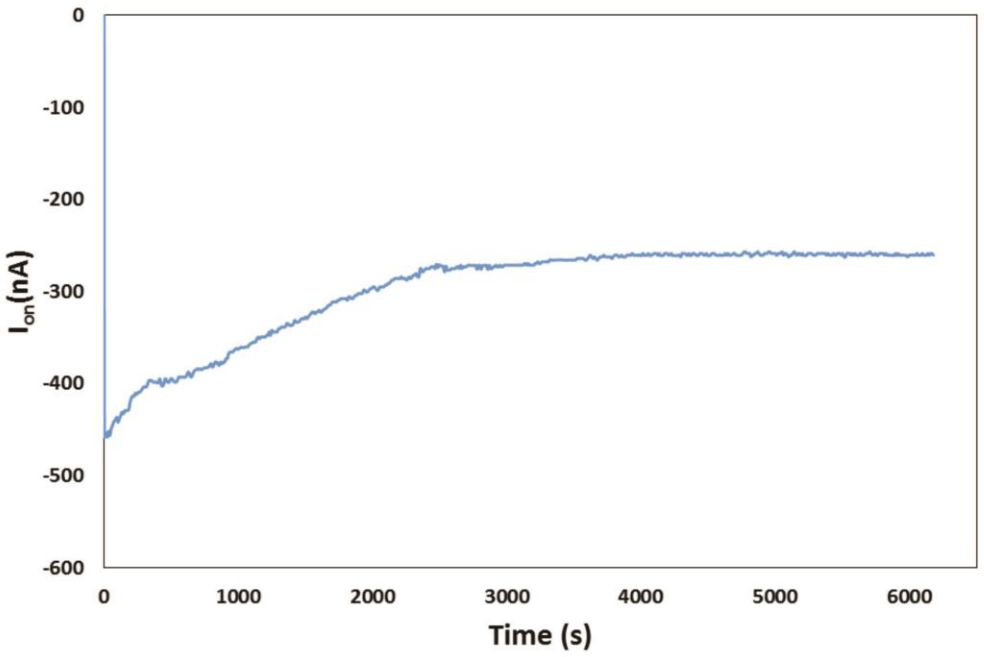

Figure 7-1: Drift of water- gated PBTTT OTFT 'on' current under continuous pumping with plain DI water over ~2 hrs.

Figure 7-2(a) shows a chart for a PBTTT OTFT previously conditioned by 45 minutes 'washing' under continuous purge of DI water. The octylamine analyte is cycled at different levels with transitional periods of recovery under purge of plain DI water. The shaded area indicates the time periods of exposure to the analyte along with their respective concentration levels, while the clear areas are the recovery periods. A reduced or less negative level is noted for OTFT 'on' current when the OTFT is subjected to the octylamine solutions. Under low concentration of octylamine exposure recovery under DI water purge is noted to be after ≈ 60 seconds. For higher concentration, the recovery time increases and is noted to be up to ≈ 210 seconds. In addition, after exposure to saturated octylamine, the PBTTT OTFT was exposed to lower octylamine concentrations again (final 3 exposure cycles in Figure 7-2(a), (275, 550, 825) μM). It is seen that the PBTTT OTFT still responds to lower octylamine concentrations, the quantitative analysis is included below in Figure 7-3. However, the recovery time raise and is recorded ≈ 300 seconds as be seen in Figure 7-2(a). The big challenge to test varied concentrations after saturation exposure is degradation of the PBTTT OTFT after 75 minutes under continuous flow of DI water with variable octylamine concentrations.

As a control experiment, a PBTTT OTFT was also exposed to 1-octanol solutions, Figure 7-2(b). Response is noted to be weak even though higher accessible maximum concentration (1-octanol saturation in water at 3.53 mM vs. 1.54 mM for 1-octylamine) was provided. Further, response does not systematically increase with increasing concentration. Rather the response is mainly fleeting, occurring briefly after switching pump rate ratios, cf, Table 4-2. The I_{on} settles back to approximately the prior value within a few seconds time despite switching pump rates, and shows indifference to whether the OTFT is under DI water purge, or under high 1-octanol concentration. Hence, PBTTT does not respond to water- borne alcohols the same way response is noted for amines.

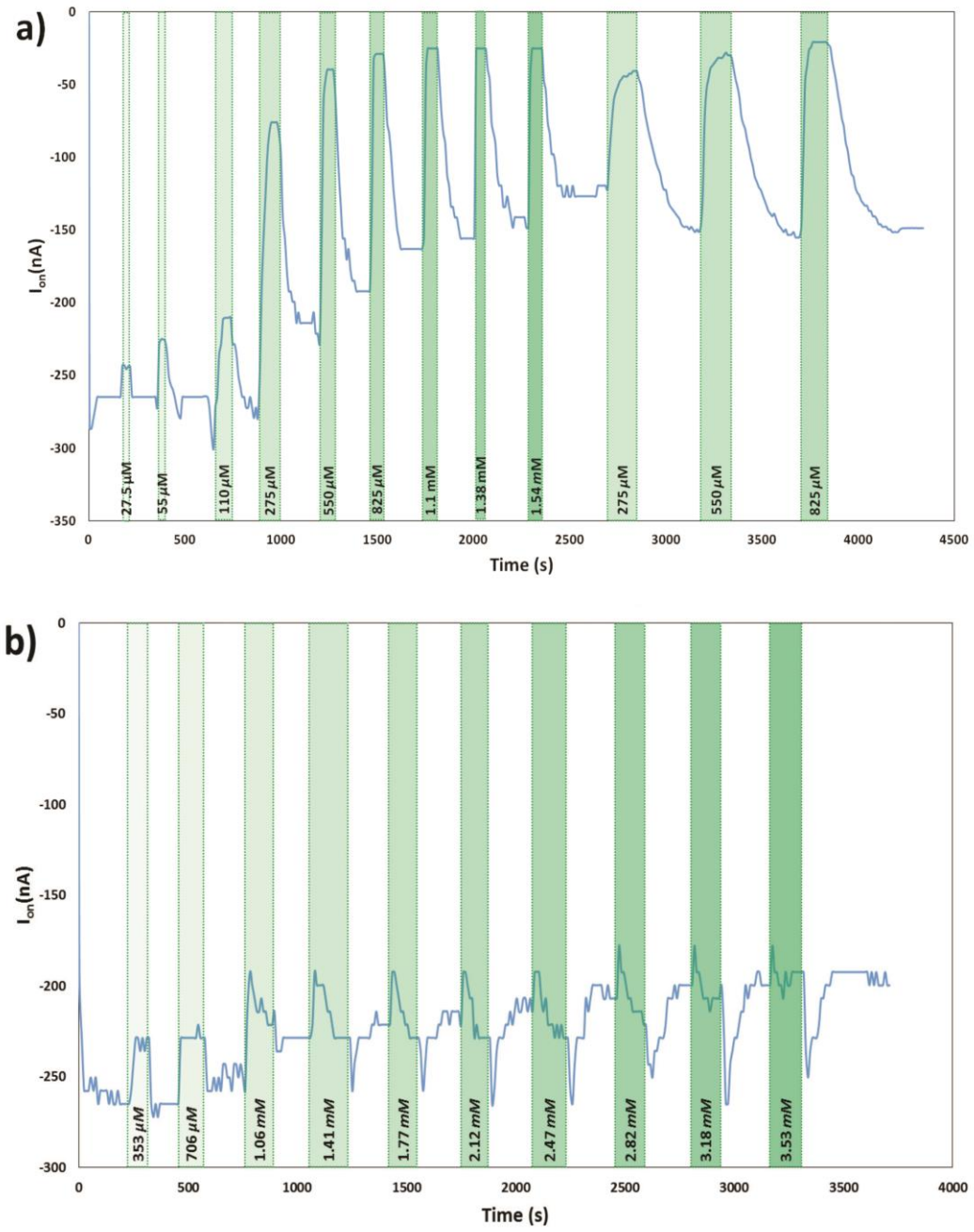

Figure 7-2: (a) Response of water- gated PBTTT OTFT 'on' current under exposure/recovery cycles to octylamine concentrations ranging from 27.5 to 1540 µM and return to earlier concentrations from 275 to 825 µM. (b): Control experiment with 1-octanol, concentration ranging from 353 µM to 3530 µM.

For quantitative analysis of the response of PBTTT OTFTs to water- borne amine, any effect of residual OTFT drift over time was excluded by normalising current response to analyte, $\Delta I_D(c)$, to $I_D(0,t)$, which stands for the drain current under purge immediately before analyte concentration c was applied. This results in the calibration chart for $\Delta I_D\ (c)\ /\ I_D\ (0,\ t)$, Figure 7-3(a). Figure 7-3(a) shows data taken from two separate experimental series. The data

sets are noted to fall on similar smooth curves. This indicates a reliable, repeatable calibration and is not dependent on variation among transistor substrates. One of the tested transistors was also exposed to lower concentrations [(275, 550, 825) μM] of water- borne amine again after saturation exposure, as shown in Figure 7-2. Response data are normalised in the same way and are shown as red squares in Figure 7-3. When presented in normalised form these points again fall onto the same calibration curve, indicating fully reversible sensor response.

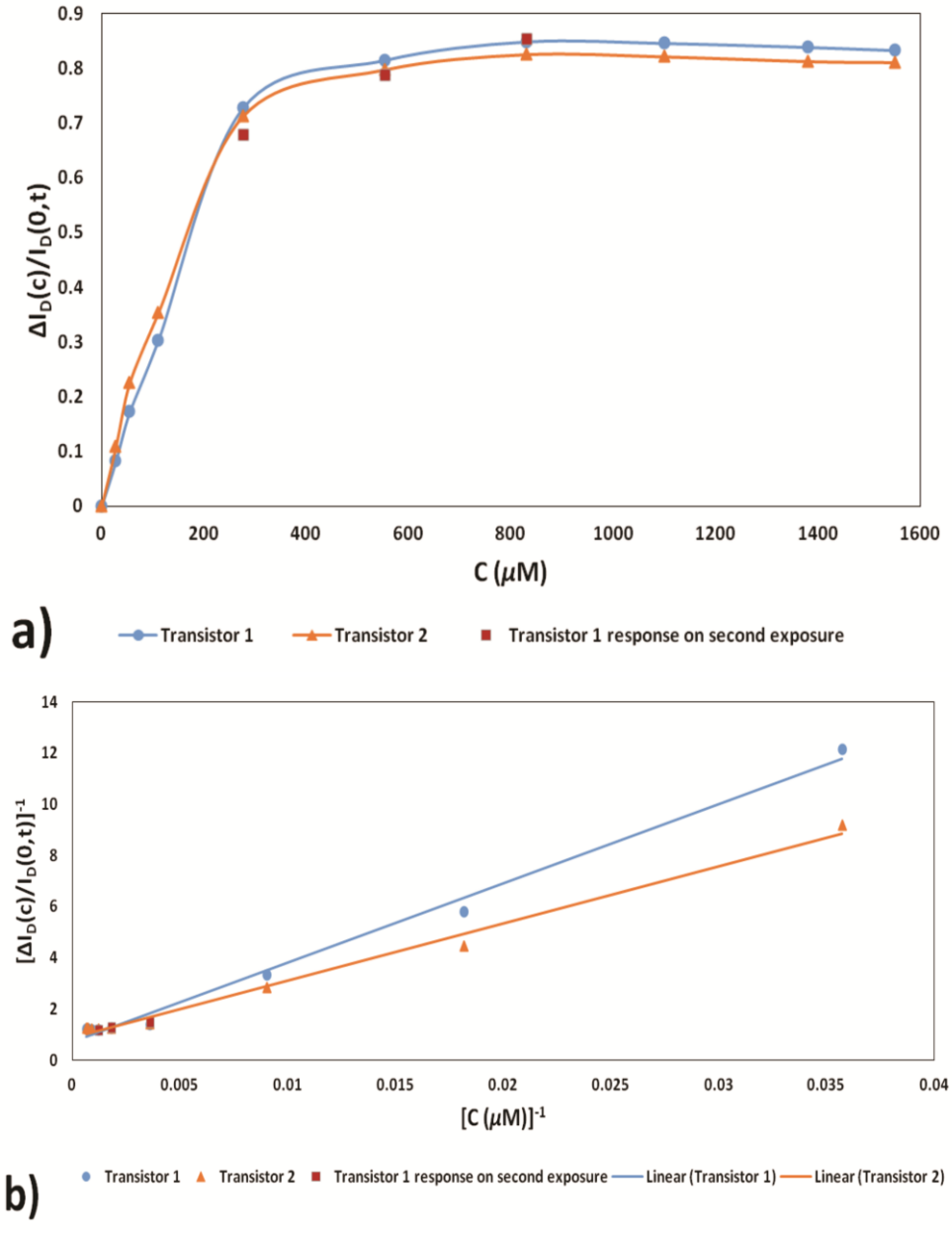

Figure 7-3: (a) Water- gated PBTTT OTFT on- current response to different octylamine concentrations in normalised form, $\Delta I_D(c) / I_D(0,t)$ 1st exposure (blue circle symbol)and 2nd exposure (red square symbol) Results are shown for transistor 1. (Orange triangle symbol) Result is shown for transistors 2. (b): Same data plotted in the form $[\Delta I_D(c) / I_D(0,t)]^{-1}$ vs. c^{-1}.

Figure 7-3(a) shows data taken from two separate experimental series (similar as in Figure 7-2) on different OTFTs, which are denoted in different symbols. The data sets are noted to fall on similar smooth curves. This indicates a dynamic, repeatable calibration and is not dependent on variation among transistor substrates. The drift of zero- analyte current with time is effectively compensated by both, prior conditioning, and normalising OTFT current response to amine to the zero- analyte current immediately before exposure. The curves initially show a significant rise at low concentrations, but tapers to a saturated response of ≈ 0.8 before octylamine concentration in water saturates at 1540 µM. This shape is similar to a Langmuir adsorption isotherm that describes fractional monolayer coverage $\Theta(c)$ for mutually independent adsorption positions on a smooth solid surface in contact with a fluid carrying an adsorbate at concentration *c*:

$$\Theta(c) = \frac{kc}{(1+kc)}, \qquad 7\text{-}1$$

wherein k is the equilibrium constant for the adsorption / desorption equilibrium,

Octylamine (dissolved) + vacant PBTTT surface site ← → Octylamine adsorbed to PBTTT site which is dependent on strength of adsorbate/surface interactions, and temperature. $1/k$ corresponds to the concentration $c_{1/2}$ that leads to $\Theta = 1/2$.

If octylamine analyte is taken as the adsorbate with the assumption that $[\Delta I_D(c) / I_D(0,t)]$ is proportional to $\Theta(c)$, then the plot $[\Delta I_D(c) / I_D(0,t)]^{-1}$ vs. c^{-1} would result in a straight line with positive slope and positive intercept, with the ratio of slope/intercept equal to $1/k$.

The above is provided in Figure 7-3(b), data at low concentrations (large c^{-1}) are nearly defined by a straight line; although small differences between the two transistors' original data are amplified. The data for high *c* (low c^{-1}) saturate, level off to a flat (zero slope) line. Therefore, if noted on overall basis the Langmuir isotherm provides a good platform for the observed $[\Delta I_D(c) / I_D\ (0,\ t)]$ vs. *c* data, which indicates adsorption of water-borne amine onto PBTTT surface, rather than bulk penetration, as the cause of the observed reduction in saturated drain current.

It is generally established that the Langmuir isotherm in its simple form, equation (7-1), mainly provides an approximate fit to experimental data while modifications are required for quantitative analysis [111]. When $1/k$ is still calculated from the fit parameters of the Langmuir plot Figure 7-3(b), 440 µM (transistor 1) / 250 µM (transistor 2) is noted, but relative error (in

particular for intercept) is large. A review of the original data (Figure 7-3) suggests $\Theta = ½$ (i.e. $\Delta I_D(c) / I_D(0, t) = 0.4$) is attained at approximately 150 µM octylamine concentration for both transistors, hence $1/k = c_{1/2} \sim 150$ µM.

7.4 Conclusions

We have shown that the sensitivity of organic semiconductors to amine vapours [4, 100-106] translates to water-borne amines. This can be seen with water- gated PBTTT OTFTs, which respond with a reduced drain current when octylamine is added to the gating water. The original OTFT drift is reduced by initial conditioning, and can be accounted for by normalising current response to the current level under purge immediately before exposure.

Normalised current response vs. amine concentration is replicable between different transistors, and reversible by purge in pure water.

The sensor response characteristic can be estimated by a Langmuir adsorption isotherm. This indicates water-borne octylamine physisorps from aqueous solution to adsorption locations at the PBTTT surface, rather than penetrating into PBTTT bulk. As a result, OTFT current is reduced in proportion to fractional surface coverage. The precise reason for mobility reduction is not exactly clear, this may be due to a disruption of charge carrier transport by adsorbed amine, note that the accumulation layer in a water- gated OTFT forms at the same surface where analyte may adsorb, allowing an immediate effect of adsorbate on charge transport. Alternatively, adsorbate may disrupt the electric double layer with consequentially reduced capacitance.

In a control experiment, little response of PBTTT OTFTs is observed to similar and higher concentrations of a different solute, 1-octanol, which superficially interacts distinctly less strongly with PBTTT than the matching amine.

The extracted value $1/k = c_{1/2} \sim 150$ mM allows an estimate of the strength of the amine / PBTTT 'bond', more precisely the standard Gibbs free energy of adsorption, ΔG^O. ΔG^O controls k in equation (7-1) via a Boltzmann factor, $k \sim \exp(-\Delta G^O / RT)$, wherein R is the gas constant, $R = 8.314$ J/mol K. However, the often- quoted equation to calculate ΔG^O from k,

$$\Delta G^o = -RT \ln k \qquad 7\text{-}2$$

is not correct, as it implies taking the logarithm of k. Note that the definition of k in equation (7-1) implies a unit of measurement for k, namely, L/mol. Transcendental functions like the

logarithm are defined for dimensionless numbers only, not for quantities that carry units. The misuse of equation (7-2) and the correct calculation of ΔG^O are discussed in detail by Zhou and Zhou [112]. They establish the correct equation for ΔG^O as

$$\Delta G^o = -RT \ln k^o \quad 7\text{-}3$$

wherein k^O is the dimensionless standard adsorption constant. k^O is calculated from k, which is defined in equation (7-1) as the adsorption constant of the solute (here octylamine), by multiplication with the concentration of solvent (here water) in units mol/L (M), which leads to cancellation of units:

$$k^o = k c_{solvent} = \frac{C_{solvent}}{c_{1/2}} \quad 7\text{-}4$$

k^O now correctly reflects the adsorption process as a competition for adsorption sites between the adsorbate (octylamine), and the solvent (water). At $c_{1/2} = k^{-1}$, the solute covers as many adsorption sites as the solvent (namely, half of available sites), although solvent molecules outnumber solute k^O times. This is because the binding of solute to the adsorption site is stronger than the binding of solvent, conforming with the definition of ΔG^O as the difference between Gibbs free energies of adsorption sites occupied by adsorbate (octylamine), and sites occupied by solvent (water). Equation (7-3) quantifies this difference from k^O.

For water, from the density ρ_{water} = 1kg/L, and molecular weight m_{water} = 18 g/mol, we calculate the concentration of (pure) water $c_{water} = \rho_{water}/m_{water}$ = 55.56 mol/L = 55.56 M. We can neglect the small difference between c_{water} and $c_{solvent} = c_{water} - c_{amine}$, as c_{amine} < 1.53 mM << c_{water}. Hence, here k^O = 55.56 M / 150 mM = 370,400 ≈ 3.7x10^5. Equation (7-3) gives ΔG^O = -31.2 kJ/mol, equivalent to 324 meV/molecule.

Chapter 8
Summary and Future Work

In the current thesis, I have presented my work in the field of electrolyte- gated thin film transistors (TFTs), which is a long- standing research interest in my supervisor's research group. Building on the work of prior group members, I can report a number of advances.

In Chapter 5, I could show an electrolyte- gated organic TFT with exceptionally high 'on' current (i.e., low sheet resistance in the 'on' state). This was by combining a high performance organic semiconducting polymer, PBTTT, with a particularly high capacitance electrolytic gate medium, namely, an ionic liquid.

In Chapter 6, I could show a route to improved performance of a water gated TFT using a precursor- route inorganic semiconductor, the II-VI material zinc oxide (ZnO). It is well established in the field of solution- processed organic semiconductors that the choice of processing solvent can have a strong influence on resulting film morphology, and hence their performance (including, fluorescence quantum yield for light emitters, and carrier mobility for TFT semiconductors). Often, the better the solvent, the better the performance (albeit other factors, in particular the solvent's volatility, are also important). Here, I could show that this principle extends to the preparation of precursor- route inorganic semiconductors: The precursor of ZnO, zinc acetate, dissolves more readily in a mix of ethanol and acetone, rather than in pure solvent alone. I can show that ZnO films processed from mixed solvent have a smoother surface morphology than those processed from pure ethanol, and that performance of ZnO in water- gated TFTs is better for films cast from mixed solvent.

Finally, in Chapter 7, I can show the application of water- gated TFTs using an organic semiconductor (PBTTT) as a sensor for a biologically relevant waterborne analyte, amine. I can present a calibration chart for the transistor's 'on' current response vs. amine concentration in the gating water, which can be modelled by the Langmuir adsorption isotherm that describes fractional surface coverage by an adsorbate. This enables quantitative analysis and the determination of an equilibrium constant for the strength of the interaction between amine, and semiconductor surface. A potential interferant (an alcohol) does not lead to a response, indicating weak or no adsorption.

The work in Chapter 7 was prepared by my development of a sample delivery / TFT flow cell unit, described in Chapter 4. This unit allows delivery of a constant stream of water with

variable analyte concentration to a water- gated TFT formed in a flow cell. The delivery/test unit integrates a real- time TFT characterisation system built by a previous group member, and will hopefully find use in future research in our group, carried by my successors.

As an outline of future research, building on work reported here, I see at least two promising lines: Firstly, further exploration of alternative precursor routes to ZnO, including different precursors, different solvents, and introducing dopants into precursor solutions- the latter not for TFTs, but transparent conductive layers. Secondly, the design of water- gated sensor TFTs that do not rely in an innate affinity between semiconductor and analyte (as in the adsorbance of amine to PBTTT surfaces), but where a ‘sensitiser' is deliberately added to the semiconductor casting solution. This is an elegant, simplified alternative to the introduction of sensitisers elsewhere in the TFT architecture. Work in both lines is currently already undertaken by my successors, and I will follow it with interest.

Published papers and attended conferences

1. Saud A. Algarni, Talal M. Althagafi, Patrick J. Smith, Martin Grell, "An ionic liquid-gated polymer thin film transistor with exceptionally low "on" resistance," ***Applied Physics Letters***, 2014. 104(18): p. 182107.
2. Saud A. Algarni, Talal M. Althagafi , Abdullah Al Naim, Martin Grell, "A water-gated organic thin film transistor as a sensor for water-borne amines," ***Talanta***, 2016. 153: p. 107-110.
3. Talal M. Althagafi, Saud A. Algarni, Abdullah Al Naim, Javed Mazher , Martin Grell, "Precursor-route ZnO films from a mixed casting solvent for high performance aqueous electrolyte-gated transistors," ***Physical Chemistry Chemical Physics***, 2015. 17(46): p. 31247-31252.
4. Talal M. Althagafi, Saud A. Algarni, Martin Grell, "Innate cation sensitivity in a semiconducting polymer," ***Talanta***, 2016. 158: p. 70-76.
5. Talal M. Althagafi, Abbad F. Al Baroot, Saud A. Algarni, Martin Grell, "A membrane- free cation selective water- gated transistor," ***Analyst,*** 2016.
6. Saud A. Algarni, Talal M. Althagafi, Patrick J. Smith, Martin Grell, "An ionic liquid-gated polymer thin film transistor with exceptionally low "on" resistance," (poster presentation), ***UK Semiconductors '14****, Sheffield, United Kingdom*, Jul, 2014.
7. Saud A. Algarni, Talal M. Althagafi, Abbad F. Al Baroot, Martin Grell, "Sensing waterborne analytes with water- gated thin film transistors," (poster presentation), ***UK Semiconductors '16****, Sheffield, United Kingdom*, Jul, 2016.

References

1. S. Ono, S. Seki, R. Hirahara, Y. Tominari and J. Takeya, Applied Physics Letters **92** (10), - (2008).
2. L. M. Dumitru, K. Manoli, M. Magliulo, L. Sabbatini, G. Palazzo and L. Torsi, ACS Applied Materials & Interfaces **5** (21), 10819-10823 (2013).
3. B. H. Hamadani, D. J. Gundlach, I. McCulloch and M. Heeney, Applied Physics Letters **91** (24), - (2007).
4. L. Hague, D. Puzzovio, A. Dragoneas and M. Grell, Science of Advanced Materials **3** (6), 907-911 (2011).
5. A. Dragoneas, L. Hague and M. Grell, J. Sens. Sens. Syst. **4** (1), 169-177 (2015).
6. Z. Bao and J. Locklin, *Organic Field-Effect Transistors*. (CRC Press, Boca Raton, 2007).
7. M. Ahles, R. Schmechel and H. von Seggern, Applied Physics Letters **85** (19), 4499-4501 (2004).
8. J. G. Simmons, Physical Review Letters **15** (25), 967-968 (1965).
9. O. D. Jurchescu, J. Baas and T. T. M. Palstra, Applied Physics Letters **84** (16), 3061-3063 (2004).
10. J. Becker, E. Fretwurst and R. Klanner, Solid-State Electronics **56** (1), 104-110 (2011).
11. H. Bässler, physica status solidi (b) **175** (1), 15-56 (1993).
12. W. F. Pasveer, J. Cottaar, C. Tanase, R. Coehoorn, P. A. Bobbert, P. W. M. Blom, D. M. de Leeuw and M. A. J. Michels, Physical Review Letters **94** (20), 206601 (2005).
13. C. Tanase, E. J. Meijer, P. W. M. Blom and D. M. de Leeuw, Physical Review Letters **91** (21), 216601 (2003).
14. H. T. Nicolai, M. Kuik, G. A. H. Wetzelaer, B. de Boer, C. Campbell, C. Risko, J. L. Brédas and P. W. M. Blom, Nat Mater **11** (10), 882-887 (2012).
15. L.-L. Chua, J. Zaumseil, J.-F. Chang, E. C. W. Ou, P. K. H. Ho, H. Sirringhaus and R. H. Friend, Nature **434** (7030), 194-199 (2005).
16. M. C. Petty, *Molecular Electronics*. (John Wiley & Sons Ltd, Chichester, 2007).
17. P. K. Weimer, Proceedings of the IRE **50** (6), 1462-1469 (1962).
18. A. Tsumura, H. Koezuka and T. Ando, Applied Physics Letters **49** (18), 1210-1212 (1986).
19. C. Clarisse, M. T. Riou, M. Gauneau and M. Le Contellec, Electronics Letters **24** (11), 674-675 (1988).
20. F.-C. Chen, Y.-S. Lin, T.-H. Chen and L.-J. Kung, Electrochemical and Solid-State Letters **10** (6), H186-H188 (2007).
21. A. Facchetti, M. H. Yoon and T. J. Marks, Advanced Materials **17** (14), 1705-1725 (2005).
22. Y.-Y. Noh and H. Sirringhaus, Organic Electronics **10** (1), 174-180 (2009).
23. M. E. Roberts, N. Queraltó, S. C. B. Mannsfeld, B. N. Reinecke, W. Knoll and Z. Bao, Chemistry of Materials **21** (11), 2292-2299 (2009).
24. L. A. Majewski, R. Schroeder and M. Grell, Advanced Materials **17** (2), 192-196 (2005).
25. K. Ueno, S. Nakamura, H. Shimotani, A. Ohtomo, N. Kimura, T. Nojima, H. Aoki, Y. Iwasa and M. Kawasaki, Nat Mater **7** (11), 855-858 (2008).
26. L. Kergoat, L. Herlogsson, D. Braga, B. Piro, M.-C. Pham, X. Crispin, M. Berggren and G. Horowitz, Advanced Materials **22** (23), 2565-2569 (2010).
27. H. Helmholtz, Annalen der Physik **165** (6), 211-233 (1853).
28. M. Gouy, J. Phys. Theor. Appl. **9** (1), 457-468 (1910).

29. O. Stern, Journal of Applied Electrochemistry and Physical Chemistry **30** (21-22), 508-516 (1924).
30. H. Wang and L. Pilon, Electrochimica Acta **63**, 55-63 (2012).
31. Y. He S. H. Yalkowski and P. Jain, *Handbook of Aqueous Solubility Data* 2nd edition ed. (Boca Raton, 2010).
32. K. Izutsu, *Electrochemistry in nonaqueous solutions*. (John Wiley & Sons, Weinheim, 2009).
33. L. Kergoat, B. Piro, M. Berggren, M.-C. Pham, A. Yassar and G. Horowitz, Organic Electronics **13** (1), 1-6 (2012).
34. F. Buth, A. Donner, M. Sachsenhauser, M. Stutzmann and J. A. Garrido, Advanced Materials **24** (33), 4511-4517 (2012).
35. S. Casalini, F. Leonardi, T. Cramer and F. Biscarini, Organic Electronics **14** (1), 156-163 (2013).
36. R. Hagiwara, K. Matsumoto, Y. Nakamori, T. Tsuda, Y. Ito, H. Matsumoto and K. Momota, Journal of The Electrochemical Society **150** (12), D195-D199 (2003).
37. S. W. Lee, H. J. Lee, J. H. Choi, W. G. Koh, J. M. Myoung, J. H. Hur, J. J. Park, J. H. Cho and U. Jeong, Nano Letters **10** (1), 347-351 (2010).
38. A. F. Al Naim and M. Grell, Journal of Applied Physics **112** (11), - (2012).
39. T. Uemura, M. Yamagishi, S. Ono and J. Takeya, Applied Physics Letters **95** (10), - (2009).
40. E. Said, X. Crispin, L. Herlogsson, S. Elhag, N. D. Robinson and M. Berggren, Applied Physics Letters **89** (14), 143507 (2006).
41. T. Someya, A. Dodabalapur, A. Gelperin, H. E. Katz and Z. Bao, Langmuir **18** (13), 5299-5302 (2002).
42. O. Inganas, Chemical Society Reviews **39** (7), 2633-2642 (2010).
43. M. J. Panzer and C. D. Frisbie, Advanced Functional Materials **16** (8), 1051-1056 (2006).
44. I. McCulloch, M. Heeney, C. Bailey, K. Genevicius, I. MacDonald, M. Shkunov, D. Sparrowe, S. Tierney, R. Wagner, W. Zhang, M. L. Chabinyc, R. J. Kline, M. D. McGehee and M. F. Toney, Nat Mater **5** (4), 328-333 (2006).
45. A. C. Mofor, A. El-Shaer, A. Bakin, A. Waag, H. Ahlers, U. Siegner, S. Sievers, M. Albrecht, W. Schoch, N. Izyumskaya, V. Avrutin, S. Sorokin, S. Ivanov and J. Stoimenos, Applied Physics Letters **87** (6), 062501 (2005).
46. H. T. Wang, B. S. Kang, F. Ren, L. C. Tien, P. W. Sadik, D. P. Norton, S. J. Pearton and J. Lin, Applied Physics Letters **86** (24), 243503 (2005).
47. L. C. Tien, P. W. Sadik, D. P. Norton, L. F. Voss, S. J. Pearton, H. T. Wang, B. S. Kang, F. Ren, J. Jun and J. Lin, Applied Physics Letters **87** (22), 222106 (2005).
48. Y. Qin, X. Wang and Z. L. Wang, Nature **451** (7180), 809-813 (2008).
49. Z. H. Wang, D. Y. Geng, Z. Han and Z. D. Zhang, Materials Letters **63** (29), 2533-2535 (2009).
50. P. Sagar, M. Kumar and R. M. Mehra, Thin Solid Films **489** (1–2), 94-98 (2005).
51. K. Nomura, H. Ohta, K. Ueda, T. Kamiya, M. Hirano and H. Hosono, Science **300** (5623), 1269-1272 (2003).
52. P. F. Carcia, R. S. McLean and M. H. Reilly, Applied Physics Letters **88** (12), 123509 (2006).
53. S. Y. Park, B. J. Kim, K. Kim, M. S. Kang, K.-H. Lim, T. I. Lee, J. M. Myoung, H. K. Baik, J. H. Cho and Y. S. Kim, Advanced Materials **24** (6), 834-838 (2012).
54. B. S. Ong, C. Li, Y. Li, Y. Wu and R. Loutfy, Journal of the American Chemical Society **129** (10), 2750-2751 (2007).
55. A. Al Naim and M. Grell, Applied Physics Letters **101** (14), - (2012).
56. H. Klauk, Chemical Society Reviews **39** (7), 2643-2666 (2010).

57. M. Park, B. D. Chin, J.-W. Yu, M.-S. Chun and S.-H. Han, Journal of Industrial and Engineering Chemistry **14** (3), 382-386 (2008).
58. Ossila, (http://www.ossila.com/, Sheffield, 2014).
59. L. Kergoat, L. Herlogsson, B. Piro, M. C. Pham, G. Horowitz, X. Crispin and M. Berggren, Proceedings of the National Academy of Sciences **109** (22), 8394-8399 (2012).
60. J.C. Vickerman and I. Gilmore, *Surface Analysis: The Principal Techniques*. (Chichester, 2009).
61. A. Ortiz-Conde, F. J. García Sánchez, J. J. Liou, A. Cerdeira, M. Estrada and Y. Yue, Microelectronics Reliability **42** (4–5), 583-596 (2002).
62. C. Ucurum, H. Siemund and H. Göbel, Organic Electronics **11** (9), 1523-1528 (2010).
63. S. Y. Park, M. Park and H. H. Lee, Applied Physics Letters **85** (12), 2283-2285 (2004).
64. IEEE Std 1620-2004, 0_1 (2004).
65. S. A. Algarni, T. M. Althagafi, P. J. Smith and M. Grell, Applied Physics Letters **104** (18), 182107 (2014).
66. T. M. Althagafi, S. A. Algarni, A. Al Naim, J. Mazher and M. Grell, Physical Chemistry Chemical Physics **17** (46), 31247-31252 (2015).
67. T. M. Althagafi, S. A. Algarni and M. Grell, Talanta **158**, 70-76 (2016).
68. I. New Era Pump Systems, (2016).
69. P. F. v. Hutten, *Semiconducting Polymers*. (Wiley- VCH, Weinheim 2000).
70. J. Veres, S. D. Ogier, S. W. Leeming, D. C. Cupertino and S. Mohialdin Khaffaf, Advanced Functional Materials **13** (3), 199-204 (2003).
71. A. Al Naim, A. Hobson, R. T. Grant, A. Dragoneas, M. Hampton, C. Dunscombe, T. Richardson, J. E. Macdonald and M. Grell, Organic Electronics **14** (4), 1057-1063 (2013).
72. W. Xie and C. D. Frisbie, The Journal of Physical Chemistry C **115** (29), 14360-14368 (2011).
73. R. Hagiwara and Y. Ito, Journal of Fluorine Chemistry **105** (2), 221-227 (2000).
74. U. Löffelmann, N. Wang, D. Mager, P. J. Smith and J. G. Korvink, Journal of Polymer Science Part B: Polymer Physics **50** (1), 38-46 (2012).
75. H. Meier, U. Löffelmann, D. Mager, P. J. Smith and J. G. Korvink, physica status solidi (a) **206** (7), 1626-1630 (2009).
76. D.-Y. Shin and P. J. Smith, Journal of Applied Physics **103** (11), - (2008).
77. L. A. Majewski, R. Schroeder and M. Grell, Journal of Physics D: Applied Physics **37** (1), 21 (2004).
78. L. Hague, D. Puzzovio, T. H. Richardson and M. Grell, Sensor Letters **9** (5), 1692-1696 (2011).
79. E. C. Smits, S. G. Mathijssen, P. A. Van Hal, S. Setayesh, T. C. Geuns, K. A. Mutsaers, E. Cantatore, H. J. Wondergem, O. Werzer and R. Resel, Nature **455** (7215), 956-959 (2008).
80. H. Minemawari, T. Yamada, H. Matsui, J. y. Tsutsumi, S. Haas, R. Chiba, R. Kumai and T. Hasegawa, Nature **475** (7356), 364-367 (2011).
81. U. Zschieschang, F. Ante, T. Yamamoto, K. Takimiya, H. Kuwabara, M. Ikeda, T. Sekitani, T. Someya, K. Kern and H. Klauk, Advanced Materials **22** (9), 982-985 (2010).
82. E. Said, X. Crispin, L. Herlogsson, S. Elhag, N. D. Robinson and M. Berggren, Applied Physics Letters **89** (14), - (2006).
83. S. H. Kim, K. Hong, W. Xie, K. H. Lee, S. Zhang, T. P. Lodge and C. D. Frisbie, Advanced Materials **25** (13), 1822-1846 (2013).

84. M. Singh, G. Palazzo, G. Romanazzi, G. P. Suranna, N. Ditaranto, C. Di Franco, M. V. Santacroce, M. Y. Mulla, M. Magliulo, K. Manoli and L. Torsi, Faraday Discussions **174** (0), 383-398 (2014).
85. S. Thiemann, S. Sachnov, S. Porscha, P. Wasserscheid and J. Zaumseil, The Journal of Physical Chemistry C **116** (25), 13536-13544 (2012).
86. E. Fortunato, A. Pimentel, L. Pereira, A. Gonçalves, G. Lavareda, H. Águas, I. Ferreira, C. N. Carvalho and R. Martins, Journal of Non-Crystalline Solids **338–340**, 806-809 (2004).
87. L. Zhang, J. Li, X. W. Zhang, X. Y. Jiang and Z. L. Zhang, Applied Physics Letters **95** (7), 072112 (2009).
88. C. Brox-Nilsen, J. Jin, Y. Luo, P. Bao and A. M. Song, IEEE Transactions on Electron Devices **60** (10), 3424-3429 (2013).
89. B. Bayraktaroglu, K. Leedy and R. Neidhard, IEEE Electron Device Letters **29** (9), 1024-1026 (2008).
90. C. D. Wagner, L. H. Gale and R. H. Raymond, Analytical Chemistry **51** (4), 466-482 (1979).
91. D. Briggs, Surface and Interface Analysis **3** (4), v-v (1981).
92. R. Al-Gaashani, S. Radiman, A. R. Daud, N. Tabet and Y. Al-Douri, Ceramics International **39** (3), 2283-2292 (2013).
93. J. H. Zheng, Q. Jiang and J. S. Lian, Applied Surface Science **257** (11), 5083-5087 (2011).
94. J. Das, S. K. Pradhan, D. R. Sahu, D. K. Mishra, S. N. Sarangi, B. B. Nayak, S. Verma and B. K. Roul, Physica B: Condensed Matter **405** (10), 2492-2497 (2010).
95. L. G. Mar, P. Y. Timbrell and R. N. Lamb, Thin Solid Films **223** (2), 341-347 (1993).
96. S. Oertel, M. P. M. Jank, E. Teuber, A. J. Bauer and L. Frey, Thin Solid Films **553**, 114-117 (2014).
97. A. Al Naim and M. Grell, Applied Physics Letters **101** (14), 141603 (2012).
98. C. S. Kim, S. Lee, E. D. Gomez, J. E. Anthony and Y.-L. Loo, Applied Physics Letters **93** (10), 103302 (2008).
99. M. H. S. Santos, International Journal of Food Microbiology **29** (2–3), 213-231 (1996).
100. G. A. Sotzing, J. N. Phend, R. H. Grubbs and N. S. Lewis, Chemistry of Materials **12** (3), 593-595 (2000).
101. Y. Che, X. Yang, S. Loser and L. Zang, Nano Letters **8** (8), 2219-2223 (2008).
102. H. E. Katz, W. Huang, J. Sinha, H. Kong, K. Besar and T. J. Dawidczyk, 2013 (unpublished).
103. F. Liao, S. Yin, M. F. Toney and V. Subramanian, Sensors and Actuators B: Chemical **150** (1), 254-263 (2010).
104. N. J. Tremblay, B. J. Jung, P. Breysse and H. E. Katz, Advanced Functional Materials **21** (22), 4314-4319 (2011).
105. S. F. Liu, A. R. Petty, G. T. Sazama and T. M. Swager, Angewandte Chemie International Edition **54** (22), 6554-6557 (2015).
106. Y. Che, X. Yang, Z. Zhang, J. Zuo, J. S. Moore and L. Zang, Chemical Communications **46** (23), 4127-4129 (2010).
107. K. Schmoltner, J. Kofler, A. Klug and E. J. W. List-Kratochvil, Advanced Materials **25** (47), 6895-6899 (2013).
108. S. Park, S. Lee, C.-H. Kim, I. Lee, W.-J. Lee, S. Kim, B.-G. Lee, J.-H. Jang and M.-H. Yoon, Scientific Reports **5**, 13088 (2015).
109. Samuel H. Yalkowsky, Yan He and P. Jain, *Handbook of Aqueous Solubility Data*, Second Edition ed. (CRC Press, Taylor & Francis Group, Boca Raton, 2010).

110. R. Schroeder, L. A. Majewski and M. Grell, Applied Physics Letters **84** (6), 1004-1006 (2004).
111. Leszek Czepirski, Mieczyslaw R Balys and E. Komorowska-Czepirska, Internet Journal of Chemistry **3** (14) (2000).
112. X. Zhou and X. Zhou, Chemical Engineering Communications **201** (11), 1459-1467 (2014).